School of Industrial and Information Engineering
Master of Science in Engineering Physics

POLITECNICO
MILANO 1863

3D INTEGRATED PHOTONIC CIRCUIT FOR ASTROPHOTONIC APPLICATIONS

Supervisor: Dr. Roberto Osellame
Co-supervisor: Dr. Simone Piacentini

Candidate: **Andrea Adami**
Student ID: 896794

Academic Year: 2018/2019

Ringraziamenti

Desidero ringraziare il mio relatore, Dr. Roberto Osellame, per avermi accolto nel suo gruppo di ricerca e per avermi dato fiducia sin dall'inizio. Un grande ringraziamento va a Simone che mi ha enormemente aiutato e seguito in ogni passo in questi mesi e per la cura e pazienza con cui ha revisionato questo lavoro. Ringrazio Giacomo ed Andrea, i quali sono sempre stati disponibili a chiarire dubbi o curiosità, e l'intero gruppo degli *Osellami*: è stato un piacere trascorrere questo periodo con voi, in particolar modo le svariate attività extra-FLM.

Ringrazio Alessio, Chiara, Federico, Gabriele, Giacomo, Ming e Simone con i quali ho trascorso cinque fantastici anni (ed interminabili lezioni).

Ringrazio tutti gli amici che ci sono sempre stati.

Un grazie speciale va a mia madre e mio padre, che mi hanno sostenuto dall'inizio alla fine di questo lungo percorso.

Infine, grazie a Claudia, senza cui tutto questo non sarebbe stato possibile.

Contents

List of Figures

List of Tables

Abstract

The implementation of integrated photonic technologies can be beneficial in many fields of physics, ranging from telecommunications to quantum optics. In this respect, a novel application of photonics is related to the field of astronomy, where the small dimension and the high thermo-mechanical stability of the integrated circuits allow to improve the performances of the sky observation.

In this work, we present the implementation of a discrete beam combiner, an integrated interferometer capable of combining light of up to eight points of a telescope aperture, in order to increase the angular resolution. To fabricate the circuit, we exploited the Femtosecond Laser Micromachining technique in a glass substrate. Since celestial light is unpolarized, one of the main requirements of stellar interferometry is the polarization insensitivity of the beam combiner. For this reason, after the inscription process, we performed a thermal annealing step, which allowed us to reduce the waveguide birefringence by releasing the internal stresses of glass.

The integrated interferometer was tested with classical light in order to validate its functioning. In particular, the device showed insertion losses below 2.5 dB for all the eight different inputs, which can be considered a state-of-the-art result for an 6 cm long chip. Moreover, the device showed a polarization insensitive behavior and, from its interferometrical analysis, a minimum condition number of 8 was measured in the astronomical H band.

The last part of this work is devoted to a preliminary study for increasing the operation bandwidth of the device. Due to the complex geometry of the beam combiner, we decided to focus on achieving a broadband directional coupler, obtained by detuning two coupled waveguides. With this technique, we were able to fabricate a directional coupler with a reflectivity of $50 \pm 5\%$ in more than 100 nm.

Sommario

La fotonica integrata ha permesso enormi progressi in molti campi della fisica, dalle telecomunicazioni all'ottica quantistica. Una recente applicazione è da trovare in astronomia dove le piccole dimensioni e l'elevata stabilità termica e meccanica dei circuiti integrati hanno permesso di migliorare notevolmente le osservazioni astronomiche.

In questo lavoro presentiamo l'implementazione di un dispositivo chiamato *discrete beam combiner*. Esso è un interferometro integrato capace di combinare la luce proveniente da otto punti dell'apertura di un telescopio, in modo da aumentarne la risoluzione angolare. Per fabbricare il dispositivo, abbiamo usato la tecnica di microfabbricazione con laser a femtosecondi in un substrato di vetro. Siccome la luce proveniente da un corpo celeste è non polarizzata, è richiesto che il dispositivo abbia un comportamento indipendente dalla polarizzazione della luce in ingresso. Dopo la scrittura del circuito è stato dunque necessario operare un processo di annealing che ha permesso di ridurre la birifrangenza delle guide d'onda.

Il dispositivo è stato analizzato con luce classica, per validarne le funzionalità. Per tutti gli otto ingressi, le perdite di inserzione sono state ridotte sotto la soglia di 2.5 dB, un valore mai raggiunto prima per un chip con 6 cm di lunghezza. Inoltre, il dispositivo si comporta in maniera indipendente dalla polarizzazione, come richiesto. Un numero di condizionamento pari a 8 è stato misurato nella banda astronomica H.

Infine, è presentato uno studio preliminare sull'aumento della banda operativa del dispositivo. A causa della complessa geometria di quest'ultimo, abbiamo deciso di considerare un accoppiatore direzionale e studiarne in tal caso l'aumento di banda. Ciò può essere realizzato con un accoppiatore detunato, ottenuto variando la costante di propagazione delle due guide d'onda. Siamo stati così in grado di fabbricare un accoppiatore con una riflessione di $50 \pm 5\%$ su più di 100 nm.

Chapter 1

Introduction

Humans have always sought to comprehend all the objects present in the night sky. For this purpose astronomy was invented: a discipline aimed to the study of celestial features. The beginning of modern day astronomy can be found in the XVII century when Galileo observed the night sky with a telescope. It was then possible to observe a plethora of new phenomena and to answer old questions, as the famous heliocentric vs. geocentric debate.

Another huge revolution came three centuries later with Michelson and the invention of the interferometer. This idea paved the way for stellar interferometry: by combining observations from multiple telescopes, it is possible to greatly increase the resolution achieved. However, many constraints are still present limiting the observation accuracy. For example, the huge dimension of existing instruments can pose serious problems in term of noise and stability.

In the last years, the astronomical performances were further improved with the advent of astrophotonics. Instead of relying on bulk optics, the idea is to take advantage of integrated technologies, already available for telecommunication. Photonic technologies can be used to improve the resolution of celestial observations. Astrophotonics will allow in the future to push the accuracy to limits unthinkable with common telescope setups.

The scope of this work is to produce an integrated photonic device that will be used at the William Herschel Telescope in the Roque de los Muchachos Observatory (Spain). In particular, the device is able to combine up to eight light beams coming from a single telescope mirror, in order to correct for the observation perturbation introduced by the Earth atmosphere. The project is in collaboration with the Leibniz Institute for Astrophysics Potsdam.

The specifications for the device, together with the entire procedure that allowed its fabrication, will be here presented in detail throughout the work. In order to do this, many theoretical aspects have to be addressed, like the

basic principles of stellar interferometry or the fabrication technique used. Finally, the device is analyzed, in order to test if the performances follow the expectations.

The work begins in Ch. 2 with a general description of astrophotonics. Some theoretical aspects necessary to understand the device behavior are discussed with more detail. In Ch. 3 the writing technique used for the device fabrication is presented. The setup and methods adopted to study and characterize a device are shown in Ch. 4. With these notions, it is possible to discuss and eventually adapt the device specifications; this is presented in Ch. 5. The device is then optimized, fabricated and characterized. A complete description of this phases can be found in Ch. 6. The work is concluded with further improvement of the device, concerning the wavelength response (Ch. 7).

The entire fabrication process has been carried out at the IFN-CNR laboratories, inside the Physics Department of Politecnico di Milano. The majority of the characterization took place in the same place. Minor analyses have been carried out at the Leibniz Institute for Astrophysics Potsdam.

Chapter 2

Astrophotonics

Photonics is a discipline aimed to generate, manipulate and detect light. Optical fibers or waveguide circuits are used to modify the beam properties and to induce various phenomena. Many are the applications, ranging from telecommunication to medicine, from computing to metrology.

This chapter is focused on *astrophotonics*, an emerging field lying at the interface between astronomy and photonics. Photonics technologies are used to improve the resolution and the accuracy of astronomic observations. The first idea appeared in 1999, when it was proposed to use integrated photonics technologies – previously adapted for telecommunication – in order to improve the stability of stellar interferometers [1].

In the first section, a general review of astronomy sub-fields greatly improved by photonic technologies will be presented. Particular attention will be given to one of such fields, namely integrated optics beam combination schemes suitable for stellar interferometry observations. Stellar interferometry basic principles are also discussed. The chapter is concluded with a theoretical description of the integrated beam combination scheme.

2.1 Astrophotonics Branches

Five astronomy branches are here reviewed. Particular attention will be given to the improvements introduced by integrated photonics.

Each paragraph compares the features of bulk optics and integrated photonics instrumentation. The main theme is that integrated technologies allow higher stability, compactness and simplicity with respect to bulk ones.

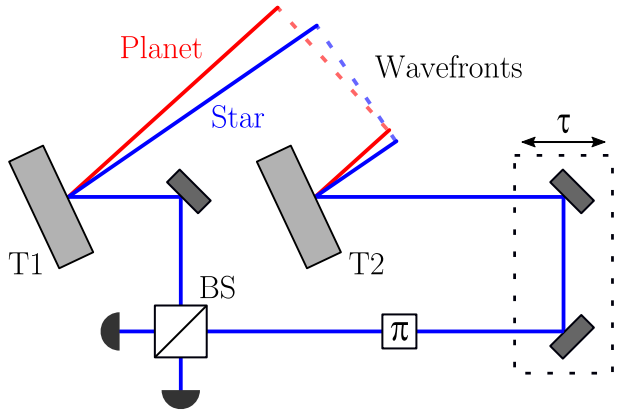

Figure 2.1: Nulling interferometry setup. The starlight (blue curve) is collected by two telescope; one of the beam goes through a delay line and a π phase shift. The two beams are combined at a beam splitter and they interfere. The same happens for the planet light (red curve) but with a different initial optical path difference. T1, T2 = Telescopes; BS = beam splitter.

2.1.1 Nulling Interferometry

In the search for exoplanets, a fundamental requirement is being able to distinguish them from the nearby star. This is difficult since they usually are orders of magnitude fainter than the parent star. Extreme high-contrast is required in order to separate the two bodies. A simple approach is to physically block the starlight with a mask placed in the focal plane, a technique called coronography. However, diffraction limits the light extinction.

A more powerful approach is nulling interferometry [2]. Light is collected by two telescopes, one of which introduces a π phase shift. A delay line is also required in order to correct for the different mirror-star distance in the two telescopes. The delay is adjusted so that the two beams interfere destructively.

A planet orbiting around the star has a different angular position from the latter, as seen from the Earth. At the observatory, the two collected beams have a different optical path difference with respect to the starlight. It is possible to tailor the delay line in order to place the planet light on a maximum of interference. In this way, while the starlight interferes destructively, the planet light does not, greatly increasing the contrast [3]. A scheme of the setup is shown in Fig. 2.1.

However, a very precise and stable setup is required: even small defects may result in imperfect starlight cancellation. The achievable contrast is thus limited [4]. Moreover, the atmosphere may introduce high spatial frequen-

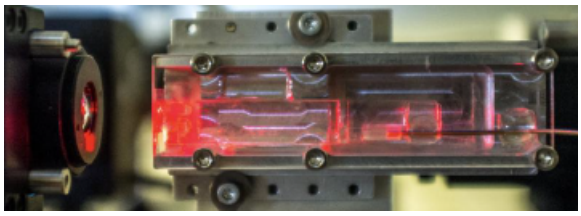

Figure 2.2: Back-illuminated GLINT device. Waveguides have been fabricated into a glass substrate. Taken from [5].

cies: the wavefront gets distorted, thus further decreasing the interferometric contrast.

An innovative method to correct these issues is to employ the intrinsic spatial filtering behavior of a single-mode waveguide. Such structure is able to propagate only the fundamental mode, independently of its input light. Higher-order modes are cut away and lost. The output wavefront is therefore planar, with a gaussian amplitude. The shape of the incoming wavefront only affects the amount of energy coupled into the waveguide [4].

A single-mode waveguide is then able to correct the wavefront by removing higher-order spatial structures. The result is a cleaner interference pattern with a higher nulling contrast.

The GLINT instrument, employed at the Anglo-Australian Telescope in Australia is a real application of this concept [5]. The device is shown in Fig. 2.2. Single-mode waveguides are used to remap and couple light and they are fabricated with the femtosecond laser micromachining, a technique that will be explained in Ch. 3. The advantage of using integrated photonic technologies is in the elevate robustness and stability of the whole device.

2.1.2 Light Filtering

When a telescope on the Earth's surface observes celestial light within the near-infrared band ($1 \div 1.8$ μm), observation is disturbed by bright narrow spectral lines due to the hydroxyl emission. Being able to filter out such features – while keeping high throughput between them – would greatly increase the observation quality [6].

This can be achieved with customized filters, like fiber Bragg gratings. The core refractive index is modulated with a periodic variation. Acting as a dielectric mirror, the fiber reflects only specific wavelengths while transmitting all the others. Having high reflectivity over a narrow bandwidth, fiber Bragg gratings are the optimal choice to suppress the unwanted hydroxyl emission.

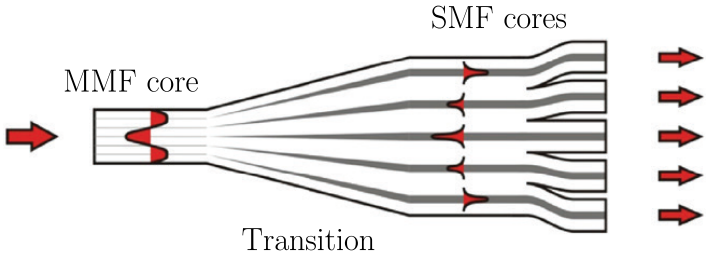

Figure 2.3: Photonic lantern device. The input is a MMF. After an adiabatic transition region, five SMFs are shown. Adapted from [7].

However, this phenomenon is reliable only for single-mode fiber (SMF) gratings. Since they support only the fundamental mode, they filter out higher-order spatial information. Instead, it would be preferable to couple light into a multi-mode fiber (MMF) [7], so that no incoming information is filtered out. The problem is that MMF have very poor performances: the Bragg grating response strongly depends on the excited mode [8].

The photonic lantern is a device able to merge the merits of the two, i.e. to improve the MMF performance up to SMF-like level. The MMF is used to collect almost all the light that has been smeared by the atmosphere. Light is then coupled into an array of independent SMFs, required for the high-quality Bragg grating. Several SMFs are needed since the MMF accepts more than one mode.

Consider an array of isolated and identical SMFs. Light propagation can be described in terms of supermodes of the array, i.e. as a group of independent SMF modes. The supermodes are degenerate and they are as many as the SMFs number [9]. The array is gradually tapered down to form a MMF. Provided the transition is adiabatic (i.e. slow enough), array supermodes can evolve into MMF modes, and vice versa. If the number of MMF modes matches the number of SMFs, light can be efficiently coupled between the two structures [10]. A schematic representation of the concept is shown in Fig. 2.3.

A fiber-based photonic lantern has been tested at the Anglo-Australian Telescope. It has been able to suppress all the hydroxyl emission lines within the range $1470 \div 1700$ nm [11].

The SMF bundle can be replaced by an array of single-mode waveguides within an integrated-photonic chip. Thus, the size, cost and complexity of existing devices can be greatly reduced. This is the primary choice when a high number of waveguides are required.

However, an integrated photonic lantern inherently requires a $3D$ waveguide fabrication technology, since the waveguide core has to be modified along

(a) Multi-mode waveguide. **(b)** 4x4 single-mode waveguides.

Figure 2.4: Microscope images of the input and output facets of an integrated photonic lantern fabricated with the femtosecond laser micromachining technique. Taken from [12].

the three directions [12]. The femtosecond laser micromachining technique is a good candidate for this purpose. Microscope images of the input and out facets of an integrated photonic lantern fabricated with this technique are shown in Fig. 2.4.

2.1.3 Spectroscopy

An unperturbed observation with a telescope has a physical limit to the angular resolution achieved. The observation is said to be diffraction-limited and the minimum angular resolution depends on the telescope mirror diameter. Features with angular separation smaller than

$$\alpha = 1.22 \, \frac{\lambda}{D} \tag{2.1}$$

where D is the telescope mirror diameter and λ the light wavelength, cannot be distinguished.

However, for a ground-based telescope, the observation is perturbed by the atmosphere turbulent motion and the angular resolution is further decreased (more details about this issue in § 2.2.1). In this case the observation is called seeing-limited, rather than diffraction-limited as before.

During most observations, the spectrograph is one of the principal instruments employed. It allows to disperse light, thus being able to perform a spectrum analysis of the source. A spectrograph operating at the seeing-limited regime has a size proportional to the mirror diameter. Indeed, as the telescope size increases in order to collect more light, the spectrograph size must increase as well. Modern-day astronomy spectrographs can be up to 6 m long

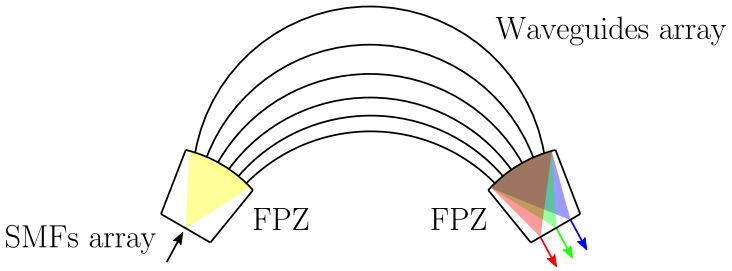

(a) FPZ = Free-propagation zone. Adapted from [13].

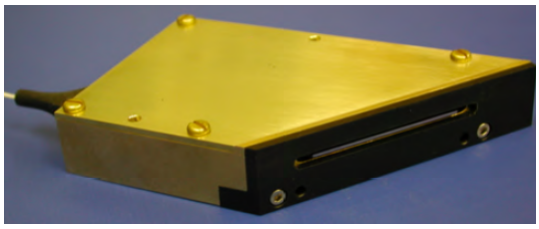

(b) Implemented device with size ∼7 cm. Taken from [13].

Figure 2.5: Integrated arrayed-waveguide grating. The input is an array of single-mode fibers. After propagation in the waveguide array light is spectrally dispersed at the output.

[7]. This poses serious problems in terms of cost and required precision. A possible solution is to employ the integrated photonic microspectrograph.

In its most basic form, a microspectrograph is constituted by a miniaturized arrayed-waveguide grating. At the input, an array of single-mode fibers brings light from the telescope focus to the device using a photonic lantern chip (see § 2.1.2). After free-space propagation, light is coupled into an array of single-mode waveguides with increasing length. They introduce a regular path difference between the fields. After another free-space propagation region, light is spectrally dispersed and the result collected by a slit. Thus, a frequency analysis of the source can be carried out. A scheme of the miniaturized arrayed-waveguide grating is shown in Fig. 2.5a.

The photonic lantern allows to completely decouple the spectrograph from the telescope: the device dependent size on the mirror diameter is thus broken [14]. The size of the device only depends on the waveguide array dimension, usually some centimeters [13]. Indeed, with the single-mode fibers acting as spatial filters, the device input light is now diffraction-limited, independently on the atmospheric seeing limitation.

The microspectrograph is a complete integrated device: once again in-

tegrated photonics ensures big advantages thanks to the high stability and scalability of the components.

A microspectrograph has been tested on the Anglo-Australian Telescope [15]. The device was fabricated with the silica-on-silicon technique. There is no possibility to exploit the third dimension, but since in this case only $2D$ devices have to be produced, this technique is a good candidate. Moreover, the silica-on-silicon approach is highly reproducible and allows for mass-production.

2.1.4 Frequency Conversion

Astronomy information is not limited to the visible/near-infrared spectrum. Many features in the night sky are present in the mid- or far-infrared regions[1], like useful information of exoplanets or protoplanetary disks. However, these spectral regions are more complex to investigate since the required components are not yet fully optimized, i.e. low performances are achieved [16].

Rather than developing this field and improve the devices performances, an original approach is to shift the acquired infrared light to shorter wavelengths, like in the visible or near-infrared [17]. In this regime the optical components for data acquisition and manipulation are greatly optimized and hence far less expensive.

The wavelength shift is operated through a sum-frequency generation process. It is a second-order non-linear effect where two photons at frequency ν_1 and ν_2 are annihilated producing a third photon at $\nu_3 = \nu_1 + \nu_2$. Consequently, the newly-generated photon has a shorter wavelength with respect to the other two.

The up-conversion takes place in a crystal; in particular, a lithium niobate crystal can be used. In order to increase the process efficiency the material should be periodically-poled, namely composed by regularly spaced ferroelectric domains with opposite orientation.

If distant celestial objects need to be observed, it is common use to study the interference of light from two or more telescopes in order to increase the angular resolution (more on that in § 2.1.5). Clearly, the up-conversion must take place on all the acquired light beams. When carrying out an interference phenomena, a high stability in all the arms is required in order to maintain the coherence of the incoming radiation. Therefore, a precise control of the conversion process is needed so to produce the same result on all the beams.

This is where integrated optics comes into play. Light propagates into the

[1] Farther away in the electromagnetic spectrum there are radio waves, but the acquisition techniques are quite different from what is discussed here.

(a) Karl G. Jansky Very Large Array. Image from https://public.nrao.edu/.

(b) Giant Magellan Telescope (3D rendering). Image from https://www.gmto.org/.

Figure 2.6: Comparison of a multi-telescope radio-interferometer and a multi-segment mirror telescope.

crystal by means of an integrated single-mode waveguide. In this way, the control on the up-conversion process is very stable and highly reproducible [17]. Moreover, the single-mode behavior of the guide allows to gain a first spatial filtering stage: it is possible to implement all the subsequent scheme in an all-fibered configuration [18].

The complete device, called ALOHA, has been tested on the CHARA telescope array (US) shifting from the near-infrared (1550 nm) to the visible (631 nm) [19]. A wider-spectrum shift is currently under laboratory study: from the mid-infrared (3.39 μm) to the near-infrared (810 nm) [18].

2.1.5 Light Combination

In § 2.1.3 the telescope angular resolution has been discussed. Eq. 2.1 shows that α can be decreased if the mirror diameter is expanded. However, D cannot be increased indefinitely for technical reasons: it is hard to keep an elevated surface quality for big mirrors. Also the cost is a determining factor.

A possible solution is to adopt more than one telescope. Combining light collected by all of them, it is possible to increase the minimum angular resolution by a factor B/D, where B (called *baseline*) is the distance between two telescopes. This is the basic concept of stellar interferometry (which will be discussed in detail in the following section, see § 2.2).

Stellar interferometry with radio-waves has been widely adopted since the last century. For example, the radio interferometer Very Large Array (New Mexico, US) is constituted by 27 radio-telescopes (see Fig. 2.6a). A similar concept, but extended through the Earth surface, allowed in April 2019 to observe the first supermassive black hole shadow with the Event Horizon Telescope [20].

When moving to shorter wavelength (infrared or even visible light), the setup precision has to increase dramatically. The delay lines used to combine the telescopes light must have a precision of fractions of the working wavelength. In this range it corresponds to few nm: it is very challenging to achieve such precision and stability with bulk instrumentation, sensitive to vibrations and temperature changes.

To this end, photonic technologies ensure huge advantages with respect to bulk optics. The devices produced are very compact and robust, allowing for an elevated thermo-mechanical resilience [21]. Furthermore, nanometric precision can be easily reached, thus ensuring the proper functioning of visible/infrared interferometers [22, 23]. On the other hand, bulk optics ensures a highly achromatic response [21], difficult to realize with integrated optics.

Another approach is to combine light signals coming from one single telescope in order to correct for the atmospheric wavefront distortion. In this case, interferometry is not used to increase the angular resolution, but rather to compensate the atmospheric disturbance, intrinsic in the measurement in a ground-based observatory. An example is the Giant Magellan Telescope under construction in Chile (see Fig. 2.6b).

Also in this context $3D$ photonic chips are a suitable choice. With integrated waveguides, separate regions of the telescope pupil can interfere. By properly customizing the waveguide geometry, it is possible to extract from the output intensity information about the incoming light, removing the atmospheric distortion [7].

Practical Implementations

A widely adopted technique to combine telescopes light is the ABCD method. By measuring the intensity at four different points of the interferometric pattern, information regarding the input light can be extrapolated [25].

The idea is to sample the output intensity at four points along the oscillation. Consider a two-beam combination scheme, for simplicity. The two input beams are equally divided in two; a $\pi/2$ phase shift is introduced in one of the four arms. Each line is then recombined with one among the two of the opposite input beam [26]. The $\pi/2$ phase shift is introduced so that the four sampled points cover one entire oscillation cycle, i.e. they are in quadrature. By measuring these four points, the amplitude and phase of the oscillation can be retrieved.

An ABCD combiner can be implemented with bulk optics but nowadays integrated ABCD interferometers are the most common choice. Concerning the latter, an implementation of the ABCD principle is shown in Fig. 2.7.

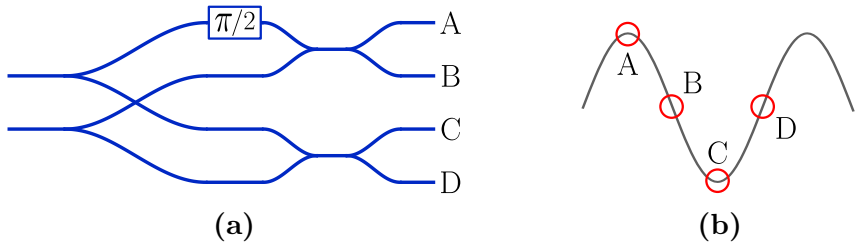

Figure 2.7: **(a)** Scheme for an integrated ABCD combiner. The two beams are split and then recombined with couplers, after a $\pi/2$ has been introduced to one arm. In **(b)** is shown the input intensity oscillation, with the four points (output of the device) have been sampled. Adapted from [24].

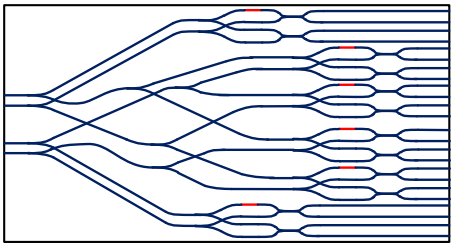

Figure 2.8: Scheme of GRAVITY: an integrated ABCD beam combiner, currently in use at the Very Large Telescope Interferometer (Chile). The red paths indicates a $\pi/2$ phase shift. Adapted from [27].

Since the couplers produce fields in phase opposition, the four device output ports are in quadrature, i.e. $\phi_B = \phi_A + \pi$, $\phi_C = \phi_A + \pi/2$ and $\phi_D = \phi_A + 3\pi/2$.

$2D$ integrated technologies are suitable since the devices only extend along two directions. For example, with the silica-on-silicon technology an ABCD device has been fabricated [24] and is currently in use in the GRAVITY instrument [27], on the Very Large Telescope Interferometer (Chile). A scheme of the integrated optics device is shown in Fig. 2.8.

Planar integrated photonics devices have been tested for combination of up to four telescopes. However, scaling up to larger structures rapidly increases the design complexity: the number of waveguides and hence of crossings rises exponentially [28].

In order to avoid waveguide-crossing in the ABCD scheme, a recent study [29] has added a third dimension, so a 3D fabrication technology is preferable to the standard photolitographic techniques. This new kind of device, called Discrete Beam Combiner (DBC), is at the basis of this work: for this reason, its functioning will be revised in the next sections. In order to do that, a deeper understanding of stellar interferometry is required.

2.2 Stellar Interferometry

The aim of this section is to employ stellar interferometry to recover the spatial and spectral features of a celestial body. Being very far from the Earth, the source can be treated as a $2D$ surface, belonging to a plane called source plane. A generic point on it can be indicated with $\boldsymbol{x} = (x_1, x_2)$.

The light emitted from the source can be described with its electric field $\boldsymbol{E} = \boldsymbol{E}(\boldsymbol{x}, t)$. Hereafter, $\boldsymbol{E}$ will be considered dimensionless for simplicity. It is also assumed a linear polarization along a fixed direction (belonging to the source plane), so that E can be treated as a scalar. The propagation direction is z.

In order to study the propagation of the electric field through space, it is convenient to introduce the formalism of the coherence function. Thus, instead of following the propagation of E, a more useful – and easier to treat – function will be analyzed. The *mutual coherence function* (MCF) between two fields at points A and B is defined as [30]:

$$\Gamma(\boldsymbol{x}_A, \boldsymbol{x}_B, \tau) = \left\langle E(\boldsymbol{x}_A, t+\tau) E^*(\boldsymbol{x}_B, t) \right\rangle \tag{2.2}$$

where * denotes the complex conjugate and $\langle \cdot \rangle$ the time average operator.

The MCF describes the correlation between the electric field at positions $\boldsymbol{x}_A = (x_{1,A}, x_{2,A})$ and $\boldsymbol{x}_B = (x_{1,B}, x_{2,B})$, in a time slot of τ. Clearly, if $\boldsymbol{x}_A = \boldsymbol{x}_B$ and $\tau = 0$, Eq. 2.2 gives the source intensity at position $\boldsymbol{x}_A$, called also photometry

$$I(\boldsymbol{x}_A) = \Gamma(\boldsymbol{x}_A, \boldsymbol{x}_A, 0) = \left\langle |E(\boldsymbol{x}_A, t)|^2 \right\rangle \tag{2.3}$$

Notice that from Eq. 2.2 it can be shown that

$$\Gamma(\boldsymbol{x}_A, \boldsymbol{x}_B, 0) = \Gamma^*(\boldsymbol{x}_B, \boldsymbol{x}_A, 0) \tag{2.4}$$

a property that will be useful later on.

The source intensity can also be computed by integrating the *spectral intensity* $I(\boldsymbol{x}, \nu)$ over the frequency domain

$$I(\boldsymbol{x}) = \int I(\boldsymbol{x}, \nu) \, \mathrm{d}\nu \tag{2.5}$$

The electromagnetic wave propagates through space and eventually reaches Earth, where the observation takes place. The plane where the telescope belongs to is called observation plane. A generic point on it can be indicated as $\boldsymbol{\xi} = (\xi_1, \xi_2)$. The distance between the source plane and the observation plane is z_0.

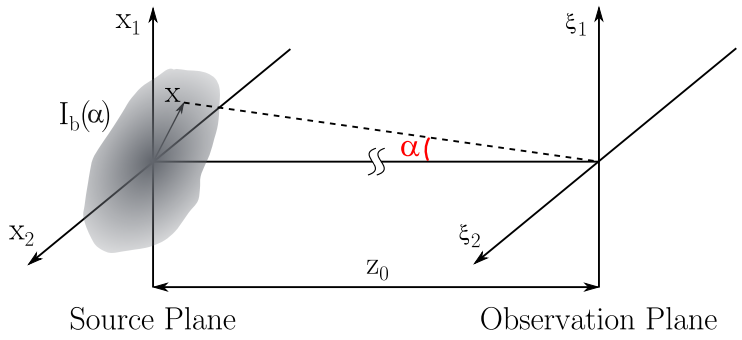

Figure 2.9: Geometry of the MCF propagation from the source to the observation plane. The distance between them is z_0. The source brightness distribution $I_b(\boldsymbol{\alpha})$ is a function of the angular coordinate $\boldsymbol{\alpha} = \boldsymbol{x}/z_0$.

In the following, instead of using $\boldsymbol{x}$, it is convenient to switch to $\boldsymbol{\alpha} = \boldsymbol{x}/z_0$. $\boldsymbol{\alpha}$ is the angular distance from the origin of the source plane, as represented in Fig. 2.9. This is possible since z_0 is surely much larger than the typical dimension of a star.

The problem is very complex to be treated exactly. However, with some expedients it can be greatly simplified [25]:

- The source emits thermal light which is, by definition, incoherent. This means that the emitted electric field is completely uncorrelated to itself, even for infinitely small distances in space and time. In other words, each point of the source radiates independently of its neighbors. This condition can be mathematically described as

$$|\Gamma(\boldsymbol{x}_A, \boldsymbol{x}_B, \tau)| = 0 \tag{2.6}$$

  unless $\boldsymbol{x}_A = \boldsymbol{x}_B$ and $\tau = 0$. From this property it directly follows that in the observation plane the MCF is function of coordinate differences only

$$\Gamma(\boldsymbol{\xi}_A, \boldsymbol{\xi}_B, \tau) = \Gamma(\boldsymbol{\xi}_A - \boldsymbol{\xi}_B, \tau) \tag{2.7}$$

- The observed light can be treated as quasi-monochromatic. This approximation is valid whenever the spectrum is sufficiently narrow, i.e. $\Delta\lambda \ll \lambda_0$, where λ_0 is the mean wavelength.

- The source shape is assumed independent of the emitted wavelength, over the observed spectrum. This is reasonable since the spectrum has been assumed sufficiently narrow. The spectral intensity can be written as the

product of the source brightness distribution and the source spectrum

$$I(\boldsymbol{\alpha}, \nu) = I_b(\boldsymbol{\alpha})G(\nu) \tag{2.8}$$

Consider also $G(\nu)$ as normalized: $\int G(\nu)\mathrm{d}\nu = 1$.

In order to describe the propagation of the MCF from the source plane to the observation plane, it is convenient to switch to the Fourier domain. The MCF is defined as the Fourier transform of the function $\hat{\Gamma}$, belonging to the Fourier space [25]:

$$\Gamma(\boldsymbol{x}_A, \boldsymbol{x}_B, \tau) = \mathcal{F}\left[\hat{\Gamma}(\boldsymbol{x}_A, \boldsymbol{x}_B, \nu)\right] = \int \hat{\Gamma}(\boldsymbol{x}_A, \boldsymbol{x}_B, \nu)e^{-i2\pi\nu\tau}\mathrm{d}\tau \tag{2.9}$$

The propagation of $\hat{\Gamma}$ can be derived applying the Rayleigh-Sommerfeld diffraction formula used in Fourier optics [31]:

$$\hat{\Gamma}(\boldsymbol{\xi}_A, \boldsymbol{\xi}_B, \nu) = \frac{1}{(\lambda z_0)^2}\iint_{\Sigma} \hat{\Gamma}(\boldsymbol{x}_A, \boldsymbol{x}_A, \nu)e^{ik(r_1 - r_2)}\mathrm{d}\boldsymbol{x}_A\mathrm{d}\boldsymbol{x}_B \tag{2.10}$$

which, employing Eqs. 2.7 (applied to $\hat{\Gamma}$) and 2.8, can be modified as

$$\hat{\Gamma}(\boldsymbol{\xi}_A - \boldsymbol{\xi}_B, \nu) = G(\nu)\int I_b(\boldsymbol{\alpha})e^{-ik(\boldsymbol{\xi}_A - \boldsymbol{\xi}_B)\cdot\boldsymbol{\alpha}}\,\mathrm{d}\boldsymbol{\alpha} \tag{2.11}$$

Using the quasi-monochromatic approximation, the term $I_b(\boldsymbol{\alpha})e^{-ik(\boldsymbol{\xi}_A - \boldsymbol{\xi}_B)\cdot\boldsymbol{\alpha}}$ becomes wavelength-independent over the observed spectrum. The MCF at the observation plane can be retrieved by anti-Fourier transforming Eq. 2.11

$$\begin{aligned}\Gamma_{qm}(\boldsymbol{\xi}_A - \boldsymbol{\xi}_B, \tau) &= e^{-i2\pi\nu_0\tau}\int I_b(\boldsymbol{\alpha})e^{-ik_0(\boldsymbol{\xi}_A - \boldsymbol{\xi}_B)\cdot\boldsymbol{\alpha}}\mathrm{d}\boldsymbol{\alpha} = \\ &= \Gamma_{qm}(\boldsymbol{\xi}_A - \boldsymbol{\xi}_B, 0)e^{-i2\pi\nu_0\tau}\end{aligned} \tag{2.12}$$

The last equality contains a fundamental result, called *van Cittert-Zernike theorem*

$$\Gamma_{qm}(\boldsymbol{\xi}_A - \boldsymbol{\xi}_B, 0) = \int I_b(\boldsymbol{\alpha})e^{-ik_0(\boldsymbol{\xi}_A - \boldsymbol{\xi}_B)\cdot\boldsymbol{\alpha}}\mathrm{d}\boldsymbol{\alpha} \tag{2.13}$$

In other words, knowing the MCF in the observation plane (at $\tau = 0$) it is possible, by anti-Fourier transforming, to retrieve the brightness distribution of the source. Eq. 2.13 is more commonly represented in its normalized form

$$\mu(\boldsymbol{\xi}_A - \boldsymbol{\xi}_B) = \frac{\Gamma_{qm}(\boldsymbol{\xi}_A - \boldsymbol{\xi}_B, 0)}{\sqrt{I(\boldsymbol{\xi}_A)I(\boldsymbol{\xi}_B)}} = \frac{1}{I_0}\int I_b(\boldsymbol{\alpha})e^{-ik_0(\boldsymbol{\xi}_A - \boldsymbol{\xi}_B)\cdot\boldsymbol{\alpha}}\mathrm{d}\boldsymbol{\alpha} \tag{2.14}$$

where $I_0 = \int I_b(\boldsymbol{\alpha})\mathrm{d}\boldsymbol{\alpha}$ is the total intensity emitted from the source.

$\mu(\boldsymbol{\xi}_A - \boldsymbol{\xi}_B)$ is called visibility of the interferometer. Being a complex function, it can be described by its modulus and phase as

$$\mu(\boldsymbol{\xi}_A - \boldsymbol{\xi}_B) = V(\boldsymbol{\xi}_A - \boldsymbol{\xi}_B)e^{i\varphi(\boldsymbol{\xi}_A - \boldsymbol{\xi}_B)} \tag{2.15}$$

Since I_b is real and positive (otherwise no physical meaning can be assigned to it), μ is an hermitian function. In other words

$$\begin{aligned} V(\boldsymbol{\xi}_A - \boldsymbol{\xi}_B) &= V(\boldsymbol{\xi}_B - \boldsymbol{\xi}_A) \\ \varphi(\boldsymbol{\xi}_A - \boldsymbol{\xi}_B) &= -\varphi(\boldsymbol{\xi}_B - \boldsymbol{\xi}_A) \end{aligned} \tag{2.16}$$

Finally, notice that the spectral intensity at the observation plane is

$$I(\boldsymbol{\xi}, \nu) = \hat{\Gamma}(\boldsymbol{\xi}, \boldsymbol{\xi}, \nu) = \hat{\Gamma}(\boldsymbol{\xi} - \boldsymbol{\xi}, \nu) = \hat{\Gamma}(0, \nu) = G(\nu) \int I_b(\boldsymbol{\alpha})\ \mathrm{d}\boldsymbol{\alpha} = G(\nu) I_0$$

Integrating this relation with respect to the frequency ν, it is possible to obtain the intensity at the observation plane: $I(\boldsymbol{\xi}) = I_0$, which is constant. The star sheds its light homogeneously on Earth's surface. This is why the information about the source shape and brightness distribution can only be obtained studying the MCF, and not simply by collecting the observed intensity.

The purpose of stellar interferometry is to characterize the visibility function $\mu(\boldsymbol{\xi}_A - \boldsymbol{\xi}_B)$. As can be seen from Eq. 2.14, two telescopes with distance $\boldsymbol{B} = \boldsymbol{\xi}_A - \boldsymbol{\xi}_B$ can be used to retrieve a particular spatial frequency component of the MCF. $\boldsymbol{B}$ is the baseline of the two telescopes and the corresponding spatial frequency is $\boldsymbol{B}/\lambda$.

It is important to sample the highest number of baseline possible (without increasing too much the setup complexity) since the denser is the sampling of the spatial spectrum and the better will be the quality of the reconstructed image [25].

More baselines can be sampled taking advantage of the Earth rotation: this induces a variation in the baseline orientation. Another technique is to add more telescopes to the interferometer. With N_t telescopes, the number of baselines is [32]:

$$N_b = \frac{N_t(N_t - 1)}{2} \tag{2.17}$$

Finally, also changing the wavelength allows to scan different baselines (provided the object structure is wavelength-independent) [25]. These three techniques are usually combined together in the most powerful instruments in order to sample the highest number of spatial frequencies as possible.

As already explained in §2.1.5, in this work only one telescope is considered. The interferometry measurement is carried out on light coming from various places of the single mirror. Different baselines are defined as different point-to-point distances on the mirror. This is done to correct for the wavefront distortion introduced by the atmospheric turbulence. In the following, this choice is justified and explained in detail.

2.2.1 Atmospheric Turbulence

Light from a distant star has a plane wavefront until it reaches Earth. Here, due to turbulent motion of the atmospheric layer, the wavefront is perturbed and gets distorted: both the amplitude and the phase of the incoming field are modified. These deformations take place in a millisecond time range [33].

On small spatial scales, the distorted wavefront can be considered as locally planar. This can be quantified introducing the *Fried parameter* r_0 [2]. It is wavelength dependent: $r_0 \propto \lambda^{1.2}$, with a value of tens of centimeters in the visible/near-infrared spectrum. Due to atmospheric distortion, a telescope with diameter bigger than r_0 will behave as a r_0-diameter one [34].

The angular resolution is greatly compromised and the observation becomes seeing-limited, instead of diffraction-limited. A method to eliminate this effect is imperative, otherwise practically no celestial object can be resolved.

A first solution is to employ a telescope orbiting around the Earth, outside the atmosphere, like the Hubble Space Telescope. The non-modified wavefront can thus be collected, without the atmosphere perturbation. The main problem is the difficulty in maintaining the instrument. Moreover, mirrors up to 10 m of diameter can be used, for technical difficulties in the transport.

If a ground-based telescope has to be used, correction techniques have to be adopted. Atmospheric turbulence can be compensated with an electro-optical system that measures and corrects the wavefront distortion [33]. It should operate on a sub-millisecond time scale, so to effectively remove the turbulence. The system, commonly referred to as adaptive optics scheme, is depicted in Fig. 2.10.

The distorted wavefront is collimated onto a deformable mirror. The latter is divided in many smaller mirrors, usually of hexagonal shape. Each of them is controlled by a piezoelectric actuator, which redirects its orientation. An example of a deformable mirror can be found in the inset of Fig. 2.10, where 37 hexagonal mirrors are used.

Following the mirror, part of the light is separated and redirected onto a wavefront sensor. It measures the local distortion of the wavefront and the

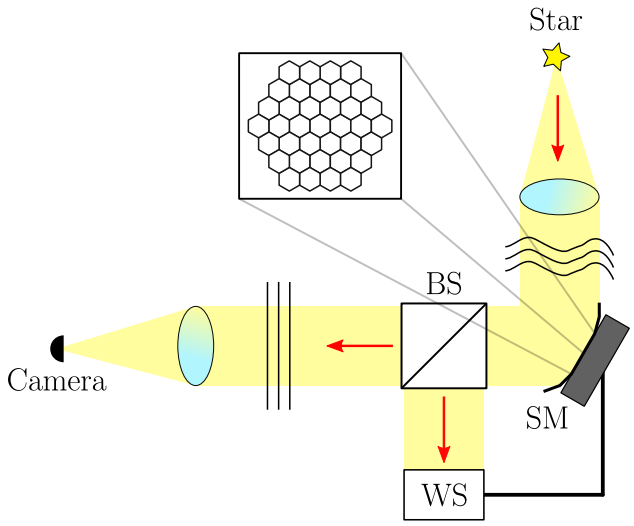

Figure 2.10: Adaptive optics scheme. The distorted wavefront is acquired by a control system which – working in a closed feedback loop – compensates the distortion. In the inset, a segmented mirror is shown. BS = Beam Splitter, SM = Segmented Mirror, WS = Wavefront Sensor.

result is used to control – in a closed feedback loop – the deformable mirror actuators. The process is repeated until the flat wavefront is retrieved.

However, if the celestial object is too dim or extended (or both), a guide star is required in order to monitor the turbulence with a high signal-to-noise ratio. This reference star should be sufficiently bright (in order to produce sufficient flux) and near the observed one. The latter requirement is needed so that the two stars are located within the same r_0 at the atmosphere level ($\sim$10 km is the mean height of the turbulent layer). This corresponds to an angular distance (called isoplanatic angle) of $\sim$5 arcsec [33]. It is clear that these requirements are way too stringent: only a tiny portion of the night sky would be observable.

In 1985, it was proposed to use artificial stars created with lasers as reference objects [35], called nowadays laser-guide star. A laser beam is shone in the stratosphere where molecules back-scatter portion of the light, which is then recollected by the telescope. A more modern scheme is to shine the laser upper in the mesosphere to collect the resonant scattering of sodium atoms [33]. An example of the latter is shown in Fig. 2.11, at the Very Large Telescope (Chile).

The methods discussed so far are only able to correct for the amplitude distortions of celestial light. However, this is not enough to correctly reconstruct

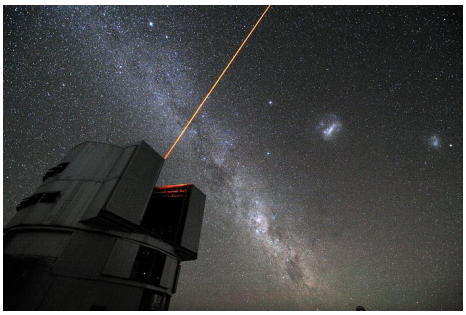

Figure 2.11: Laser-guide star at the Very Large Telescope in Chile. Image from https://www.eso.org/public/.

the visibility function: the original phase has to be acquired too. This is possible with the closure phase approach, a method born with radio-astronomy, successfully applied also to optical imaging [36].

The idea is to apply a mask at the re-imaged telescope aperture plane in order to select only specific points of the segmented mirror (see Fig. 2.10). This technique is called aperture masking interferometry: a single telescope is used as a miniaturized interferometer. By measuring the relative phase for each points pair, it is possible to reconstruct the original field phase already subtracting the atmospheric turbulence.

Consider three of such points: A, B and C. Only one of them, say A, has a phase delay introduced by the atmospheric turbulence, as represented in Fig. 2.12. The detected intensity fringes at the baseline AB will have a certain shift (dependent on the delay) if compared to the ideal non-perturbed situation. The observed phase shift along the baseline $\boldsymbol{B}_{AB}$ can be represented as

$$\phi_{AB}^{obs} = \phi_{AB} + \psi_{AB} \tag{2.18}$$

where ϕ_{AB} is the intrinsic celestial object phase shift and ψ_{AB} is the perturbation introduced by the atmosphere.

The same reasoning can be done on the baseline $\boldsymbol{B}_{AC}$

$$\phi_{AC}^{obs} = \phi_{AC} + \psi_{AC} \tag{2.19}$$

where $\psi_{AC} = -\psi_{AB}$ [37]. On the other hand, no shift is detected when observing the baseline $\boldsymbol{B}_{BC}$, i.e. $\phi_{BC}^{obs} = \phi_{BC}$.

It is clear that the sum of the three observed phases – called closure phase – is insensitive to the A phase delay introduced by the atmosphere: it depends only on the source features. This holds for arbitrary phase delays and on any of the three points. The procedure can be repeated for any set of three points between all the ones constituting the mask [2, 38].

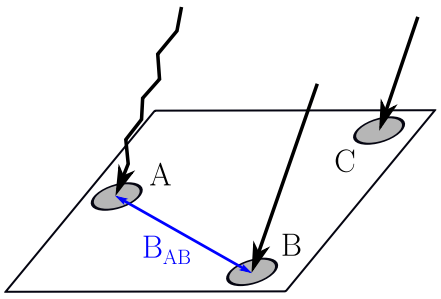

Figure 2.12: Closure phase scheme with three segmented mirror points. Only the position A is affected by the atmospheric turbulence. The baseline $\boldsymbol{B}_{AB}$ is also shown. Adapted from [37].

2.3 Discrete Beam Combiner

The DBC is a beam combiner device used to encode phase variations into intensity variations. Indeed, as has been discussed in § 2.2, the starlight reaching the Earth's surface is constant, so that no immediate information can be collected from it. Combining optical fields it is possible to observe an interference pattern, which carries the necessary source information.

In order to retrieve the source brightness distribution (i.e. its shape and intensity), the visibility function has to be reconstructed (see Eq. 2.13). This is done by sampling the acquired light at the observation plane, where the telescope mirror is placed. Its functionality and shape has been already discussed in § 2.2.1. It is composed by different sub-mirrors, each of which can be seen as a local source of light.

This is the plane where the Fourier sampling takes place. Source pairs are combined together and their MCF is computed. Such MCF refers to a given baseline, i.e. the distance between the considered points in the observation plane. The more are the pairs considered and the more precise is the global MCF reconstruction. Indeed, to any baseline it corresponds a unique spatial frequency. The more are the baseline considered and the more are the spatial frequencies mapped. Hence, the more accurate is the Fourier space reconstruction [23]. The drawback is the increased complexity of the interferometric setup.

Notice that two pairs having the same baseline – both modulus and direction – give the same amount of information to the reconstruction. Indeed, the MCF depends on vectorial coordinate-differences only (see Eq. 2.7), provided the quasi-monochromatic approximation holds [25]. Aperture masking is used to select only the required points from the segmented mirror in order to acquire only non-redundant baselines.

For each baseline, the fields are interfered so that the amplitude and phase of the incoming field are obtained. While the former has been already corrected

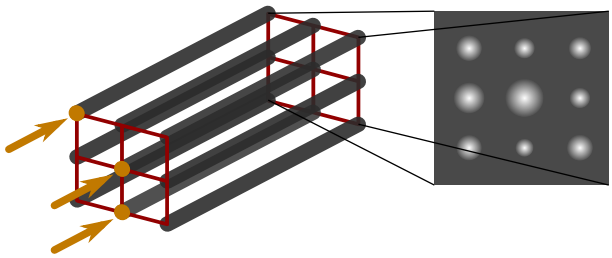

Figure 2.13: Graphical representation of a square DBC with $N = 9$ and $M = 3$. Light is injected in three waveguides and after propagation the output pattern is collected with a photodetector.

thanks to the adaptive optics system, the latter can be reconstructed with the closure phase technique (see 2.2.1). The interferometer operation is carried out by the DBC, whose inputs are the fields exiting the aperture mask.

Here follows the mathematical description of a DBC, composed by an array of waveguides. The basic working principle of the device is that light couples between neighboring waveguides, ensuring an energy transfer through the whole structure.

2.3.1 Mathematical Description

Consider an array of N waveguides, with a given configuration. The following theory holds whatever is the array geometry. Injected into it, there are M electric fields, one in a unique waveguide. Clearly, $M \leq N$.

When light is injected in a waveguide, it spreads to neighboring sites during propagation, provided the waveguides are sufficiently close. If more inputs are excited, the output intensity configuration represents the interference mix of all the input fields. Such intensity pattern depends on the array geometry, on the length of the waveguides and on the excited sites [39]. An example of a device with square geometry is represented in Fig. 2.13.

Since the waveguides produced by the FLM technique (see Ch. 3) have low refractive index contrast, the coupling between neighboring waveguides is weak (provided also the waveguides are not too close to each other). Therefore, light propagation can be modeled within the frame of the *coupled mode equations* [40], explained in detail in App. A. The system of equations describing the propagation of light inside two neighboring waveguides has been obtained (see Eq. A.10).

In the present context, it is necessary to generalize the coupled mode equations to more than two waveguides. In the case of N identical waveguides, the

system of differential equations A.10 can be written as

$$i\,\frac{\mathrm{d}A_n}{\mathrm{d}z} = \sum_{m\neq n}^{N} \kappa_{n,m} A_m \tag{2.20}$$

where A_n is the electric field amplitude in the n-th waveguide along the propagation direction z. $\kappa_{n,m}$ is the *coupling coefficient*, describing the coupling between the n-th and m-th modes. They are defined as the normalized overlap integral between the transverse mode profiles $\psi_i(x,y)$ propagating in the waveguides

$$\kappa_{n,m} = \frac{k_0^2}{2\beta} \frac{\iint \psi_m \Delta n_m^2 \psi_n^* \mathrm{d}x\mathrm{d}y}{\iint \psi_m \psi_n^* \mathrm{d}x\mathrm{d}y} \tag{2.21}$$

where $k_0 = 2\pi/\lambda$ is the wavenumber and $\beta = (2\pi/\lambda)\Delta n$ the propagation constant. $\Delta n = n - n_0$ is the refractive index contrast between the waveguide core and the substrate. Notice that the array is composed by identical waveguides so that Δn is the same for all of them.

For a discrete set of points, the MCF can be defined as

$$\Gamma_{j,k} = \big\langle A_j(0) A_k^*(0) \big\rangle, \qquad j,k = 1,...,M \tag{2.22}$$

where Eq. 2.2 (with $\tau = 0$) has been employed. The pair of indexes (j,k) are used to indicate a given baseline; they play the role of the coordinate vector $\boldsymbol{\xi}_A - \boldsymbol{\xi}_B$.

Moreover, it can be showed that the peak intensity J_n carried by the n-th mode is a linear combination of all possible MCFs[2] of the M input fields [41]

$$J_n = \big\langle |E_n|^2 \big\rangle = \sum_{j=1}^{M} \sum_{k=1}^{M} \Big[a_{n,j}(z) a_{n,k}^*(z) \Big] \Gamma_{j,k} \tag{2.23}$$

where $a_{n,j}(z)$ are a function of the array geometry and device length [28]. They represent the input-response function of the array and they can be computed by direct integration of Eq. 2.20, or experimentally, as will be shown in § 4.4. In other words, $a_{n,j}(z)$ is the field amplitude of the n-th mode – at propagation distance z – resulting from the excitation of the j-th waveguide.

Eq. 2.23 already shows the DBC functionality: the output intensity is connected to the input fields correlation through the array geometry.

However, it is common use to remap it in terms of real-valued variables. Knowing that for a complex number x its real and imaginary part can be

[2] Actually, $\Gamma_{j,k}$ is called mutual coherence function only when $j \neq k$. When $j = k$, $\Gamma_{j,k}$ is the photometry (or intensity).

expressed as $\mathbb{R}\mathrm{e}[x] = (x + x^*)/2$, $\mathbb{I}\mathrm{m}[x] = (x - x^*)/2\,i$ and using Eq. 2.4, it is possible to show that Eq. 2.23 can be reformulated as

$$J_n = \sum_{j=1}^{M}\sum_{k=1}^{M}\left(\mathbb{R}\mathrm{e}\left[a_{n,j}a_{n,k}^*\right]\mathbb{R}\mathrm{e}\left[\Gamma_{j,k}\right] - \mathbb{I}\mathrm{m}\left[a_{n,j}a_{n,k}^*\right]\mathbb{I}\mathrm{m}\left[\Gamma_{j,k}\right]\right) =$$
$$= \sum_{k=1}^{M}|a_{n,k}|^2\Gamma_{k,k} + 2\sum_{j=1}^{M-1}\sum_{k\neq j}^{M}\left(\mathbb{R}\mathrm{e}\left[a_{n,j}a_{n,k}^*\right]\mathbb{R}\mathrm{e}\left[\Gamma_{j,k}\right] - \mathbb{I}\mathrm{m}\left[a_{n,j}a_{n,k}^*\right]\mathbb{I}\mathrm{m}\left[\Gamma_{j,k}\right]\right) \tag{2.24}$$

Eq. 2.24 can be written more succinctly in matrix form if the following transformations are adopted [42]

$$\begin{aligned} b_{n,k} &= |a_{n,k}|^2, \quad k = 1, ..., M \\ b_{n,j+(k-1)(k-2)/2+M} &= 2\,\mathbb{R}\mathrm{e}\left[a_{n,j}a_{n,k}^*\right], \quad j < k, \quad k = 2, ..., M \\ b_{n,j+(k-1)(k-2)/2+M(M+1)/2} &= -2\,\mathbb{I}\mathrm{m}\left[a_{n,j}a_{n,k}^*\right], \quad j < k, \quad k = 2, ..., M \end{aligned}$$

$$\begin{aligned} G_k &= \Gamma_{k,k}, \quad k = 1, ..., M \\ G_{j+(k-1)(k-2)/2+M} &= \mathbb{R}\mathrm{e}\left[\Gamma_{j,k}\right], \quad j < k, \quad k = 2, ..., M \\ G_{j+(k-1)(k-2)/2+M(M+1)/2} &= \mathbb{I}\mathrm{m}\left[\Gamma_{j,k}\right], \quad j < k, \quad k = 2, ..., M \end{aligned}$$

Thus, Eq. 2.24 now becomes

$$J = \underline{\underline{V2PM}}\; G \tag{2.25}$$

where J is the column vector containing the N output intensity values and G the column vector of the G_i terms. $V2PM$, called *visibility-to-pixel matrix*, is the $N \times N$ matrix containing the $b_{n,m}$ coefficients. It is the matrix connecting the MCF with the device output intensity.

The aim of a DBC is to retrieve the unknown G vector by measuring the J terms. The $V2PM$ can be extracted experimentally (see § 4.4), so that G can be obtained from Eq. 2.25 as

$$G = \underline{\underline{P2VM}}\; J \tag{2.26}$$

where the $P2VM$ (called *pixel-to-visibility matrix*) is the Moore-Penrose pseudo-inverse of $V2PM$. Notice that since in general the $V2PM$ is a rectangular matrix[3]: its inverse cannot be defined in the usual sense, but a pseudo-inverse has to be computed [43].

[3]The $V2PM$ is a square matrix only in the condition $N = M^2$.

Notice that Eq. 2.26 can be evaluated provided $P2VM$ exists and is well-conditioned. The latter condition requires the $V2PM$ to have a low *condition number* (CN). Such value is defined, for an invertible matrix, as [44]:

$$CN = \frac{maximum\ \ singular\ \ value}{minimum\ \ singular\ \ value} \tag{2.27}$$

The condition number is a measure of how much a change in the input affects the output of a process. Therefore, a matrix with a low condition number ensures a higher stability of the input-output transformation. Usually, a low value of CN is smaller than 10. Indeed, $CN = 10$ means that if the output intensities J_n are measured with a 1% precision, the maximum error on the retrieved G_n is 10% [42].

The M input fields configuration and the waveguides geometry (i.e. how the waveguides are placed one near the other in space) are chosen in order to produce a $V2PM$ with the lowest possible condition number. Moreover, also the device length strongly impacts such parameter.

For a given array geometry, the input configuration and device length ensuring the lowest condition number can be found by direct numerical evaluation. The field distribution is computed for all the possible configurations at many length and the condition number of the corresponding $V2PM$ is obtained. However, the computational time of the algorithm scales rapidly with the waveguides number considered in the array [45].

Once the MCF of the input fields has been experimentally extrapolated, it is possible to reconstruct the visibility function (see Eq. 2.14). As already explained, the observation plane is constituted by a discrete set of points rather than a continuous one. The coordinate vector $\boldsymbol{\xi}$ has to be substituted with a discrete index. The visibility modulus and phase can then be reformulated as

$$V_{j,k} = \sqrt{\frac{(\mathbb{R}\mathrm{e}[\Gamma_{j,k}])^2 + (\mathbb{I}\mathrm{m}[\Gamma_{j,k}])^2}{\Gamma_{j,j}\Gamma_{k,k}}}, \qquad j \neq k \tag{2.28}$$

$$\varphi_{j,k} = \arctan \frac{\mathbb{I}\mathrm{m}[\Gamma_{j,k}]}{\mathbb{R}\mathrm{e}[\Gamma_{j,k}]}, \qquad j \neq k \tag{2.29}$$

where $\Gamma_{j,k}$ is the MCF between fields at points j and k (see Eq. 2.22).

2.3.2 Configuration Examples

The first beam combiner studied was constituted by a square array of waveguides [42]. In the simplest condition, the input fields are M and the waveguides

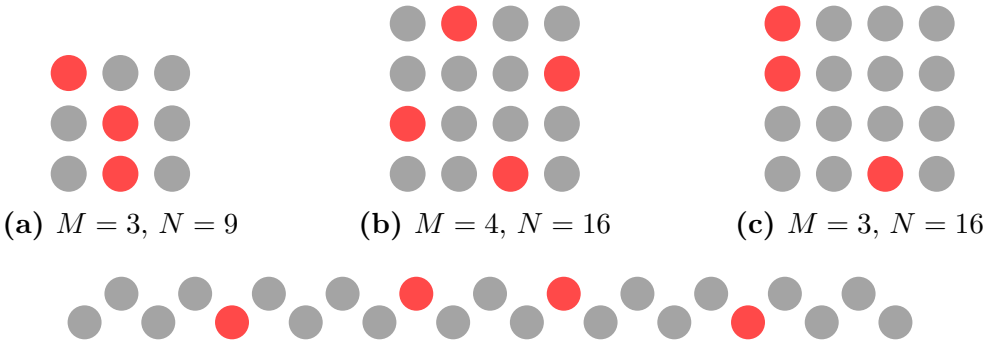

(a) $M = 3$, $N = 9$ **(b)** $M = 4$, $N = 16$ **(c)** $M = 3$, $N = 16$

(d) $M = 4$, $N = 23$

Figure 2.14: Schematic representation of the best configurations (i.e. lowest condition number) for various DBCs. M is the number of inputs, N the total number of waveguides. **(a)**, **(b)** and **(c)** are square arrays; **(d)** a zigzag one. Notice that in the last two situations $N < M^2$.

$N = M^2$. The $V2PM$ is therefore a square matrix. It has been found that the coupling of waveguides beyond the nearest neighbor ones has a dramatic impact on the retrieval of the MCF [41]. In order to increase such type of coupling, it is preferable to use a $2D$ configuration of waveguides: this is why a $1D$ geometry has not been studied.

With such geometry, the best input configurations for $M = 3$ and $M = 4$ have been found by direct numerical evaluation. They are are represented in Fig. 2.14a and Fig. 2.14b. The condition numbers associated to the corresponding $V2PM$ are 8.3 and 7.7, respectively [28].

It has also been shown that using $N > M^2$ can decrease the condition number, thus producing a better configuration. An example with $M = 3$ and $N = 16$ is represented in Fig. 2.14c with condition number equal to 3 [28].

In 2016, Diener *et al.* showed that with a zigzag configuration of waveguides, lower condition number values can be reached [22]. Such structure can be created by superimposing two linear arrays, one above the other, shifted by half the distance between two waveguides. An example with $M = 4$ and $N = 23$ is shown in Fig. 2.14d, with condition number equal to 3.8 [22].

The first-order coupling is in the diagonal direction, while the second-order one is along the horizontal direction. This can be understood by ideally pushing down the upper plane so to have all the waveguides on the same plane. The nearest neighbor to any waveguide is a waveguide belonging to the opposite plane.

Two coupling coefficients can be defined. Waveguides on the same plane

exchange energy through the *horizontal* coupling coefficient κ_h. Waveguides on opposite planes through the *diagonal* coupling coefficient κ_d. Higher-order couplings are neglected.

A further advantage of the zigzag configuration is the ease with which the output can be spectrally analyzed. The DBC output can be directly interfaced to a spectrograph, without the need of additional instruments [22]. This is because of the geometry of the array (see Fig. 2.14d): light exiting each waveguide can be dispersed vertically, with no overlap between the fields. On the other hand, the square geometry requires to redirect the output in a linear fashion, in order to be acquired by the spectrograph. This passage intrinsically introduces additional losses to the device [22].

Chapter 3

Femtosecond Laser Micromachining

This chapter is devoted to the theoretical foundations of the *Femtosecond Laser Micromachining* (FLM) technique. It is a method widely adopted from the first years of this century to fabricate waveguides inside a glass substrate.

Another common technique is photolitography where a given pattern is transferred from an optical mask onto a substrate – usually silicon or silica. Even if very compact devices can be created, they can only explore a $2D$ surface, preventing the possibility of exploiting the third dimension. Moreover, sophisticated facilities are required [46].

These issues are solved employing FLM.

A general introduction on the main advantages of FLM will be presented, followed by an analysis of the mechanism of writing inside glass. After that, a review of the main parameters upon which the fabrication depends will be showed. Finally, a thermal treatment able to increase the quality of the fabricated structures will be discussed.

3.1 Overview

The idea at the basis of FLM dates back to 1996, when it has been showed that by focusing a femtosecond laser beam into a dielectric material, a permanent modification of the latter can be induced [47]. Only a small region of the sample is modified, corresponding to the volume where the beam is focused. In particular, the optical properties of such small volume are modified: by properly tailoring the process, a smooth positive refractive index change can be induced. Such structure can be used to efficiently guide light, creating an

optical waveguide inside the bulk of the glass.

Simply by increasing the energy delivered by each pulse, other structures can be fabricated. For example, it is possible to induce nanogratings that, after a chemical etching, allow the formation of buried microchannels, widely used in microfluidic applications [48].

The main advantages of FLM can be resumed into four points:

- $3D$ structures can be fabricated, exploiting the depth degree of freedom.
- The optical modification is limited to the focal volume – the small region where the beam is focused.
- It is a direct-writing technique, thus reducing the cost and complexity of the process (e.g. no clean-room required).
- It can be used on many different substrates, like glasses, crystalline materials and polymers.

However, there are also disadvantages. The refractive index contrast that can be induced with FLM ($\Delta n \sim 10^{-3}$) is lower with respect to one generated by photolitography. Therefore, it is very difficult to reduce the propagation loss (see 4.3.2) of FLM waveguides below $0.1-0.2$ dB/cm, while in photolitography a value of 0.1 dB/cm can be easily reached [46]. Moreover, FLM waveguides have a higher minimum curvature radius achievable, thus limiting the compactness of the devices to be fabricated.

3.2 Light-Matter Interaction

3.2.1 Free-Electron Plasma Formation

In a transparent material, visible radiation cannot be linearly absorbed. Such photons have not sufficient energy to promote an electron from the valence band to the conduction band. Indeed, the band gap of such materials is around 5 eV, while the highest energy brought by a visible photon is 3 eV.

In order for the light to be absorbed, nonlinear absorption mechanisms – involving more than one photon – are needed. The laser can thus interact with the material, depositing energy into it.

There are two classes of nonlinear mechanisms that allow this interaction to take place: nonlinear photoionization and avalanche ionization [49].

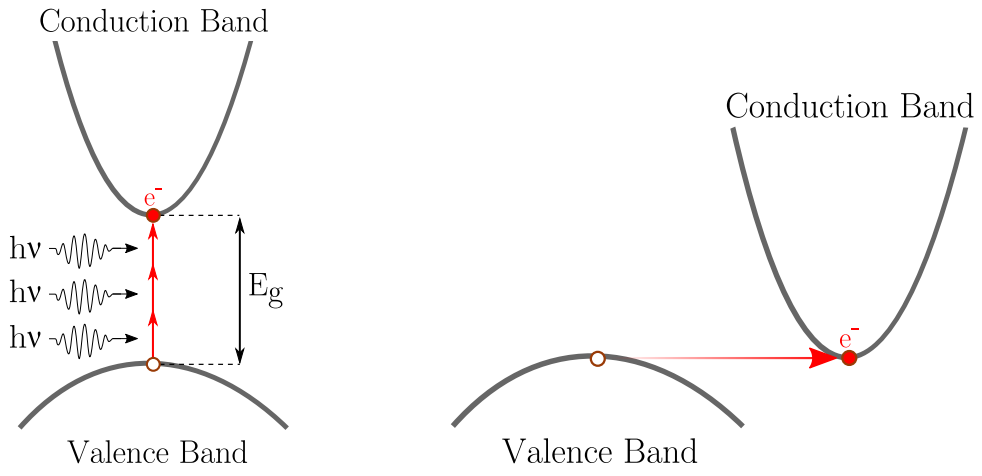

(a) Multiphoton ionization. **(b)** Tunneling ionization.

Figure 3.1: Nonlinear photoionization mechanisms. The full red dot indicates an electron; the empty dot, a vacancy. E_g is the energy band gap between the valence band maximum and the conduction band minimum. Adapted from [46].

Nonlinear Photoionization

Photoionization is the excitation of an electron from the valence band to the conduction band, driven by the laser electric field. Two different regimes exist, depending on the value of the beam intensity. At low intensity, the dominant regime is the *multiphoton ionization* where an electron in the valence band simultaneously absorbs several photons, as in Fig. 3.1a. The minimum number of photons m required can be computed with $mh\nu \geq E_g$, where E_g is the energy band gap of the material.

At high laser intensity, the strong electric field can distort the band structure, reducing the energy gap between valence and conduction band. A valence electron can then tunnel into the conduction band, as in Fig. 3.1b. This is called *tunneling ionization*.

When the intensity is in a middle region between the two regimes, photoionization is a combination of the two mechanisms: the band structure is distorted, but more than one photon is still needed to overcome the energy barrier.

These two regimes obey to the same fundamental principles. It is possible to distinguish between the two, in a more quantitative way, introducing the

Keldysh parameter [50]:

$$\gamma = \frac{2\pi\nu}{e}\sqrt{\frac{m_e c n \varepsilon_0 E_g}{I}} \tag{3.1}$$

where ν is the laser frequency, I the laser intensity, E_g the energy band gap of the material, e the electron charge, m_e the effective electron mass, c the light speed in vacuum, n the refractive index and ε_0 the vacuum permittivity.

When $\gamma \gg 1.5$ the dominant process is multiphoton ionization. When $\gamma \ll 1.5$ it is tunneling ionization [49].

Notice that γ depends not only on the intensity, but also on the laser frequency ν. Therefore, the multiphoton ionization is dominant whenever the beam intensity is low and the frequency sufficiently high – but still below the value sufficient for linear photon absorption. Similarly, tunneling ionization requires high intensity and low frequency.

Example 1. $\lambda = 1030$ nm, $n = 1.5$, $E_g = 5$ eV, $I = 10$ TWcm^{-2}. *Eq. 3.1 gives* $\gamma \sim 1$, *meaning that the photoionization is in this case a mix between the two regimes. These are values typical in a waveguide fabrication in a dielectric material like glass.*

The photoionization rate W, i.e. the number of valence electrons promoted to the conduction band in a second, strongly depends on the laser intensity [51]. In the multiphoton ionization regime $W \propto I^m$, with m the number of photons. In the tunneling regime, the dependence is more weak, while still not linear [52].

Avalanche Ionization

An electron in the lowest energy level of the conduction band can linearly absorb – sequentially – several photons. It can eventually reach an energy level exceeding the conduction band minimum by more than the band gap. Such electron may then collide with a valence electron, promoting the latter to the conduction band. The two electrons are thus positioned in the conduction band minimum (Fig. 3.2, right panel). Each of these electrons can start the process again from the beginning, as long as the laser beam is present and strong enough. This phenomenon gives rise to an avalanche of electrons, hence the name *avalanche ionization*.

Avalanche ionization requires some electrons to be initially present in the conduction band minimum. Such electrons can be provided either from a multiphoton ionization or from tunneling ionization [49]. For this reason,

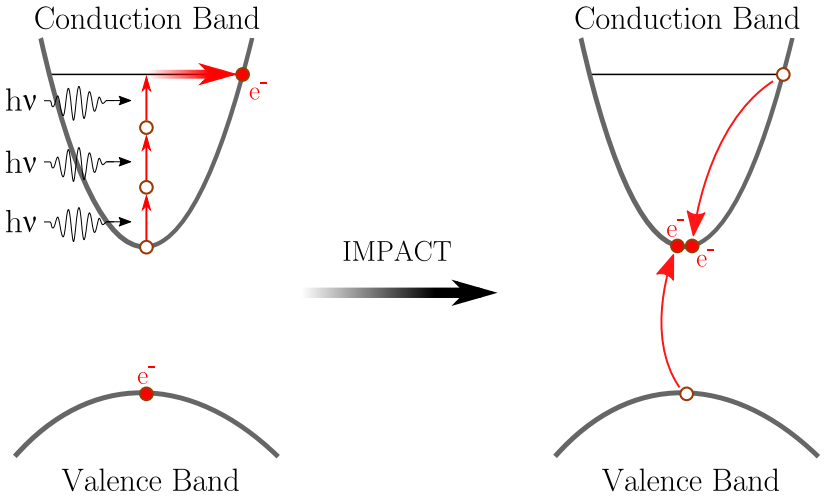

Figure 3.2: Avalanche ionization. Left panel: free-carrier absorption. Right panel: impact ionization, ending up with the two electrons in the conduction band minimum. Adapted from [46].

the process is deterministic since no defect electrons are needed to seed the absorption [53]. This allows a controlled and reproducible phenomenon [54].

At the beginning of the avalanche ionization process, just few electrons are present in the conduction band. They form an electron plasma, with a low electron density N. For this reason, the plasma frequency is lower than the laser frequency: $\omega_p < \omega_L$. Here $\omega_L = 2\pi\nu$ and the plasma frequency ω_p is defined as

$$\omega_p = \sqrt{\frac{Ne^2}{m_e \varepsilon_0}} \tag{3.2}$$

When $\omega_p < \omega_L$ holds, the plasma created at the beam focus is transparent to the laser radiation.

While the process progresses, the electron density grows until it reaches the critical value N_C, defined as the value N satisfying $\omega_p = \omega_L$:

$$N_C = \frac{m_e \varepsilon_0}{e^2}\,\omega_L^2 \tag{3.3}$$

From this point on, the plasma becomes strongly absorbing: most of the pulse energy is directly transferred to the plasma, and a damage occurs in the material. Since the plasma remains localized at the focal volume, the damage involves only such region. By convention, it is assumed that the

optical breakdown starts when the electron density reaches the critical value: $N = N_c$ [55].

Example 2. *If* $\lambda = 1030$ nm*, then* $\omega_L \simeq 10^{15}$ Hz *and the critical density is* $N_c \simeq 10^{21}$ cm^{-3}*. Assuming a pulse duration of* 100 fs*, the threshold laser intensity required to reach the optical breakdown is* $I_{th} = 10$ TWcm^{-2} *[56].*

It has been showed that the avalanche ionization rate depends linearly on the laser intensity [55]. If nonlinear photoionization were the only absorption process, the optical breakdown threshold intensity would vary greatly with band gap. But since also avalanche ionization contributes to the absorption process, such threshold has small variations with band gap [49]. Thanks to this low dependence, FLM can be applied to a broad range of dielectrics materials [46].

It should be noticed that, in borosilicate glass, for pulses with a temporal width shorter than 100 fs, nonlinear photoionization dominates over avalanche ionization [57]. Therefore, under this condition, the former can produce damage in the glass by itself.

Apart from that, shorter pulses allow a higher precision in the fabrication. Indeed, sub-picosecond pulses require less energy per pulse, with respect to picosecond ones, to reach the threshold intensity for optical breakdown.

3.2.2 Energy Relaxation

Once the plasma is fully formed, and the threshold condition has been reached, the energy absorbed by the plasma is transferred to the lattice. However, since the time for the electrons to thermally excite the surrounding lattice is in the picosecond timescale [53], the heat transfer occurs long after the laser pulse is gone. In other words, the lattice heating is temporally separated from the energy absorption.

If the laser repetition rate is high enough, a pulse arrives before the heat diffusion driven by the previous one is concluded. Such cumulative heating increases the volume of the modified region (for a deeper discussion, see §3.3.2).

3.2.3 Material Modification

Following the heat transfer to the lattice and the consequent heat accumulation, a permanent modification in the material structure is generated. Depending on the fabrication parameters (see §3.3) and on the properties of the material (e.g. band gap), different structural changes can be induced.

In fused silica glass, at relatively low pulse energy (~ 100 nJ with 100 fs pulses, 800 nm wavelength), an isotropic modification of the volume around the focal point has been observed [58]. This produces a smooth change in the refractive index of the glass. No heat accumulation effect has been observed.

In borosilicate glass, with repetition rate higher than 100 kHz, heat accumulation effects have been observed (with 400 fs laser pulses, 1040 nm wavelength) [59].

In both glasses, the magnitude of the refractive index contrast is in the order of $\Delta n \sim 10^{-3}$ [60]. This is the regime used for waveguide fabrication. Other structural changes exist, like the birefringent refractive index change or the void formation (both happening at higher pulse energies than the isotropic refractive index change) [61].

3.3 Fabrication Parameters

So far, only two fabrication variables have been discussed, namely pulse energy and pulse duration. However, many other parameters can influence the fabrication. Here follows a review of the main ones.

3.3.1 Writing Configuration

The writing configuration describes the sample translational direction with respect to the laser beam propagation direction – assumed to correspond to the z axis in the following. Usually, for waveguide fabrication, the sample is moved and not the beam.

In the *longitudinal configuration*, the sample is translated along the direction of the beam propagation. The cross section of the fabricated structure is symmetric [62], since its radius – in both directions perpendicular to the z axis – depends on the beam waist diameter (see Eq. B.4).

However, the waveguide length is limited by the lens working distance, which can be a limiting factor in the fabrication of complex structures.

A more flexible configuration is usually adopted, called *transversal configuration*, depicted in Fig. 3.3. The sample is translated orthogonally to the beam propagation direction.

Waveguides can be fabricated exploiting the entire sample depth. Indeed, an usual objective used for fabrication has a working distance of some millimeters, usually bigger than the sample depth. The only limitation in the size is given by the positioning system (see § 4.1).

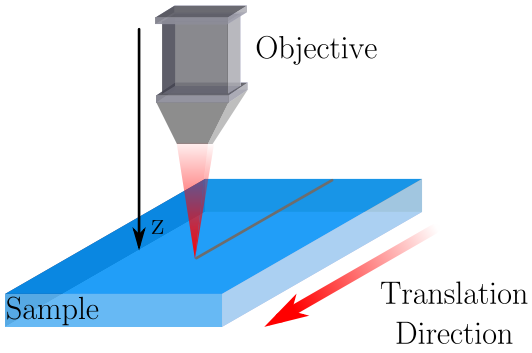

Figure 3.3: Transversal writing geometry. The sample is translated along a direction perpendicular to the laser beam – set to be the z axis.

However, with this configuration, the waveguide cross section is asymmetric. In the direction perpendicular to both the z axis and the writing direction, the waveguide radius depends on the laser beam waist w_0 (Eq. B.4). But along the z axis, the radius depends on the Rayleigh range z_R (Eq. B.5). Their ratio can be expressed as $z_R/w_0 = n/NA$ (see Eq. B.6), usually different from 1.

Example 3. *Usual values for glass fabrication are* $n = 1.5$, $NA = 0.25 \div 0.85$. *Thus* $n/NA = 1.8 \div 6$, *bigger than one. For this reason, the waveguide is fabricated with an elliptical cross section. By using an objective with* $NA \simeq n = 1.5$, *a more symmetric cross section can be obtained. However, this implies to decrease the beam waist by almost an order of magnitude (see Eq. B.4), allowing the fabrication of very poorly-guiding waveguides (recall indeed that* $\Delta n \sim 10^{-3}$ *which – together with a reduced beam waist – prevents light from being well confined into the guiding region) [62].*

In the past years, various techniques have been devised allowing the use of the transversal configuration with a lower degree of ellipticity (see for example [63]). However, in many situations, the cross section ellipticity is not too high, so that high quality waveguides can be still fabricated.

3.3.2 Repetition Rate

The repetition rate of the laser, i.e. the number of pulses per second, can affect the damage induced. When the repetition rate is low, the material modification is limited to the focal volume. Indeed, the thermal energy diffuses out of this region almost completely before the subsequent pulse comes [64]. The pulses act independently from one another.

Moreover, a long time is needed to fabricate a single structure, due to the low writing speed ($\sim \mu m/s$) required for this regime [65].

The waveguide quality can be improved (i.e. the losses decreased) by increasing the repetition rate. Eaton *et al.* [66] have shown that, in borosilicate

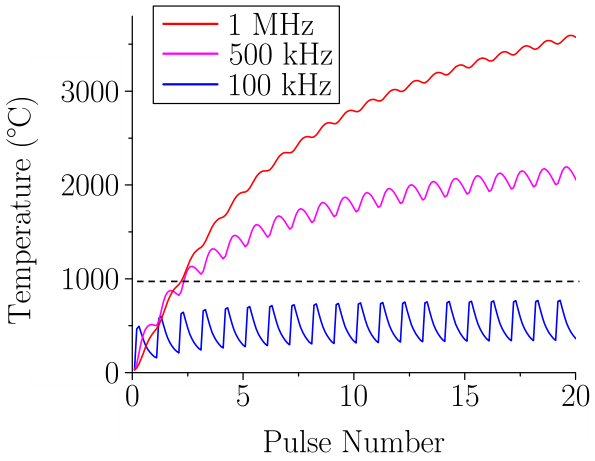

Figure 3.4: Simulated glass temperature – at a radial position of 3 μm from the focus – versus exposure at repetition rates of 100 kHz, 500 kHz, 1 MHz. The dashed line represents the softening point of the glass. Cumulative heating is absent at 100 kHz repetition rate. Adapted from [67].

glass, the minimum repetition rate to induce cumulative heating is 200 kHz. At such rates, the time between consecutive pulses is shorter than the time required for the absorbed laser energy to diffuse out of the focal volume.

As can be seen from Fig. 3.4, a higher temperature can be reached with a repetition rate of 1 MHz, with respect to lower rates. Thus, the melted volume is strongly increased and the size of the modified structure increases. Notice that at 100 kHz, the temperature does not reach the softening point of the glass[4] (dashed line in the picture). No heat accumulation is present and a negligible temperature increase is observed.

When a transversal writing configuration is used, such effects allow the creation of more symmetric guiding regions in borosilicate glass [59]. In turn, this permits the fabrication of waveguides with a higher quality.

Moreover, an higher repetition rate allows for a higher writing speed ($\sim mm/s$), so that the fabrication time can be greatly reduced.

When heat accumulation effects are present, it is almost impossible to predict the shape of the refractive index modification. In order to optimize the waveguide performances, it is necessary to perform a trial-and-error procedure, as will be described in § 6.1.

[4]The softening point of the glass is the temperature at which the glass viscosity is $10^{6.6}$ Pa·s (see § 3.4) and the glass deforms under its own weight [68]. For Corning Eagle XG borosilicate glass, such temperature is 971 °C

3.3.3 Focusing Condition

The laser beam is focused into the sample through a system of lenses. However, aberrations can modify the beam shape at the focus. When building buried structures inside the glass, a strong dependence on the depth is present [69]. This dependence is more prominent for lenses with a higher numerical aperture (NA) [49], since peripheral rays are more affected by aberrations.

It is common use to employ a microscope objective for focusing the beam into the sample. Such objective is able to correct both for chromatic and spherical aberrations. Aberrations can be further reduced employing oil-immersion objectives, which reduce the index mismatch between the glass and the environment.

Apart from aberrations, also dispersion caused by beam propagation inside the glass can degrade the process. In particular, dispersion causes the pulse to broaden, thus decreasing the peak intensity – since the pulse energy keeps constant during propagation. If such power decreases below the minimum threshold, the laser beam is no more able to cause a permanent modification of the glass. However, since the propagation in the glass is limited at most to some millimeters, dispersion can be neglected for pulses longer than 100 fs.

Nonlinear effects like self-focusing also come into play. If the pulse peak power exceeds the critical value for self-focusing[5], the pulse is further focused and collapses into a thin filament. In order to avoid this, the pulse peak power has to be below such critical value, but still higher enough so to achieve the optical breakdown.

3.3.4 Other Parameters

The translational speed is defined as the distance the sample travels in one second. The higher it is, and the lower is the time range in which a given volume is invested by pulses – keeping fixed the repetition rate [70]. Therefore, at high scan speed, the energy pulse threshold increases.

On the other hand, a high translational speed allows a quicker process, since less time is required for the waveguides fabrication.

Also the number of scan, i.e. how many times the laser beam is scanned over the same structure, can affect the quality of the waveguide. In particular, in borosilicate glass, using more than one scan allows to increase the refractive

[5]For a Gaussian beam, the critical peak power for self-focusing is defined as $P_c \simeq \lambda^2/\pi n_0 n_2$ where n_0 and n_2 are, respectively, the linear and non-linear refractive index of the material.

index contrast. In this way, waveguides with a more guiding region can be fabricated.

3.4 Annealing

The temperature at the focal volume can reach 10 000 °C, in the instant just after the pulse arrives [70]. However, the focal spot moves during fabrication: after a given number of pulses have been absorbed, the modified region rapidly cools down.

This may induce mechanical stresses inside the glass, that can be reduced by an annealing procedure. The term *annealing* refers to some kind of thermal treatments able to remove – or at least reduce – internal mechanical stresses in the material.

To understand which is the thermal treatment useful for the present work, two notable temperatures of glasses have to be defined. Usually, they are characterized by the viscosity[6] the material reaches at that temperature.

At a viscosity of 10^{12} Pa·s, the glass is at the *annealing point*. The glass, being still solid, is able to relax internal stresses in some minutes – if the temperature is kept fixed just above this point.

At a lower temperature, and at a viscosity of $10^{13.5}$ Pa·s, the glass reaches the *strain point*. Here, stresses relax in some hours. Below such point, any internal relaxation stops and it is safe to cool down the sample at the desired rate, in order to reach room temperature [68].

A typical annealing process, represented in Fig. 3.5, consists of the following steps:

a) Rapid heating just above the annealing point.

b) Gradual temperature decrease down to the strain point – which prevents the formation of additional stresses.

c) Rapid cooling down to room temperature.

The annealing process can be efficiently applied to increase the quality of the waveguides fabricated using the FLM technique [71]. The first step consists in fabricating waveguides with a higher pulse energy to what is usually done to produce single-mode waveguides. In this way, a multi-mode waveguide is generated.

[6] For a solid, the viscosity is defined as the force arising in response to shear, compression or tension stresses. It is measured in $Pa \cdot s$.

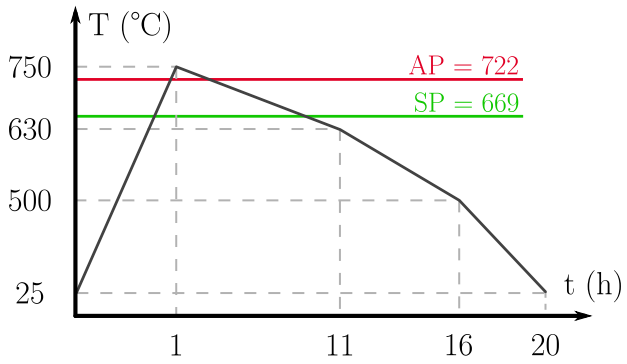

Figure 3.5: Dependence of annealing temperature with time. The red line marks the annealing point (AP), the green line the strain point (SP). The values are related to Corning Eagle XG borosilicate glass. Picture not in scale.

The refractive index profile thus induced is composed of a central region with $\Delta n > 0$, then by a depressed ($\Delta n < 0$) ring and finally by an outer ring with $\Delta n > 0$, but in magnitude lower than the first one.

Though an exact measure of the refractive index contrast should be performed with more advanced techniques (such as phase-contrast imaging or refractometry), it is possible to have a qualitative insight of its profile by a simple microscope analysis. As an example, Fig. 3.6a shows the cross section of a femtosecond laser written waveguide. It is possible to distinguish white regions which indicate an increase in the refractive index, i.e. a region guiding the light coming from the microscope.

This refractive index profile is acceptable for straight waveguides, but exhibits high losses for bent waveguides (see § 4.3.3), especially if the curvature radius is small [72].

The annealing process is therefore carried out. This allows to completely eliminate the outer $\Delta n > 0$ ring and to increase the magnitude of the depressed ring. The refractive index profile is more gaussian shape-like – ideal for guiding a single-mode – as in Fig. 3.6b. However, the magnitude of the central refractive index contrast decreases slightly.

The gaussian shape of the waveguide core allows to reduce significantly the bending loss (see § 4.3.3) with respect to the non-annealed waveguide. Indeed, the gaussian mode profile has similar performances to the step-index one, well known to guide efficiently around bends [71].

The annealing process is also able to reduce the birefringence of the written waveguides [73]. A polarization-insensitive device can thus be fabricated, i.e.

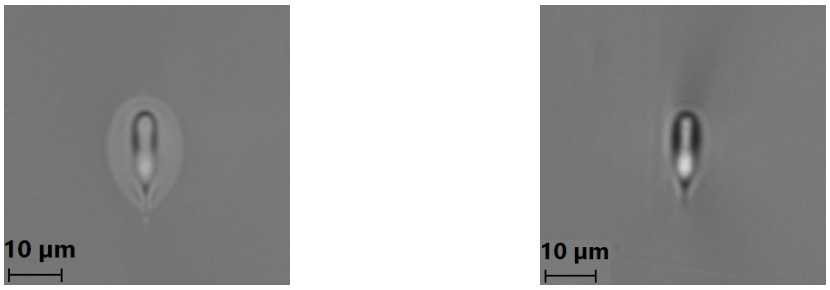

(a) **(b)**

Figure 3.6: Examples of waveguides **(a)** before and **(b)** after the annealing process. In the left image the outer $\Delta n > 0$ ring is clearly visible surrounding the waveguide core; in the right one, such ring has disappeared.

a device operating with the same behavior independently of the injected light polarization.

Chapter 4

Experimental Setup and Methods

In this chapter the experimental setup will be presented. Firstly, the fabrication line and procedure will be reviewed followed by a brief explanation of the microscope analysis. Then the characterization process will be deeply analyzed, focusing on the waveguide losses and on the methods employed to study them. Finally, the setup and the procedure used to retrieve the $V2PM$ from a given DBC will be described.

4.1 Fabrication Setup

In this work, the laser source employed has a wavelength of 1030 nm. Each pulse has a maximum energy of 1 μJ and a time width of 350 fs.

In particular, the source is a cavity-dumped mode-locked oscillator with internal repetition rate of 17 MHz. The active medium is a $KY(WO_4)_2$ crystal, doped with Ytterbium. The medium is optically pumped by an InGaAs multi-emitter laser diode (wavelength of 980 nm and power of 15 W). A laser pulse is extracted from the cavity when a Pockels cell – controlled by an external electronic driver – induces a polarization rotation, causing the reflection of part of the pulse by a thin-film polarizer. The available repetition rate spans from few kHz up to 1.1 MHz (for this work, 1 MHz has been used).

Just after the source, a half-wave plate combined with a Glan-Thompson polarizer allows to tune the power to the desired value. The polarizer also sets the polarization used during the fabrication.

The sample is mounted onto a three axes air-bearing translational stage Aerotech FiberGlide 3D. Three independent axes, driven by a linear brushless

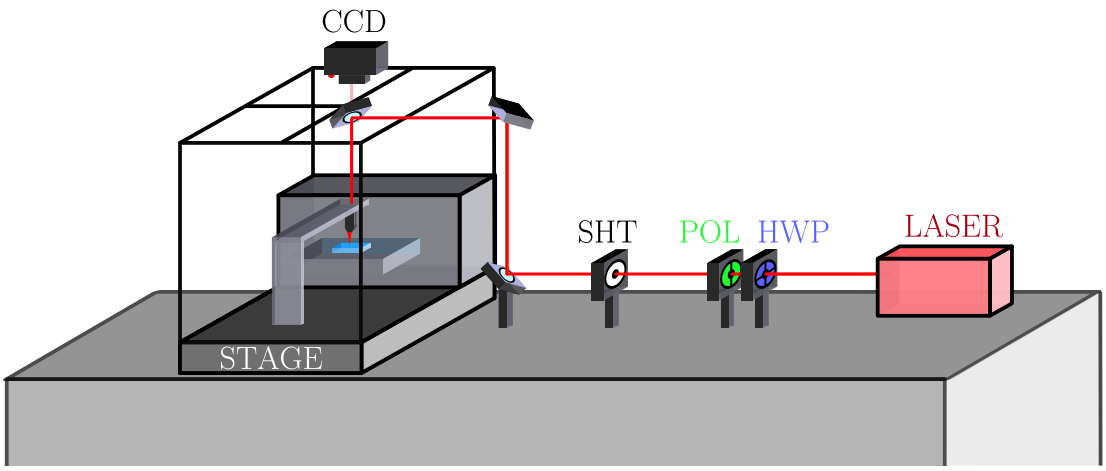

Figure 4.1: Schematic representation of the fabrication setup. HWP = Half-Wave Plate, POL = Polarizer, SHT = Shutter, CCD = CCD Camera.

servomotor, allow to span smoothly the whole sample[7]. The latter can be also rotated around two axes perpendicular to the beam thanks to a gimbal-based adjuster Thorlabs GM100. The stage axes are controlled via software. The instructions are encoded in G-code language.

To obtain high-quality waveguides in borosilicate glass, a microscope objective (50X magnification and $NA = 0.6$) has been used to focus the laser beam into the sample. The focal point is kept fixed, only the sample moves.

A near-infrared CCD camera – mounted perpendicularly to the sample – receives the back-reflection coming from the air-glass interface. It is used to precisely align the sample to the laser beam and to determine the origin of the stage coordinate system.

Finally, a mechanical shutter Thorlabs SH05 is synchronized with the stages and controlled through the same software. It is used to turn off the fabrication process when the focus passes through a region where no waveguide should be fabricated.

A schematic representation of the fabrication setup is depicted in Fig. 4.1. Notice that the beam has been represented in red for clarity, even if it is not in the visible spectrum.

4.2 Microscope Analysis

After the fabrication phase, the sample is analyzed at the optical microscope. It is a quick method, used to qualitatively study the fabricated geometry. A Nikon

[7]Position accuracy 100 nm, maximum volume covered 100x150x5 cm^3, maximum translational speed 100 mm/s.

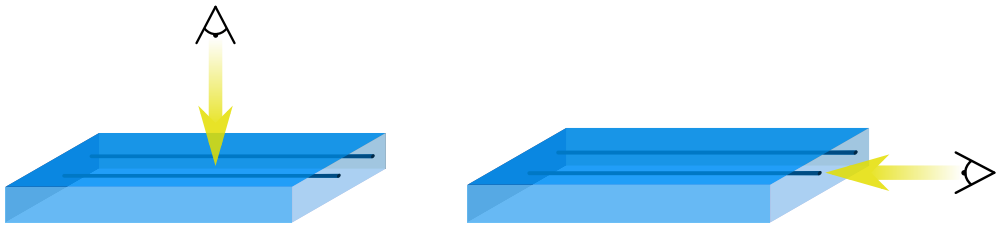

(a) View from the above face. **(b)** View from the side face.

Figure 4.2: Graphical representation of the microscope analysis. The yellow arrow represents the observation direction.

ECLIPSE ME600 microscope has been used, together with a PixeLINK PL-B871 CCD camera for images acquisition. The microscope objectives are Nikon Plan Fluor 4X, 10X, 20X and 40X.

The first step consists in observing the waveguide from the top, i.e. perpendicular to the writing direction, as in Fig. 4.2a. In this way, eventual interruptions of the waveguide path can be detected. Interruptions can be caused by the presence of some unwanted particle – like dust – on the surface of the sample, which distorts the beam focus during the fabrication. They strongly impact the loss of the waveguide, reducing the amount of guided light.

After that, both input and output facets are observed with the microscope light parallel to the writing direction, as in Fig. 4.2b. The faces should be polished, otherwise the excessive scattering does not allow to spot the waveguide core. This view is useful to qualitatively identify if the waveguide has been fabricated correctly, i.e. if it is able to guide light. This can be checked by observing the shape of the modified region. High quality waveguides present a bright central core. This is the guiding region, which is guiding the microscope light, as can be seen from Fig. 3.6b.

However, in order to study quantitatively the waveguide property, a more accurate method is needed. This phase will be presented in the following section.

4.3 Characterization Setup

It is very difficult to predict the behavior of FLM waveguides, due to the complexity of the mechanisms involved. For this reason, it is not possible to accurately model their properties. In order to find the best waveguide, many combinations of fabrication parameters (see § 3.3) have to be explored. The best waveguide is the one minimizing the amount of losses, and with the desired mode profile and polarization behavior.

The characterization phase is therefore of paramount importance, since it allows to determine the optimum and most reproducible among the different fabrication conditions.

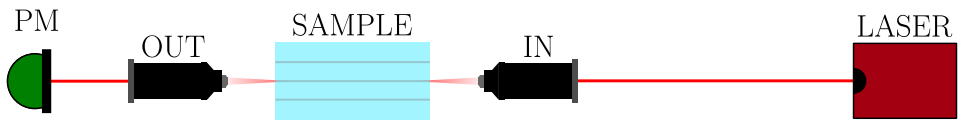

(a) End-fire coupling configuration.

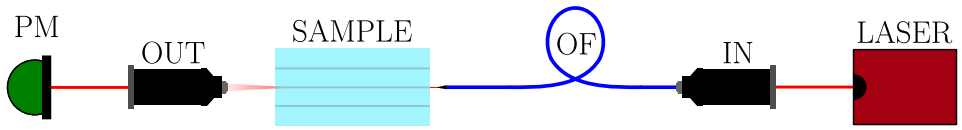

(b) Fiber-butt coupling configuration.

Figure 4.3: Schematic representation of the characterization setups. IN = Input objective, OUT = Output objective, PM = Power Meter, OF = Optical Fiber.

To characterize a waveguide, a laser beam with known properties (e.g. power, mode profile and polarization) is injected into it. The output beam is then collected and analyzed. Knowing the input, and measuring the output, the waveguide properties can be inferred.

Two are the configurations used to characterize a waveguide. The first one is called *end-fire* configuration, depicted in Fig. 4.3a. A microscope objective is used to collimate the laser beam into the sample input facet. After propagation inside the waveguide, the output light is collected by another objective, focusing the image onto a power meter sensor.

This setup is used whenever the polarization behavior of a waveguide has to be analyzed. Indeed, the objectives preserve the incoming light polarization, which can be fixed employing additional optical elements. For example, a polarizer and a half-wave plate can be placed after the laser source to tune the angle of the input light polarization, or a quarter-wave plate can be used to inject circularly-polarized light inside the waveguide. In this work, a Thorlabs Linear Polarizer and a B. Halle Zero Order half-wave plate, both optimized for the 1550 nm wavelength, have been used.

The second configuration is called *fiber-butt* coupling, represented in Fig. 4.3b. The input objective is used to focus the laser beam inside a single-mode optical fiber. The light coming out from the fiber is directly coupled into the waveguide by bringing them close. After propagation in the sample, the output light is collected by another objective. This setup is used to precisely measure the waveguide losses. However, the optical fiber does not preserve the incoming light polarization.

For this work, a Thorlabs diode laser at 1550 nm, a power meter Ophir Nova II and an optical fiber able to guide the above wavelength have been used. A Santec ECL-200 tunable laser (from 1480 nm to 1600 nm) has been employed when the wavelength behavior of a structure has to be addressed.

To allow a precise movement, the fiber has been mounted on a Melles Griot NanoMAX micropositioner. The sample is set on a Thorlabs MBT402D stage, allowing the movement along two axes perpendicular to the laser beam. Two additional degrees of freedom are the rotations around those axes.

In the remainder of this section, the methods employed to study the waveguide losses and mode profile will be analyzed.

4.3.1 Waveguide Mode Profile

The analysis of the output mode profile is useful to determine the waveguide behavior for a certain input wavelength. It is used not only to study the waveguide loss (see § 4.3.2), but also to estimate the coupling coefficient with neighboring waveguides.

The intensity profile of the supported mode can be measured employing a configuration similar to Fig. 4.3b, but substituting the power meter sensor with a camera. After that, the sample has to be removed in order to acquire the optical fiber intensity profile. In this way, by comparing the acquired profiles, it is possible to calibrate the waveguide mode with respect to the optical fiber one (which has known dimensions). In this work, an InGaAs camera Xenics Bobcat 640 has been used.

All the used optical fibers support a single mode – the fundamental one. For a waveguide, single mode operation is preferred in order to have a reproducible coupling between neighboring waveguides and low bending losses. Employing the camera is therefore an efficient method to verify that the chosen waveguide can sustain only the fundamental mode and not higher order ones.

Since this configuration ensures the absence of sign-inversion in the profile, the mode electric field can be estimated from the square root of the intensity profile $E(x, y) \propto \sqrt{I(x, y)}$.

4.3.2 Waveguide Losses

In the following, all the types of waveguide loss will be defined, showing how to retrieve them from a typical characterization experiment.

The most general type of waveguide loss is the *Insertion Loss* (IL), defined as

$$IL\big[\mathrm{dB}\big] = -10 \log_{10}\left(\frac{P_{out}}{P_{in}}\right) \tag{4.1}$$

P_{out} is the power measured at the end of the output objective, following the fiber-butt configuration (see Fig. 4.3b). P_{in} is the power measured with the same setup, but removing the sample and eventually bringing the output objective closer to the fiber, so to focus its output on the power meter sensor [65].

Notice that the loss introduced by the objectives and the fiber, even if low, are included in such measured powers. However, since they are present in both P_{out} and P_{in}, when doing the ratio they disappear so that they are not present in IL.

The insertion loss is composed by many terms:

$$IL\big[\mathrm{dB}\big] = FL\big[\mathrm{dB}\big] + CL\big[\mathrm{dB}\big] + L\big[\mathrm{cm}\big] \cdot PL\left[\frac{\mathrm{dB}}{\mathrm{cm}}\right] \tag{4.2}$$

Each term is now described, showing how it can be computed.

Fresnel Loss

At the interface between two media with different refractive index, a portion of the light is reflected. The remaining part is transmitted. It is possible to define the *reflectance* R as the portion of the light power that is reflected: $P_r = RP_{in}$. When dealing with normal incidence, R can be computed through the Fresnel equation

$$R = \left(\frac{n_1 - n_2}{n_1 + n_2}\right)^2 \tag{4.3}$$

where n_1 and n_2 are the refractive indices of the two media. Similarly, the *transmittance* is defined as $P_t = TP_{in}$. It is the complementary variable to R since $T = 1 - R$.

The *Fresnel Loss* (FL) is defined as the portion of the power lost due to the propagation through the air-glass interface. It can be defined similarly to Eq. 4.1 as

$$FL\big[\mathrm{dB}\big] = -10\,\log_{10}\left(\frac{P_t}{P_{in}}\right) = -10\,\log_{10}\left(T\right) \tag{4.4}$$

Notice that P_t is not measurable, since it is the power just after the interface, i.e. inside the glass. However, thanks to Eq. 4.3, T is known. The Fresnel loss has a fixed and known value for a given interface.

Example 4. *Consider the air ($n_1 = 1$) glass (if borosilicate glass $n_2 \simeq 1.5$, at $\lambda = 1550$ nm) interface. Then $R \simeq 4\%$, $T \simeq 96\%$. Employing Eq. 4.4 it is possible to obtain $FL = 0.177$ dB.*

The Fresnel loss can be reduced employing index-matching materials. The refractive index difference is thus decreased, increasing the transmittance.

Coupling Loss

The *Coupling Loss* (CL) is defined as the power lost when the light is coupled from the fiber to the waveguide [62]. It is due to a mismatch between the fiber and the waveguide mode profiles. It can be estimated with the following superposition integral [74]:

$$CL\big[\mathrm{dB}\big] = -10\,\log_{10}\left(\frac{\left|\iint E_{wg}E_{of}^{*}\mathrm{d}x\mathrm{d}y\right|^2}{\iint \left|E_{wg}\right|^2\mathrm{d}x\mathrm{d}y \iint \left|E_{of}\right|^2\mathrm{d}x\mathrm{d}y}\right) \tag{4.5}$$

where E_{wg}, E_{of} are, respectively, the waveguide and fiber electric field. Usually, a more simplified version of Eq. 4.5 is used, valid when coupling a single-mode fiber to a single-mode waveguide [62]:

$$CL[\mathrm{dB}] \simeq -10 \log_{10}\left(\frac{(a^2+x^2)(a^2+y^2)}{4a^2xy}\right) \tag{4.6}$$

where a is the optical fiber mode radius and x, y the waveguide mode radii.

While a is known from the fiber specifications, x and y have to be measured. This can be done following what has been presented in § 4.3.1.

Propagation Loss

The *Propagation Loss* (PL) is the loss strictly related to the propagation of light inside the waveguide. The internal geometry of the refractive index modification is not perfectly smooth and uniform. This produces scattering causing some photons to be lost.

Another contribution to the propagation loss is the presence of absorption centers inside the waveguide. Absorbing some photons, they contribute to the photon loss – even if, in glass, this mechanism is of minor importance [75].

The propagation loss is defined as the portion of power lost after the light propagated through the sample

$$PL\left[\frac{\mathrm{dB}}{\mathrm{cm}}\right] = -\frac{1}{L}\,10\,\log_{10}\left(\frac{P(L)}{P_{in}}\right) \tag{4.7}$$

where $P(L)$ is the measured power at the end of a waveguide of length L.

Being dependent on the waveguide length L, the propagation loss is defined in dB/cm – rather than in dB as the other types of losses. In this way, the measured loss is normalized with respect to L. It is thus possible to compare the propagation loss in different waveguides.

Notice that it is not convenient to measure $P(L)$ because waveguides with different length require different samples. This problem could be in principle solved fabricating waveguides with the same length on a single sample and then cutting it to shorter lengths for any waveguide. However, this is a long and sample-destructive process.

Since all other quantities can be easily computed, the propagation loss can be directly retrieved from Eq. 4.2 as

$$PL\left[\frac{\mathrm{dB}}{\mathrm{cm}}\right] = \frac{IL - FL - CL}{L} \tag{4.8}$$

This final value is characteristic for each waveguide and it is used to express quantitatively its guiding properties. Indeed, being a typical FLM device long at least a couple of centimeters, the main loss mechanism is the propagation while

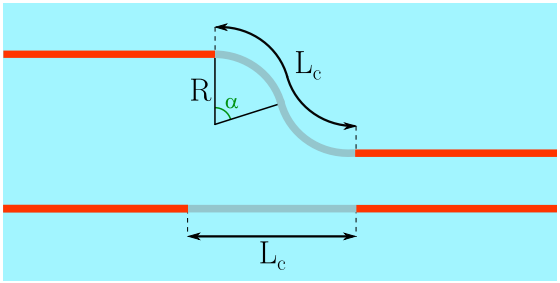

Figure 4.4: Comparison between a straight waveguide (bottom) and a bent waveguide (top) with curvature radius R. The length L_c is equal in both structures The picture is not in scale.

the coupling and Fresnel losses are almost constant. This is the reason why the propagation loss – rather than the insertion loss – is used to assess the waveguide quality.

4.3.3 Bending Waveguides

Once the optimum fabrication conditions have been found, it is useful to study to which extent such waveguides can be bent. An additional type of loss is now present, namely the *Bending Loss* (BL). During propagation inside a bent waveguide, photons can be lost in the surrounding media due to the finite curvature radius [75].

The bending loss depends exponentially on the curvature radius R_c:

$$BL \propto e^{-R_c} \tag{4.9}$$

Due to this strong dependence, the minimum achievable curvature radius is in practice limited by the bending loss, rather than by fabrication tolerances – which would allow for curvature radius as low as some micrometers.

To compute the bending loss, the output power of a bent waveguide has to be compared with a reference value. Such reference is, in this context, the output power of the corresponding straight waveguide (i.e. the one fabricated with all the same parameters), called $P_{out,straight}$:

$$BL\left[\frac{\mathrm{dB}}{\mathrm{cm}}\right] = -\frac{1}{L_c}\,10\,\log_{10}\left(\frac{P_{out}}{P_{out,straight}}\right) \tag{4.10}$$

where L_c is the length of the curved path, as depicted in Fig. 4.4.

Eq. 4.10 has been obtained assuming the length of the straight regions outside L_c in both waveguides to be equal (red paths in Fig. 4.4). In this approximation, the propagation losses introduced by those regions are almost equal – as are the

coupling and Fresnel losses. Therefore, the bending loss can be evaluated by a direct comparison of the insertion losses of the two structures:

$$BL\left[\frac{\mathrm{dB}}{\mathrm{cm}}\right] = \frac{IL - IL_{straight}}{L_c} \tag{4.11}$$

Notice that from Eq. 4.11, Eq. 4.10 can be immediately obtained.

Example 5. *Consider a sample with length* $L = 25$ mm. *A bent waveguide with* $L_c = 20$ mm *and a curvature radius of* $R = 40$ mm *has to be fabricated inside the sample. The angle of the circular paths is* $\alpha = L_c\,/\,(2R) = 14.3°$. *Thus the length of half a circle is* $x = R\sin\alpha = 9.88$ mm *which differs from* $L_c\,/\,2 = 10$ mm *just by* 0.12 mm. *This difference introduces a propagation loss that can be neglected – if compared with the* 10 mm *of the original path.*

4.4 V2PM Retrieval

It has been shown in § 2.3 that in order to retrieve the complex visibility of an astronomical target, an array of evanescently-coupled waveguides can be used, i.e. a DBC. Such device is described by the $V2PM$, which can be experimentally retrieved injecting known sources into the device and observing the output distribution.

To access different baselines, a two-fields injection is used. Moreover, a phase delay between them is required in order to observe the interference fringes. This can be realized with a Michelson interferometer. A beam is divided with a beam splitter; the two new beams travel the same path and they recombine through the same beam splitter. In order to introduce a phase difference between the two, one of the mirror is mounted on a translational stage. By moving it, the delay τ between the fields is modified and a phase difference is introduced.

In order to arbitrarily access two different points on the DBC input, an improvement to the Michelson interferometer is required. The movable mirror can also be titled around the axis perpendicular both to the plane and to the beam propagation direction [76]. A lens can then be used to focus both beams into the two required inputs. The complete setup is shown in Fig. 4.5.

With this setup, it is possible to experimentally obtain the $V2PM$. For the sake of simplicity, a 16-waveguides square DBC with three input fields is here considered ($N = 16$, $M = 3$). The optimal input field configuration is represented in Fig. 2.14c. In the following, those three input positions will be identified with 1, 2 and 3.

For the present condition, Eq. 2.25 is as follows

$$\begin{pmatrix} J_1 \\ J_2 \\ \vdots \\ J_{16} \end{pmatrix} = \begin{pmatrix} b_{1,1} & b_{1,2} & \dots & b_{1,9} \\ b_{2,1} & b_{2,2} & \dots & b_{2,9} \\ \vdots & \vdots & \ddots & \vdots \\ b_{16,1} & b_{16,2} & \dots & b_{16,9} \end{pmatrix} \begin{pmatrix} G_1 \\ G_2 \\ \vdots \\ G_9 \end{pmatrix} \tag{4.12}$$

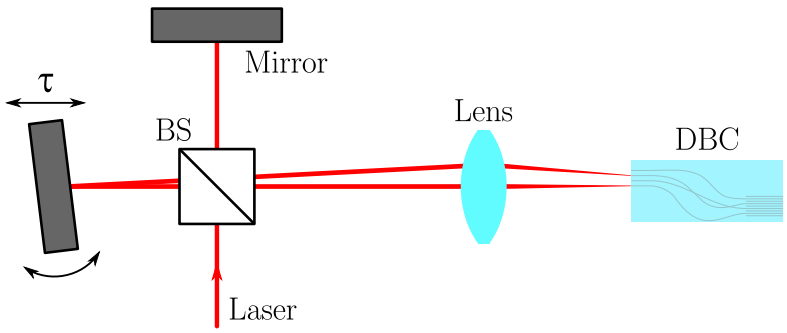

Figure 4.5: Modified Michelson Interferometer. One of the mirror is able to move along the beam direction so to increase the delay τ. It can be also titled in order to match the DBC inputs. BS = Beam Splitter.

The aim is to retrieve all the 16x9 $b_{n,m}$ coefficients. The analysis is divided in two steps [77]. The first one consists in obtaining the first three columns of the $V2PM$. When light is injected only at the input 1 of the DBC, the G vector is as follows

$$G = \begin{pmatrix} G_1 & 0 & 0 & \dots & 0 \end{pmatrix}^T \tag{4.13}$$

Inserting this value into Eq. 4.12, it is possible to obtain

$$J_n = b_{n,1} G_1, \qquad i = 1, 2, ..., 16 \tag{4.14}$$

so that by measuring J_n and knowing G_1, all the $b_{n,1}$ coefficients can be retrieved. Repeating the process for the inputs 2 and 3 the – respectively – second and third column of the $V2PM$ can be obtained as well.

The second step is quite different, since two fields are required. Indeed, defining a G vector with $G_4 \neq 0$ and $G_1 = G_2 = 0$ has no physical meaning (it would represent two fields with a non-null MCF but with zero intensity).

The two input fields have a phase modulation ϕ between them. Consider for the moment only the inputs 1 and 2; the G vector has now the form

$$G = \begin{pmatrix} \Gamma_{1,1} & \Gamma_{2,2} & 0 & \mathbb{R}\mathrm{e}[\Gamma_{1,2}] & 0 & 0 & \mathbb{I}\mathrm{m}[\Gamma_{1,2}] & 0 & 0 \end{pmatrix}^T \tag{4.15}$$

Thus, employing Eq. 4.12, the output intensity at the n-th waveguide can be written as

$$\begin{aligned} J_n &= b_{n,1}|A_1|^2 + b_{n,2}|A_2|^2 + b_{n,4}\,\mathbb{R}\mathrm{e}[\Gamma_{1,2}] + b_{n,7}\,\mathbb{I}\mathrm{m}[\Gamma_{1,2}] = \\ &= b_{n,1}|A_1|^2 + b_{n,2}|A_2|^2 + b_{n,4} V_{1,2}|A_1||A_2|\cos\phi + b_{n,7} V_{1,2}|A_1||A_2|\sin\phi \end{aligned} \tag{4.16}$$

In the second equivalence the modulus of the visibility function has been introduced (Eq. 2.28), together with $\Gamma_{1,1} = |A_1|^2$ and $\Gamma_{2,2} = |A_2|^2$ where A_1, A_2 are the electric fields amplitudes at the input 1 and 2, respectively.

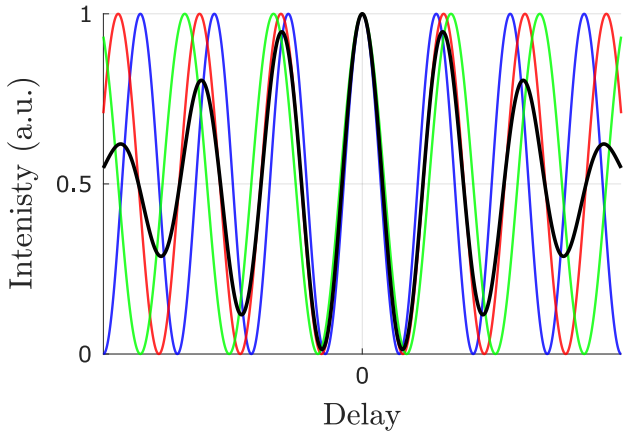

Figure 4.6: Three monochromatic fringe patterns are shown in blue, red and green for three different wavelengths, as a function of the delay. Their (normalized) sum is the polychromatic intensity pattern (black curve). Adapted from [25].

Notice also that since $\Gamma_{1,2}$ is a complex function, the following relations hold

$$\sqrt{(\mathbb{R}\mathrm{e}[\Gamma_{1,2}])^2 + (\mathbb{I}\mathrm{m}[\Gamma_{1,2}])^2} = \frac{\mathbb{R}\mathrm{e}[\Gamma_{1,2}]}{\cos\phi} = \frac{\mathbb{I}\mathrm{m}[\Gamma_{1,2}]}{\sin\phi} \tag{4.17}$$

where ϕ is the phase difference between the fields.

The first two terms in Eq. 4.16 are DC components which can be isolated from the rest. The remaining terms describe an oscillatory function of the type

$$\tilde{J}_n = \alpha\cos\phi + \beta\sin\phi \tag{4.18}$$

Three examples of $\tilde{J}_n$ are shown in Fig. 4.6 (blue, red and green curves) for three different wavelengths. By fitting the output intensity at the n-th port with the $\tilde{J}_n$ signal, the coefficients α and β can be obtained. From here, it is straightforward to extrapolate $b_{n,4}$ and $b_{n,7}$, since the two input fields are known (hence also the $V_{1,2}$):

$$\begin{aligned} b_{n,4} &= \frac{\alpha}{V_{1,2}|A_1||A_2|} \\ b_{n,7} &= \frac{\beta}{V_{1,2}|A_1||A_2|} \end{aligned} \tag{4.19}$$

The visibility function modulus $V_{i,j}$ represents the fringes contrast, i.e. the difference between the maxima and minima of the interference pattern. Therefore, as can be seen from Fig. 4.6: $V_{i,j} = 1$.

The whole process can be repeated for the input pairs 1-3 and 2-3 and for all the N output waveguides. Thus, the complete $V2PM$ can be experimentally retrieved.

The same experimental scheme can be carried out for any DBC configuration, whatever are N and M. The first M columns of the $V2PM$ are found by through the photometry; the other $M^2 - M$ employing the modified Michelson interferometer.

The above procedure is strictly valid only for monochromatic input field. For each wavelength, G and $V2PM$ can be computed: they will in general depend on the wavelength chosen. The polychromatic output intensity can be obtained summing up all the monochromatic intensities, since different wavelength do not interfere

$$J = \int_{\lambda_{min}}^{\lambda_{max}} \underline{\underline{V2PM}}(\lambda) G(\lambda) \mathrm{d}\lambda \tag{4.20}$$

In Fig. 4.6 (black curve) is shown the polychromatic fringe pattern, given by the normalized sum of the three monochromatic signals. Notice that when the delay between the arms is increased (in absolute value), the interference is lost and the signal approximates a constant value. The delay τ corresponding to the loss of the fringes contrast is called *coherence time*. It is proportional to the considered spectral bandwidth $\tau_c \propto \Delta\nu^{-1}$ [25].

Chapter 5

DBC Design

The aim of this work is to produce a particular DBC geometry with FLM-written waveguides (see Ch.3). This technique has been chosen since – after proper annealing – ensures a polarization-insensitive behavior of the device. This is required since celestial light is unpolarized, i.e. it has not a fixed polarization direction. The device should work in the same way, independently on the incoming light polarization. Moreover, a $3D$ writing geometry is necessary in order to fabricate a DBC device.

The project is in collaboration with the Leibniz Institute for Astrophysics Potsdam, which provided the simulations of the device operation and performed its interferometric characterization.

This chapter is devoted to the theoretical analysis of the device to fabricate. The initial configuration is presented, followed by improvements to correct some problematic issues. In the end, the pupil remapper is deeply analyzed.

5.1 8-Waveguides DBC

The desired device for this project is a eight-inputs DBC with a zigzag configuration. However, a single DBC with eight input fields would require to simulate an array with more than $8^2 = 64$ waveguides in order to find the inputs configuration and device length able to minimize the condition number. Such a device would be quite complex to design and challenging to fabricate with a sufficient reliability. For this reason, it has been decided to simplify its geometry, with the aim of fabricating a more complex device in the future.

In particular, it has been decided to implement two separate four-inputs DBCs, sampling 8 different points of the same telescope aperture. Following Eq. 2.17, with four telescopes (or four sampled points of one telescope, as in this case), 6 baselines can be obtained. Since the two DBCs sample different points, the total number of baselines is here 12.

It is an improvement to the simpler device with only four inputs, but still a

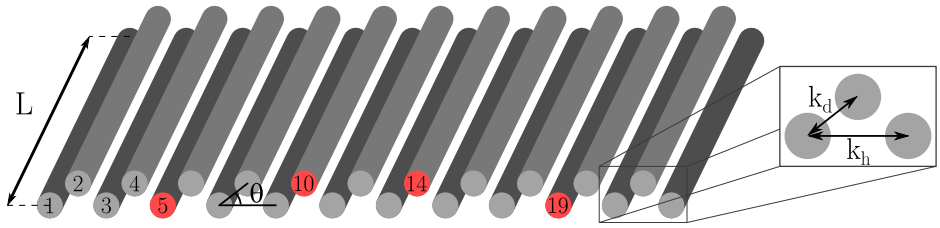

Figure 5.1: 23-waveguides zigzag DBC. The inputs are colored in red and are indicated with 5, 10, 14, 19. The numbering of the waveguides starts from the left-most one on the lower plane. L is the length of the waveguides and θ the angle between the planes. The inset shows the coupling coefficients κ_h and κ_d.

simplified choice with respect to an eight-inputs device. Indeed, with eight points, the baselines are 28. The higher is the number of the telescope pupil sampled points and the more accurate is the Fourier space reconstruction (see § 2.2).

For a single DBC, it has been showed that the configuration allowing the lowest condition number is represented by an array of 23 waveguides, 12 in the lower plane and 11 in the upper one [22]. The input sites are chosen to be at positions 5, 10, 14 and 19, starting the enumeration from the lower plane. The structure is represented in Fig. 5.1.

The two DBCs have the same configuration (both of waveguides and of the input fields). They are placed at the same depth and on opposite sides with respect to the telescope pupil. The latter is connected to the DBCs inputs by a pupil remapper, a device which will be explained in § 5.1.1.

As was explained in § 2.3.2, the waveguides can couple through two coupling coefficients: the horizontal κ_h and the diagonal κ_d one (see the inset in Fig. 5.1). For this work, the requirement to obtain a well-conditioned $V2PM$ is that the two coupling coefficients between waveguides should be equal: $\kappa_h = \kappa_d$. In this case, the condition number obtained is the lowest for the given configuration. In the following chapter, the DBCs parameters will be optimized in order to achieve this condition.

The aim of the project it to test the device at the William Herschel Telescope in the Roque de los Muchachos Observatory (Spain). The telescope has a single mirror with a diameter of 4.2 m. The atmospheric turbulence correction is performed by a segmented deformable mirror on which the primary mirror light is focused. The segmented mirror is composed by 37 hexagons – placed in a honeycomb lattice – that can be independently adjusted.

Eight segments of the deformable mirror will be used to adjust the coupling of the device inputs. In particular, light coming from the chosen segments will be focused into the waveguides by an array of micro-lenses with the same honeycomb lattice and a pitch of 250 μm. For this reason, the input waveguides should strictly match the geometry of the micro-lens array, as depicted in Fig. 5.2.

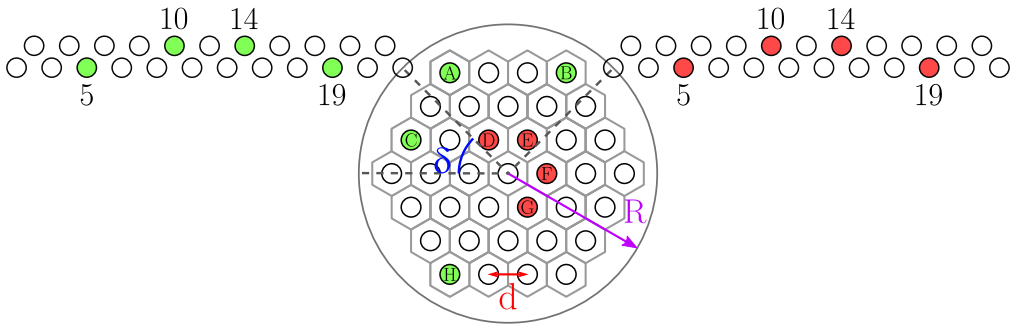

Figure 5.2: Specifications for the eight-waveguides DBC. Each circle represents a waveguide input. The pupil remapper will connect the red points from the pupil to the rightmost DBC and the green ones to the leftmost DBC. R = 900 µm, $\delta = 45°$, d = 250 µm.

The DBCs must be placed at a distance $R = 900$ µm from the pupil center and at an angle of $\delta = 45°$. Each DBC input must be connected to a precise telescope pupil point, according to the following relations:

DBC(g)	**Pupil**
5	H
10	C
14	A
19	B

DBC(r)	**Pupil**
5	G
10	D
14	E
19	F

Table 5.1: Specifications for the DBC waveguide–telescope pupil segment connections. (g) indicates the green DBC and (r) the red one, following the notation of Fig. 5.2.

There are now some design issues that must be addressed. First of all, the height of the device (i.e. the distance from the lower to the upper waveguide) turns out to be slightly more than 1.3 mm. This is a problem since the device will be fabricated inside a 1.1 mm deep glass substrate.

This issue can be solved simply by turning the geometry of the inputs by 60°. The DBCs are instead kept fixed. This transformation, shown in Fig. 5.3, allows to achieve a device height of 0.866 mm, enough to be fabricated inside the glass sample. Notice that in the new configuration no redundant baselines are present. This is because a rotation does not change the relative distance between points. Moreover, the $V2PM$ is not modified since the uniquely connection between the pupil points and the DBC input remains unchanged.

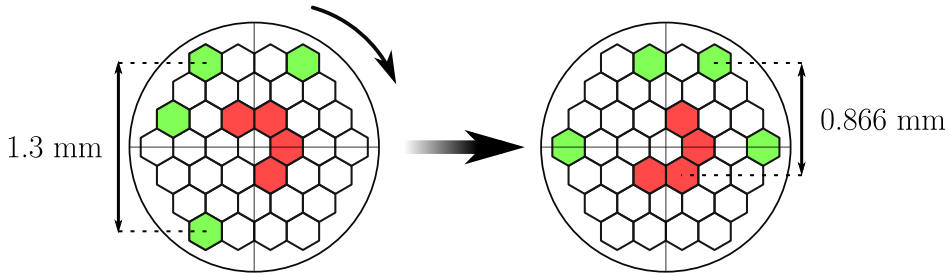

Figure 5.3: 60° rotation of the telescope pupil in order to shorten the device height. The height is modified from 1.3 mm down to 0.866 mm.

Another improvement is to place the DBCs one above the other, on the same side. In this way, the output light can be collected with a single-step acquisition. It is necessary to keep a minimal distance between the two, in order to avoid external coupling: each DBC should work independently from the other.

However, in order to avoid an increase in the device height, it has been necessary to decrease the δ angle down to 30°. Also this time, the $V2PM$ is not modified.

5.1.1 Pupil Remapper

Once the DBC has been configured, it is necessary to route the waveguides coming from the telescope pupil to the DBC input. Indeed, the micro-lenses and the DBC input positions are organized in two different $2D$ surfaces.

The device operating this function is called *pupil remapper*, whose purpose is to remap the mirror points onto the proper DBC waveguides. A pupil remapper is constituted by as many waveguides as the number of the DBC inputs. A pictorial representation of the remapper connecting the pupil to the DBCs is shown in Fig. 5.4.

These waveguides must satisfy certain criteria. A fundamental requirement for a beam combiner device is that the paths that light goes through in the interferometer are equal in length, within the coherence length of the incoming light [23]. This is the distance over which a coherent wave keeps its degree of coherence, i.e. the maximum distance between two optical paths still allowing an interferometric phenomena. The coherence length is defined as $l_c = \lambda_0^2/(n\Delta\lambda)$ where λ_0 is the mean wavelength of the spectrum.

Example 6. *Consider the H atmospheric transmission band:* $\lambda_0 = 1.65$ µm, $\Delta\lambda = 0.35$ µm. *Then* $l_c = 8$ µm, *assuming* $n \simeq 1$. *The requirement can be easily fulfilled, being the position accuracy of the translational stage down to* 100 nm *(see § 4.1).*

Therefore, the pupil remapper waveguides must be matched in length with each others. A mathematical procedure is required, able to adjust the curvature and the direction of each line [72]. Notice that for the DBC, no further modification is needed since all the waveguides already have the same length.

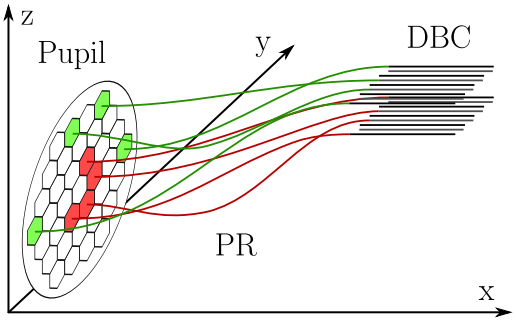

Figure 5.4: Graphical representation of the device. The eight pupil remapper waveguides connect the telescope pupil to the two DBCs. The coordinate axes are also shown.

However, only the geometrical length of the curves can be matched, and not the optical path [23]. The latter is defined as the product of the geometrical length and the local refractive index. Since the induced refractive index contrast slightly varies with the depth (because of the different focusing condition), it is very complex to match the optical length. Nevertheless, it is expected that this issue alters the optical path difference well below the coherence length.

For the waveguides simulations, cubic spline curves have been used [78]. These are $3D$ polynomial functions of order three characterized by a smooth change of the curvature radius, thus reducing the bending losses of the corresponding waveguide. For the sake of simplicity, the process of constructing them will be presented only on the xy plane. Once that is done, it is straightforward to generalize it to the $3D$ space, adding also the z axis.

The first step consists in observing the distance of all the pupil point-DBC input pairs, so to find the largest one. Such waveguide will be the first to be simulated. The corresponding spline curve is computed with the only requirements of the starting and ending points. Its length is also computed.

All the other paths are generated with an additional requirement: the middle point along the x axis (blue dot in Fig. 5.5) is left free to move on the y axis in order to match its length with the first spline curve. Indeed, if one of these waveguides had been constructed without moving such central point, it would have been shorter, as can be seen from Fig. 5.5.

Other than the length-matching, many other constraints must be taken into account in the simulation of the remapper:

- The waveguides should start and finish with zero first derivative, in order to minimize the coupling losses (see § 4.3.2). For this reason, a short straight region is added to both ends of the waveguide (red segments in Fig. 5.5).

- The waveguides should not be too close to each other, otherwise some light

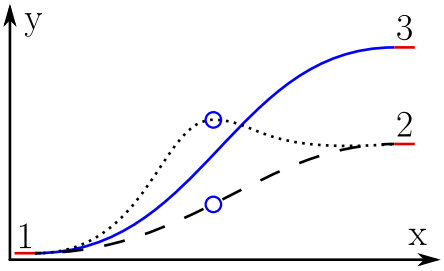

Figure 5.5: Length-matching algorithm for the spline curves. The blue curve (connecting points 1 and 3) is the first spline to be built, called primitive, without the free point. The spline connecting points 1 and 2, if built without the free point too, results in a lower length (dashed line). To ensure the length-matching, such curve has to expand in the plane (dotted line). Adapted from [72].

can couple from one to the other, losing the desired interference pattern.

- The waveguides should not have a too low minimum curvature radius. Otherwise, the bending losses become dominant, and too much light is lost during propagation (see § 4.3.3).

Another use of the remapper is to decrease the amount of stray light. Indeed, the glass itself acts as a waveguide with respect to the air around it, and if some light is not coupled into the waveguides, it is guided all the way to the output of the device. With the pupil remapper, the output is carried to a position different from the input waveguides, thus reducing significantly this effect, as can be seen from Fig. 5.6.

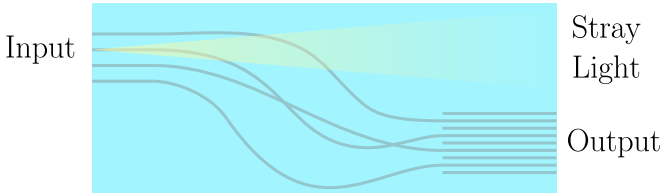

Figure 5.6: Pictorial representation of the top of the device. The pupil remapper has also the function of reducing the amount of stray light present at the device output. Light is injected only at one of the four inputs.

Chapter 6

Device Fabrication and Characterization

In Ch. 5 the device geometry has been defined. In the current chapter, the fabrication process leading to the device implementation will be described.

The first step consists in finding the set of fabrication parameters (see § 3.3) best suited for the writing of the current device. With those parameters it will be possible to experimentally study the behavior of the device, firstly analyzed in simpler parts (e.g. DBC or pupil remapper alone), and then as a whole. With this it is possible to tailor some characteristic device parameters that have been not addressed so far, like its length or the required depth inside the substrate.

Every fabrication has been carried out on the borosilicate glass substrate Corning Eagle XG and employing the FLM technique presented in Ch. 3. After proper annealing of the devices, they have been characterized with laser light at 1550 nm.

6.1 Optimization Process

The optimization process required to experimentally tailor all the device parameters is now outlined. Starting with straight and bent waveguides in order to find the optimal fabrication parameters, the section will be concluded with the analysis of more complex structures, like waveguides array or the pupil remapper.

6.1.1 Straight Waveguides

An important parameter during the inscription process is represented by the focusing depth inside the glass sample. By increasing it, the spherical aberrations induced by the air-glass interface increase as well, thus changing the waveguide properties. For this reason, it is not straightforward to find a combination of fabrication parameters providing a high-quality waveguide at different depths.

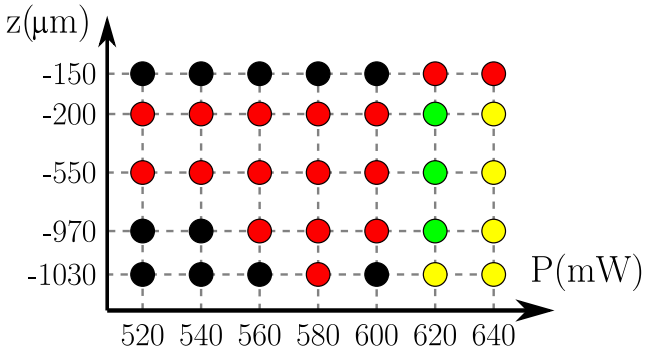

Figure 6.1: Straight waveguides fabrication scans for different laser power. The writing speed is 40 mm/s. Black dots represent either a non-guiding region or a multi-mode waveguide. Red dots represent high losses, while green one low losses. Yellow dots are in a middle region between the two.

Therefore, the first step for the optimization of the fabrication process is to inscribe a set of straight waveguides changing the laser power, the writing speed and the depth inside the sample. The first two parameters are used to find the region where high-quality waveguides can be fabricated. Instead, the depth analysis is done to check the maximum range that can be covered. The required depth range is 866 μm, as has been explained in § 5.1.

Other parameters like the repetition rate (1 MHz) and scan number (6) have been kept fixed to optimal values already known from previous tests. A partial microscope image of the sample input facet is shown in Fig. 6.2. In each image, the leftmost waveguides have been fabricated at 20 mm/s, the rightmost ones at 40 mm/s. In the left image $P = 520$ mW; in the right one $P = 640$ mW. Notice that in both images the waveguide dimension is decreased as the writing speed increases. Moreover, it can be seen that the waveguide dimension also increases as the writing power is increased.

The propagation losses have been characterized with the fiber-butt coupling configuration (see Fig. 4.3b). The optimal writing speed has been assessed to be 40 mm/s. Fixing that speed, all the waveguides losses are shown schematically in Fig. 6.1. A color code is used to qualitatively represent the waveguide loss. The optimal laser power turn out to be 620 mW.

For these optimal parameters, the waveguide behavior as a function of the inscription depth is shown in Tab. 6.1. The mode diameter is shown, together with the coupling and propagation losses. The corresponding camera-acquired images are shown in Fig. 6.3.

Too shallow waveguides are multi-mode. Since too much energy is deposited into the material, the waveguide diameter is too big, thus supporting also higher order modes and not only the fundamental one. On the other hand, if focusing the

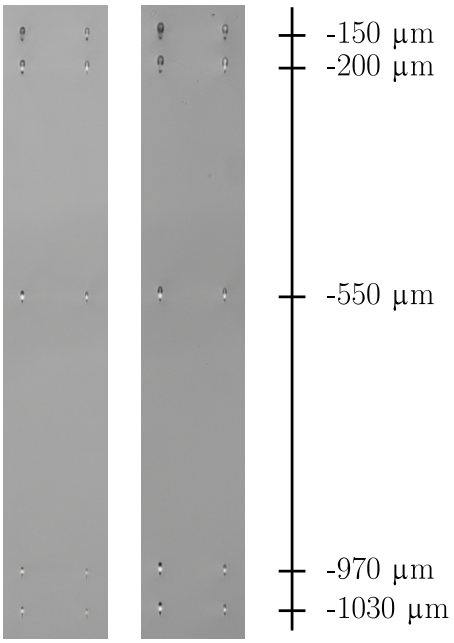

Figure 6.2: Microscope image of the input facet of a sample with straight waveguides. In the left image the writing power is 520 mW and the speed 20 and 40 mm/s. In the right image the speeds are the same but the power is increased to 640 mW.

beam too close to the bottom surface, the glass gets ablated and no waveguide is created. After a further analysis, the best compromise found – with the power and speed already discussed – is to fabricate within a depth from -190 µm to -1057 µm from the top surface. The samples used have a depth of 1.1 mm.

Depth [µm]	**Dimension** [µm]	**CL** [dB]	**PL** [dB/cm]
-150	multi-mode	-	-
-200	9 x 10	0.13	0.23
-550	8 x 9	0.15	0.26
-970	10 x 10	0.10	0.34
-1030	10 x 10	0.08	0.40

Table 6.1: Straight waveguides parameters as a function of the inscription depth. The mode dimension, the coupling loss and the propagation loss are shown. Writing speed 40 mm/s, laser power 620 mW. The waveguide at -150 µm is multi-mode.

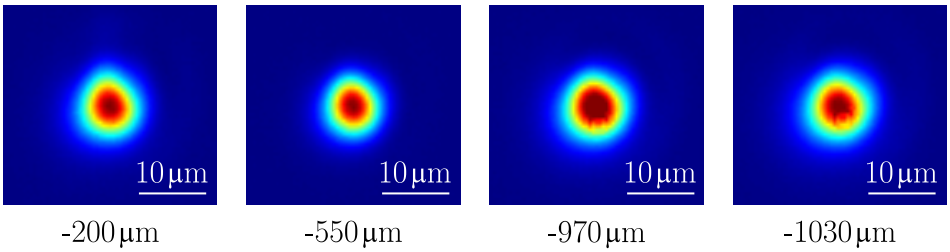

Figure 6.3: Straight waveguide modes acquired by the camera, as a function of inscription depth. The multi-mode waveguide at d = -150 µm is not shown.

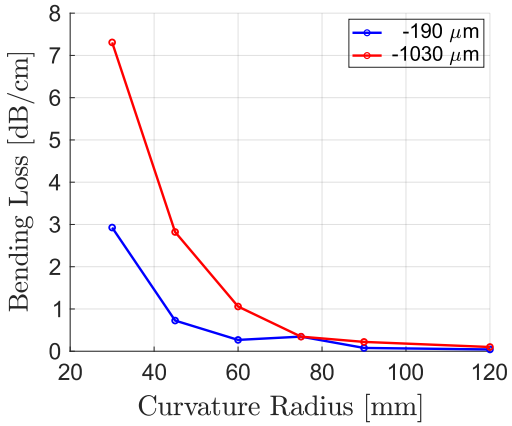

Figure 6.4: Bending loss [dB/cm] dependence with the curvature radius [mm]. Set of waveguides at -190 µm (blue curve) and at -1030 µm (red curve) from the sample top surface are shown.

6.1.2 Bending Waveguides

Since in the current work many curved waveguides have to be fabricated in the pupil remapper region, an analysis of the bending loss is required. To do so, waveguides with the parameters chosen in the previous section but with a finite curvature radius have been fabricated, following what was presented in §4.3.3. The measured bending losses for waveguides at 190 µm depth from the top surface are shown in Fig. 6.4 (blue curve).

It has been found that a minimum curvature radius of 50 mm is required in order to have a negligible amount of bending loss (e.g. 0.5 dB/cm) at all the depths. However, when the waveguide is fabricated near the sample bottom surface, the bending loss greatly increases. See for example Fig. 6.4 (red curve), where the bending losses of 1030 µm deep waveguides are shown. Fortunately, as will be shown later, the geometry of the final device requires a low curvature radius at depths far from the bottom sample surface. This means that at the critical depth

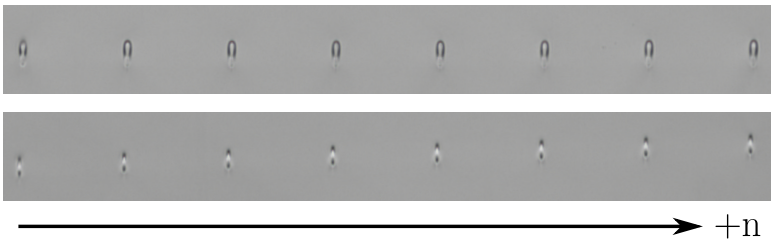

Figure 6.5: Microscope images of the waveguides fabricated for the refractive index optimization. The above waveguides are at 250 μm from the top surface; below they are at 1 mm.

the curvature radius is quite high, thus preventing the waveguide to lose too much light.

6.1.3 Refractive Index Optimization

During the fabrication trials discussed in the previous sections, it has been noticed that the deepest waveguides were fabricated at a slightly different depth than what expected. This effect is here evident since the waveguides have been fabricated spanning many different depths.

Recall that at the laser pulse repetition rate employed (1 MHz), cumulative heating is present at the beam focus (see § 3.3.2). As a consequence, the guiding region is at a slightly different spatial position with respect to the laser focus. The main issue is that this excursion depends on the inscription depth.

Usually, in order to fabricate a waveguide at depth z from the surface, it is necessary to tailor the fabrication as if the wanted focus would have been at $z_0 = z/n$, where n is the substrate refractive index. This is done in order to compensate for the Snell refraction of the beam at the air-glass interface. It is the stage software that takes care of operating this change.

It has been thought that by modifying the refractive index provided to the stage software, it might be possible to compensate the waveguide depth excursion. In particular, an *effective* refractive index for the current device has to be found. This means to find the refractive index value allowing for the same mismatch – at all depths – between the beam focus and the guiding region.

Notice that this is not the actual substrate refractive index at the working wavelength. Indeed, the attention is here on the waveguide guiding region rather than on the beam focal point. This effective refractive index refers only to waveguides obtained with the above-mentioned fabrication parameters.

To this end, many straight waveguides have been fabricated, at various depths. For each set, a different refractive index has been considered in the fabrication procedure: from 1.49 to 1.53.

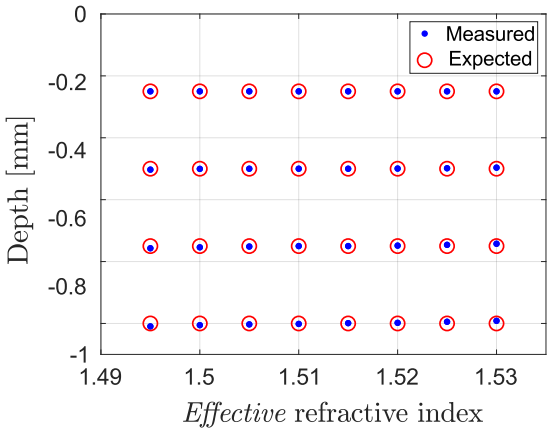

Figure 6.6: Comparison of measured guiding region (blue dot) with the expected one (red circle) for waveguides at different depth and *effective* refractive index.

In Fig. 6.5 are shown two microscope images of the waveguides at 250 µm and 1 mm from the top surface, for increasing refractive index. It can be seen that the waveguides are written at different depths inside the sample, as the effective refractive index is modified.

The sample has been characterized with the fiber-butt coupling configuration (see Fig. 4.3b). The fiber and the output objective have been mounted on two separate PI Hexapods: automated translational stages with a precision of 200 nm. By maximizing the power transmitted in each waveguide, it has been possible to locate the guiding regions. The measured positions, compared to the expected ones, are represented graphically in Fig. 6.6.

The best condition allowing for the minimal mismatch between the measured position and the expected one is when $n = 1.5125$, slightly above the original value. This will be the glass refractive index used in all the subsequent fabrications.

6.1.4 1D Waveguides Array

Once the single waveguide parameters have been chosen, array of waveguides can be fabricated. Since the global behavior of many coupled waveguides is complex, the first step consists in studying a simplified version: a one-dimensional array. To this end, only the $1D$ coupling between waveguides is now addressed. The results can then be used to study a more complex geometry, as the zigzag configuration of the DBC.

The linear array geometry used is constituted of 31 straight waveguides placed on the same plane. Light is injected in the central waveguide, which is longer than the others.

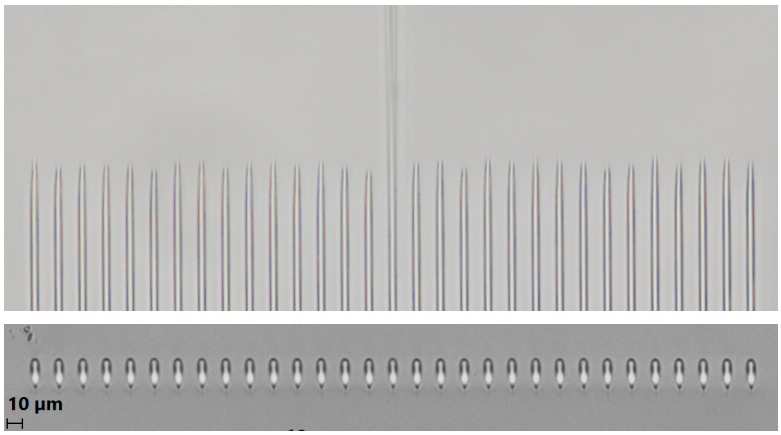

Figure 6.7: Microscope images of a 31-waveguides linear array. The device is shown from above and from the input facet, respectively.

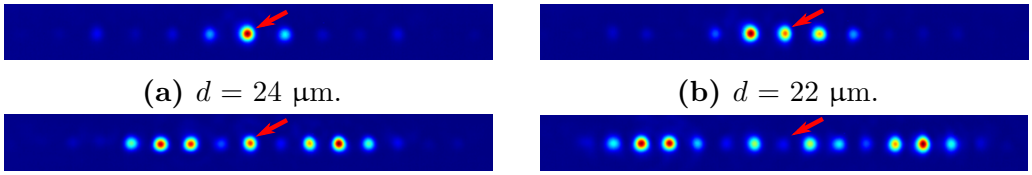

(a) $d = 24$ µm. **(b)** $d = 22$ µm.

(c) $d = 19$ µm. **(d)** $d = 18$ µm.

Figure 6.8: Output intensity distribution acquired by the camera for linear arrays with different spacing d between the waveguides. The array length is L = 20 mm. The red arrow highlights the input waveguide.

Light propagation inside the array is studied collecting the output intensity distribution with a camera. For this work, an InGaAs camera Xenics Bobcat 640 has been used. Since the losses are not the main concern (they have been already optimized) and since a polarization analysis will be carried out, an end-fire coupling configuration (see Fig. 4.3a) has been adopted to study the array.

The arrays have been placed at depth of 431 µm and 361 µm from the top glass surface, since at those positions the final DBCs will be fabricated. Thus the waveguides array behavior at the desired depth can be studied. Microscope images of the top and the output facet of a linear array are shown in Fig. 6.7.

Two are the parameters affecting the array behavior: its length and the distance between the waveguides. Actually, only the latter influences the coupling coefficient between waveguides. The array length is tailored in order to better highlight this dependence.

Indeed, a too short array is not able to efficiently couple all the modes with each other: light may remain concentrated on just few waveguides. On the other hand,

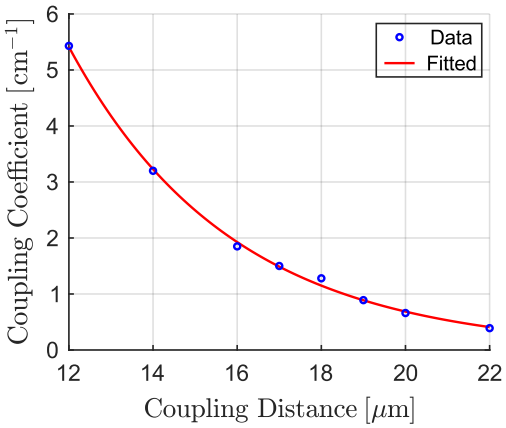

Figure 6.9: Coupling coefficient [cm^{-1}] dependence with different waveguide spacing [µm] for a 31-waveguides linear array.

in a too long array, light can reach the boundaries, thus introducing deviations from the ideal situation.

Different arrays have been fabricated, changing the length and the waveguides spacing. The output intensity distribution was acquired. Fig. 6.8 shows an example of four linear arrays with length 20 mm and waveguide spacing varying from 18 to 24 µm.

For each configuration the coupling coefficient has been studied. To do this, the theoretical behavior of an array of N identical waveguides must be addressed.

The light propagation inside the structure can be obtained solving the coupled mode equations

$$i\,\frac{\mathrm{d}A_n}{\mathrm{d}z} = \sum_{m\neq n}^{N} \kappa_{n,m} A_m \tag{6.1}$$

which can be rewritten in matrix form as

$$i\,\frac{\mathrm{d}A}{\mathrm{d}z} = \underline{\underline{K}}\,A \tag{6.2}$$

$\underline{\underline{K}}$ is the coupling coefficients matrix and A is the column vector of the various waveguide amplitudes at a given z position along the propagation direction.

In the case of a linear array, each waveguide can couple with the two closest to it (neglecting higher-order coupling). The coupling is identical in both directions. Therefore, the $\underline{\underline{K}}$ matrix can be written as

$$\underline{\underline{K}} = \begin{pmatrix} 0 & \kappa & 0 & \dots & 0 \\ \kappa & 0 & \kappa & \dots & 0 \\ 0 & \kappa & 0 & \dots & 0 \\ \vdots & \vdots & \vdots & \ddots & \vdots \\ 0 & 0 & 0 & \dots & 0 \end{pmatrix} \tag{6.3}$$

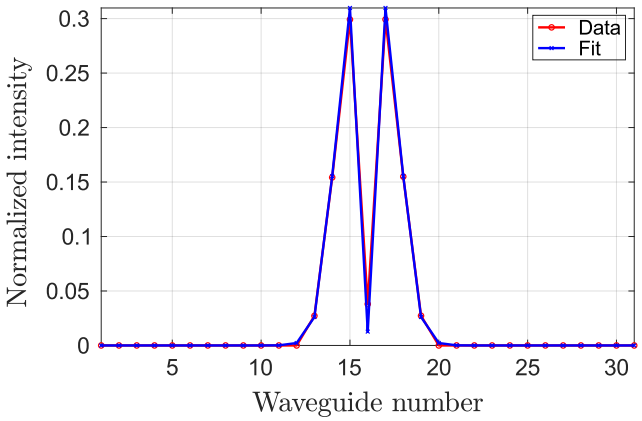

Figure 6.10: Comparison between acquired data and the corresponding fit for a linear array with $L = 5$ mm and $d = 14$ µm. On the abscissa there is the waveguide number and on the ordinate the normalized intensity.

By fitting Eq. 6.2 with the captured data (i.e. the elements of A), κ can be extrapolated. The extrapolated coupling coefficients have been plotted in Fig. 6.9 as a function of the corresponding waveguide spacing (the array length is fixed at $L = 20$ mm). In the same picture, the exponential fit is also shown. It can be noticed that the coupling coefficient decreases exponentially as the waveguide spacing increases. Indeed, the farther away are the waveguides and the weaker is the overlap between the corresponding modes.

In order to test the goodness of the fit, the acquired distribution has been compared with the theoretical one, expected with the extrapolated coupling coefficient. An example is shown in Fig. 6.10 for a $L = 5$ mm and $d = 14$ µm linear array.

For the device, the coupling coefficient should be as high as possible, in order to reduce the device length. However, if the waveguides are fabricated too close, detuning and additional stress may appear due to the partial overlap of the modified regions. For this reason, a good compromise was found to be a distance of 16 µm. In this case, the fitted coupling coefficient is $\kappa = 1.85$ cm^{-1}.

6.1.5 Temperature Dependence

Another aspect in the device characterization, is its eventual behavior variation with temperature. Indeed, all previous tests have been carried out at room temperature (around 21 °C), while the final use of the device is on top of a mountain at the William Herschel Telescope. There is a great temperature excursion, which may degrade the device performances.

To test the amount of change, different temperature gradients have been applied to a $1D$ array ($L = 10$ mm, $d = 16$ µm), using a Peltier module. With a thermocouple

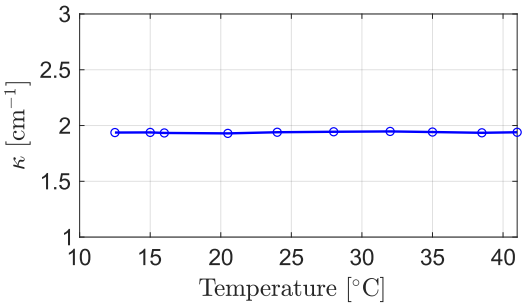

Figure 6.11: Coupling coefficient [cm^{-1}] dependence with the temperature [°C], for a linear array of 31 waveguides.

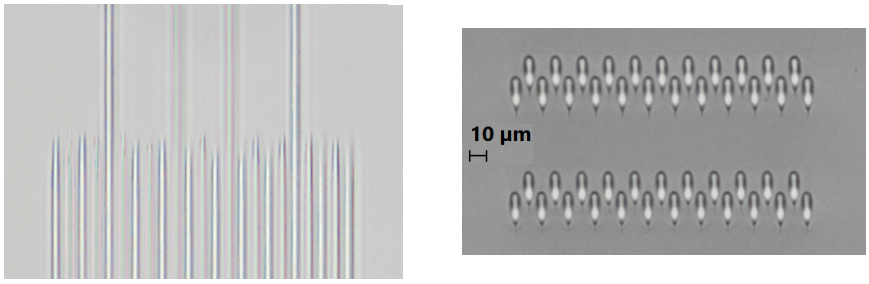

Figure 6.12: Microscope images of two 23-waveguides zigzag arrays. The device is shown from above and from the input facet, respectively.

the temperature was constantly monitored.

The covered temperature are from 10 °C to 40 °C. Within this range, ten points have been collected, capturing the intensity distribution with the camera. The data have been analyzed and the coupling coefficients have been extrapolated. Fig. 6.11 shows the coefficient variation with the temperature. In the temperature range studied, it changed from 1.93 to 1.95 cm^{-1}: a variation of 1% with respect to the unperturbed condition. Since, such value is below the variability of the measurement, it can be assumed that the device does not change significantly its behavior, ensuring a high stability to the temperature.

6.1.6 2D Waveguides Array

This step is done in order to study the waveguide coupling in two dimensions. The aim is to find the configuration allowing for $\kappa_h = \kappa_d$. The parameters that can be changed in order to obtain the desired behavior are two: the array length and the angle θ between the planes, as in Fig. 5.1.

The arrays are placed at a depth of 431 µm and 361 µm from the sample top surface, i.e. the depths of the final device DBCs. Notice that the distance between

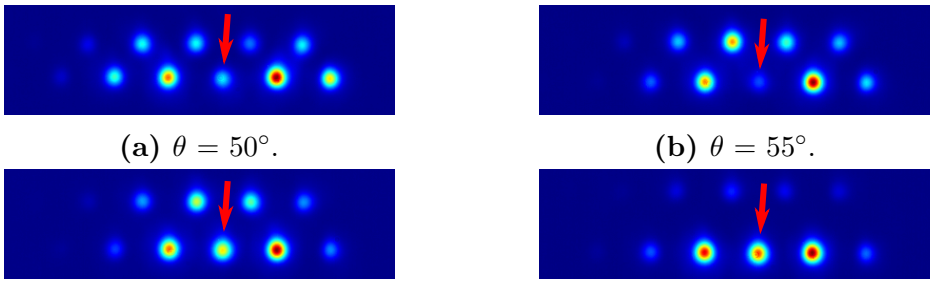

(a) $\theta = 50°$. **(b)** $\theta = 55°$.

(c) $\theta = 60°$. **(d)** $\theta = 65°$.

Figure 6.13: Output intensity distributions acquired by the camera for zigzag arrays with different angle θ between the planes. $L = 5$ mm and $d = 16$ µm. The red arrow highlights the input waveguide.

them is 70 µm, sufficient to avoid any kind of coupling between them. The two DBCs must indeed work independently. Microscope images of the two zigzag arrays are shown in Fig. 6.12.

Many arrays have been fabricated slightly changing their parameters. The four waveguides corresponding to the inputs are longer than the others, so to ease the light injection. Fig. 6.13 shows a comparison of the output distribution for arrays with different angle θ but same length $L = 5$ mm (and same input site). As the angle is increased, the coupling between waveguides on opposite planes becomes weaker. Notice that the array is only 5 mm short: in this way, the fit to retrieve the coupling coefficients is more reliable. Indeed, light does not reach the boundary waveguides, so that propagation remains symmetric. This is why in Fig. 6.13 only up to eleven waveguides have a non-null output.

The optimal configuration has been found to be with $L = 20$ mm and $\theta = 60°$. The characterization of the device is similar to what has been done in §6.1.4. In this case, the $\underline{\underline{K}}$ matrix contains two types of terms: κ_d and κ_h. The former represents the first-order coupling; the latter the second-order one. Higher-order couplings are neglected. The $\underline{\underline{K}}$ matrix can then be written as

$$\underline{\underline{K}} = \begin{pmatrix} 0 & \kappa_d & \kappa_h & 0 & \dots & 0 \\ \kappa_d & 0 & \kappa_d & \kappa_h & \dots & 0 \\ \kappa_h & \kappa_d & 0 & \kappa_d & \dots & 0 \\ 0 & \kappa_h & \kappa_d & 0 & \dots & 0 \\ \vdots & \vdots & \vdots & \vdots & \ddots & \vdots \\ 0 & 0 & 0 & 0 & \dots & 0 \end{pmatrix} \tag{6.4}$$

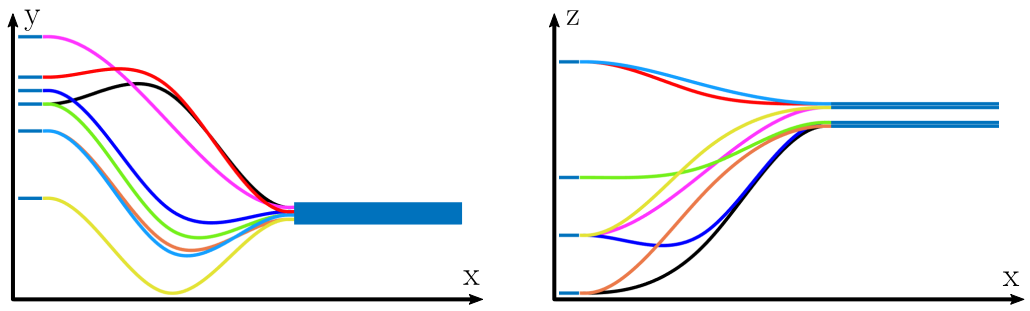

(a) xy plane. **(b)** xz plane.

Figure 6.14: Simulations of the device in the xy and xz planes. The 8 waveguides are shown with different colors. After the pupil remapper, the two DBCs are shown. Pictures not in scale.

6.1.7 Pupil Remapper

The pupil remapper is built following what has been presented in § 5.1.1. With the explained procedure, the waveguides result with identical geometrical length. Other than that, also the other requirements must be satisfied. For example, in order to ensure zero derivative at both extremes of each remapper waveguide, two straight regions of 1 mm each have been added.

Moreover, a minimal distance of 30 µm from any two point of any waveguides is required in order to avoid inter-coupling. The light coupling should take place only in the DBC region, and not in the remapper.

The fabrication order of the waveguides should follow a precise order. The laser used for the waveguide writing cannot be focused through a previously modified region of the glass, otherwise the strong aberrations distort the beam, causing it to be focused at a different position. For this reason, the waveguides have to be fabricated in sequence from the deepest to the shallowest.

After some simulations, the pupil remapper configuration satisfying all those requirements has been found. With a length of 35 mm along the x axis, the minimum curvature radius reached is 52 mm, above the 50 mm threshold found in § 6.1.2.

A pupil remapper (without the DBCs at its end) has been fabricated, following the simulations. Each waveguide has been characterized with a fiber-butt coupling configuration (see Fig. 4.3b), in order to determine the amount of loss introduced. The propagation loss turned out to be in the range $0.3 \div 0.4$ dB/cm for all the waveguides. Other than the loss study, this part is useful also to verify the absence of eventual coupling between the waveguides.

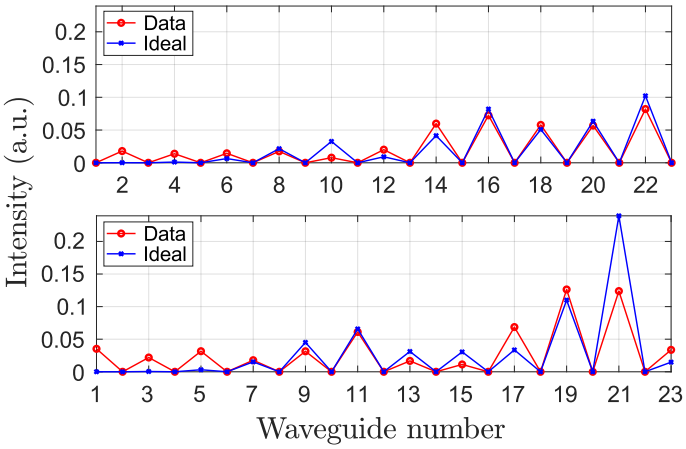

Figure 6.15: Comparison between acquired data and simulated intensity distribution for a 23-waveguide zigzag DBC, with input at the 19-th waveguide. On the abscissa there is the waveguide number and on the ordinate the normalized intensity. The upper and lower DBC planes are shown separately.

6.2 Final Device

In Fig. 6.14 is shown a MATLAB® simulation of the complete device, from above and from the side. The pupil remapper waveguides connect the eight inputs to the two DBCs. The device is 60 mm long along the x direction, 1.5 mm wide along y and 0.866 mm deep.

Many devices have been fabricated on the same sample, slightly changing the DBC parameters with respect to the ones optimized in § 6.1.6. This is done for a reproducibility reason: each fabrication slightly differs from the others so that the optimal device may actually depend on the fabrication. The pupil remapper configuration and length have been kept fixed.

The devices have been characterized by injecting light into each pupil remapper input, one at a time. The output intensity distribution has been collected with the camera. The acquired data have been analyzed as in §6.1.6. By fitting the acquired data it is possible to determine both coupling coefficients. The optimal device is the one resembling with the lowest error and for the highest number of inputs, the condition $\kappa_h = \kappa_d$.

Moreover, the acquired data should also be compared with the theoretical intensity distribution, obtained simulating numerically the propagation of light inside the structure. To perform this comparison, the *similarity* has been used as a figure of merit. It is defined as

$$S = \left(\sum_{k=1}^{N} \sqrt{v_k^{id} \cdot v_k^{exp}} \right)^2 \tag{6.5}$$

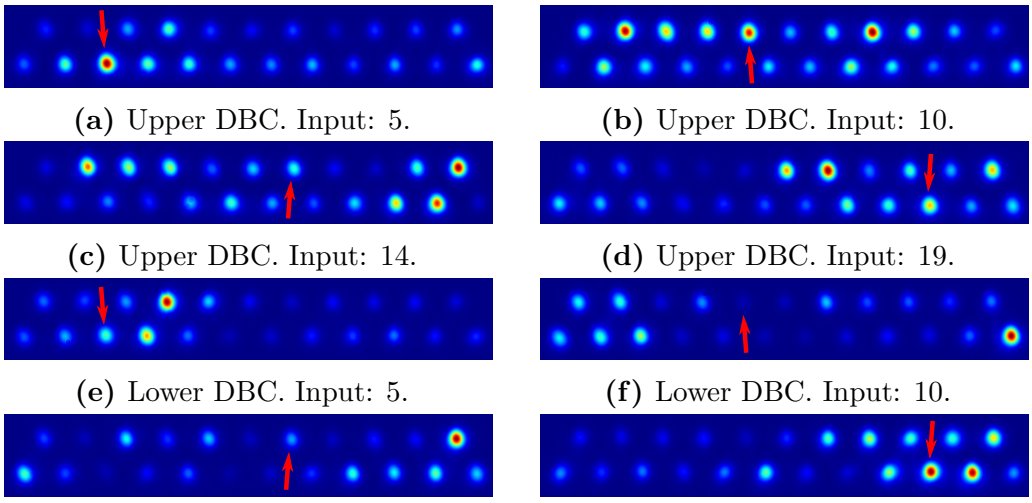

(a) Upper DBC. Input: 5. **(b)** Upper DBC. Input: 10.

(c) Upper DBC. Input: 14. **(d)** Upper DBC. Input: 19.

(e) Lower DBC. Input: 5. **(f)** Lower DBC. Input: 10.

(g) Lower DBC. Input: 14. **(h)** Lower DBC. Input: 19.

Figure 6.16: Output intensity distribution acquired by the camera for the upper and lower DBC. The red arrow highlights the input waveguide.

where v_{id} and v_{exp} are the column vectors (with size N) containing the normalized peak intensities of the ideal and measured output distributions, respectively. When $S = 1$, the two a distributions are identical. Fig. 6.15 shows an example of comparison between the acquired distribution and the theoretical one for a DBC with input at waveguide 19. The similarity achieved is $S = 0.87$.

The optimal device, better satisfying the given requirements turned out to be the one with $L = 21$ mm and $\theta = 59°$. The output intensity distributions acquired by the camera are shown in Fig. 6.16 for all the eight different inputs.

Since the two DBCs are identical, the output intensity distribution should be equal if light is injected in the same input waveguide. However, it has been found that the two distributions are quite different, as it is possible to notice observing pictures with the same input but different DBC in Fig. 6.16.

It is possible that such difference is due to the variability in the fabrication process. Even a difference as small as 100 nm in the two arrays can generate a different interference pattern. Moreover, also the different depth position of the DBCs may play a role. Since the evanescent coupling is very sensitive to the waveguide properties, even a small variation due to a different fabrication depth may modify it.

6.2.1 Polarization Analysis

In § 5.1, the device polarization-insensitivity has been presented as a fundamental requirement: the device must act on all the polarizations with the same behavior.

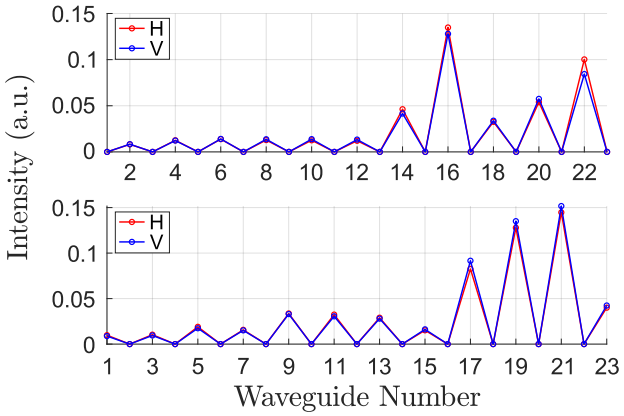

Figure 6.17: Comparison between acquired data for a 23-waveguide zigzag DBC with input light at two perpendicular polarizations: horizontal (red curve) and vertical (blue curve). The input is at the 19-th waveguide. On the abscissa the is the waveguide number and on the ordinate the normalized intensity. The upper and lower DBC planes are shown separately.

This can be tested through a polarization analysis of the device.

Each device input has been analyzed with two perpendicular polarizations – called here vertical (V) and horizontal (H). The setup used is the end-fire coupling (see Fig. 4.3b) together with a polarizer and a half-wave plate to fix the input light polarization.

The output intensity distribution has been compared in the two cases. No difference in the interference pattern has been observed, meaning that the device behaves in the same way with all the polarizations. Hence it can be used with any kind of unpolarized light, as required. An example is shown in Fig. 6.17; the similarity between the H (red curve) and V (blue curve) polarizations is $S = 0.99$. The distributions differ slightly only around the rightmost waveguides. This could be due to boundary effects.

6.2.2 Condition Number Characterization

What presented so far has been obtained in the laboratories of the IFN-CNR, inside the Physics Department of Politecnico di Milano, where the devices have been fabricated and analyzed. In the remainder of this chapter, the characterization carried out at the Leibniz Institute for Astrophysics Potsdam will be presented.

Employing the procedure explained in § 4.4, the $V2PM$ for the current device has been derived and the condition number obtained. The characterization has been carried out with a tunable source from 1500 nm to 1600 nm in order to test the wavelength behavior of the device.

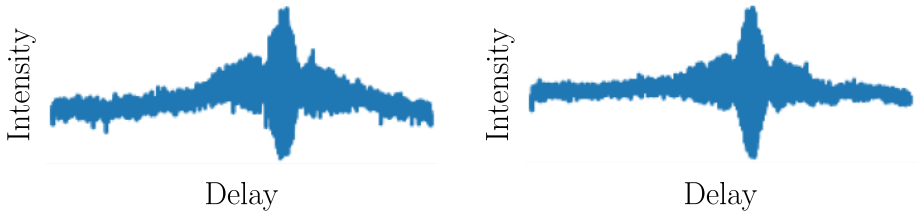

Figure 6.18: Polychromatic fringe pattern as a function of the delay, measured for two different baselines. The output has been recorded from waveguide number 14 of the upper DBC.

Light has been injected in the device with the modified Michelson interferometer setup presented in § 4.4. In Fig. 6.18 is shown an example of the polychromatic intensity pattern of one of the output waveguides for two different input baselines. Repeating the procedure for all input baselines and for all the output waveguides, the complete polychromatic $V2PM$ can be obtained (see § 4.4). From here, the condition number can be extrapolated. Fig. 6.19 shows its dependence with the wavelength.

Notice that the device has been optimized for a 1550 nm wavelength. However, the condition number at $\lambda = 1550$ nm is not the lowest. In other words, the device may present better performances at higher wavelengths. This is one of the reasons the wavelength dependence of the device should be studied more deeply, as will be explained in Ch. 7.

As the final step, the goodness of the matrix inversion has been tested. To do this, a known source is injected in the device – as usual with a two-points excitation – and the output intensity is acquired. The data are used in Eq. 2.26, together with the $P2VM$ calculated in order to obtain experimentally the input light coherence, i.e. the G vector elements.

Since the input source is known, its visibility is known too. It can be compared with the experimental one just obtained, in order to check the similarities. The visibility has been defined in § 2.2 and § 2.3.1 as the normalized MCF between two electric fields at the same time instant, i.e. $\tau = 0$. However, in the current analysis of the condition number, it is necessary to generalize its definition.

In this situation, a delay τ is introduced between the fields. Resorting to Eq. 2.2, the new visibility definition taking into account the temporal delay is

$$V_{i,j} = \frac{E_i(t)E_j(t-\tau)}{\sqrt{|E_i(t)|^2|E_j(t-\tau)|^2}} = \frac{E_0(t)E_0(t-\tau)}{I_0} \tag{6.6}$$

where $E_i(t) = E_0(t)/2$ and $E_j(t-\tau) = E_0(t-\tau)/2$ have been used in the last equivalence. Indeed, the input fields at positions i and j are the same – and both equal to half the initial known value E_0. Moreover, the input field intensity $I_0 = |E_0(t)|^2$ is constant with time.

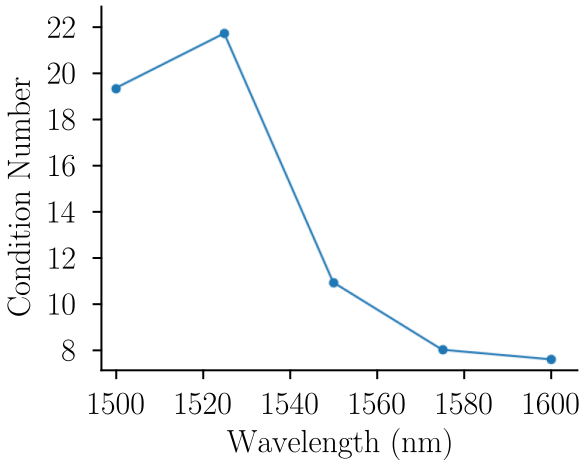

Figure 6.19: Condition number as a function of the wavelength. The values of CN have been extrapolated from the $V2PM$.

Being the electric field a complex function, the corresponding visibility can be represented in the complex plane. Looking at Eq. 6.6, it is possible to conclude that the theoretical visibility is a circle centered in the origin with unitary radius. Indeed, the injected field at two spatial positions is the same. Hence $V_{i,j} = e^{i\omega\tau}$ with unitary modulus and τ-dependent phase.

Fig. 6.20 shows examples of acquired visibility, compared with the theoretical value, for four input baselines. Points with the same color represent the same wavelength but different delay τ between the input fields.

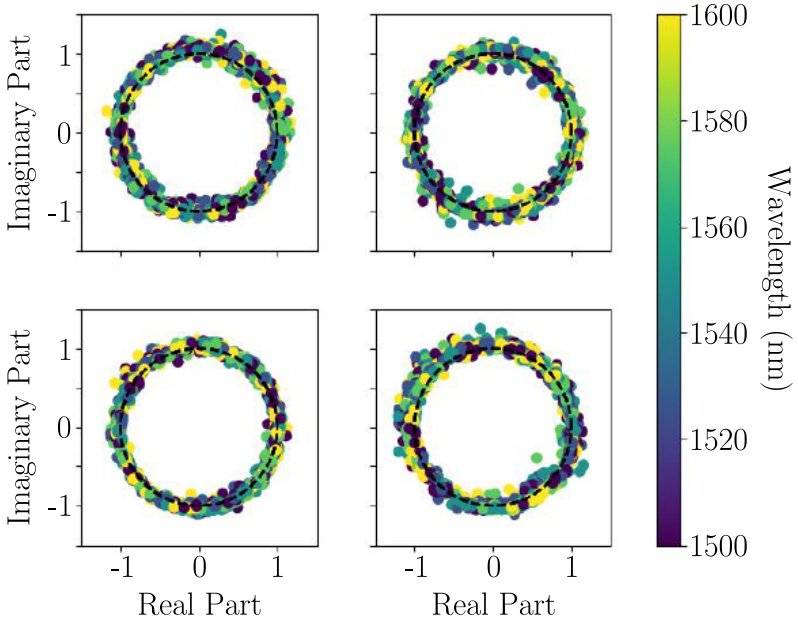

Figure 6.20: Retrieved visibility for four baselines and at different wavelengths, represented in the complex plane. The black dashed circle is the expected visibility of the input source.

Chapter 7

Broadband Directional Couplers

The final part of this work is centered on the polychromatic behavior of the device. As can be seen from Fig. 6.19, the condition number strongly depends on the input wavelength. This means that the $V2PM$ is modified whenever the wavelength changes. This is not a desired behavior since a telescope observation is intrinsically polychromatic. The ideal condition would be a flat response of the device within all the studied wavelength range.

The wavelength dependence study of the complete device is complex since many waveguides must be taken into account. As the initial step, the wavelength behavior of a much simpler device can be studied, namely the directional coupler. The background theory is more complete and easier to treat analytically.

The purpose of this chapter is to analyze in detail the wavelength dependence of a directional coupler. Initially, the structure will be presented, together with its governing equations. After that, the wavelength sensitivity of the device is studied, showing how it is possible to increase the device bandwidth. In order to do so, both theoretical simulations and experimental sessions are carried out.

7.1 Directional Coupler

A directional coupler is composed by two evanescently-coupled waveguides. The modes propagating into them are able to exchange energy between each other. The coupling is present in a central straight region of length L_c, as can be seen from Fig. 7.1. At the device input and output, the arms are much more distant so to ease the light injection and collection.

In its simplest form, when a field is injected just in one input, a directional coupler acts as a beam splitter. The normalized power coming out from the same waveguide where the input field has been injected is called *reflection* R. The one from the other arm is called *transmission* T. The ratio between the light intensity exiting the two arms can be tailored modifying the device geometry.

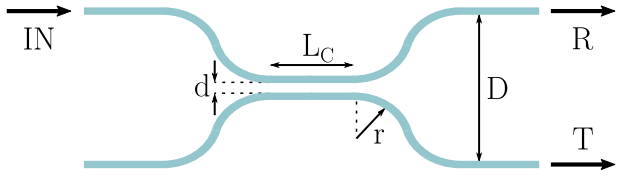

Figure 7.1: Graphical representation of a directional coupler. The power is injected in one arm and the output collected from both. L_c is the coupling region length and d the waveguides distance there. r is the radius of the bending curves and D the maximum distance between the waveguides.

A coupler is characterized by the length of its coupling region L_c and by the spacing d of the waveguides there. Other parameters are the curvature radius r of the bending paths and the maximum distance D between the waveguides.

The propagation of the modes inside the waveguides can be described through the coupled mode equations [40], explained in detail in App. A. Within the coupling region, the normalized mode power propagation can be described as (see Eqs. A.11):

$$\begin{cases} R(z) = \cos^2(\sigma z) + \dfrac{\delta^2}{\delta^2 + \kappa^2} \sin^2(\sigma z) \\ T(z) = \dfrac{\kappa^2}{\delta^2 + \kappa^2} \sin^2(\sigma z) \end{cases} \tag{7.1}$$

where $\sigma = \sqrt{\delta^2 + \kappa^2}$, $\delta = \Delta\beta/2$ and κ the coupling coefficient. z is the propagation distance inside the coupling region. $\Delta\beta = |\beta_1 - \beta_2|$ is the detuning between the waveguides, i.e. the difference in their propagation constant β_i. The latter is defined as $\beta_i = (2\pi/\lambda)\Delta n_i$, where $\Delta n_i = n_i - n_0$ is the refractive index contrast between the waveguide core and the substrate. Therefore $\Delta\beta = (2\pi/\lambda)\Delta n_{1,2}$, where $\Delta n_{1,2} = \Delta n_1 - \Delta n_2$.

When the two waveguides are identical $\Delta\beta = 0$ and the directional coupler is called *synchronous*. In this case $\sigma = \kappa$. Fig. 7.2 shows the reflection as a function of the propagation distance (in units of π/κ). The transmission is the complementary function to the reflection so that $T = 1 - R$ at any point.

Energy is periodically exchanged between the two waveguides with a spatial period $\Lambda^s = \pi/\kappa$. After one cycle, the initial condition is re-obtained. Notice that after half a period, all the energy has been transferred to the opposite waveguide.

Whenever $\Delta\beta \neq 0$, the power transfer between the waveguides is not complete, i.e. the condition $R = 0$ cannot be achieved anymore. This device is called *asynchornous* directional coupler. In Fig. 7.2 there are two examples of this situation, for different values of $\Delta\beta$. Notice also that the period of the oscillation shrinks as $\Delta\beta$ increases: $\Lambda^a = \pi/\sqrt{\kappa^2 + \delta^2}$.

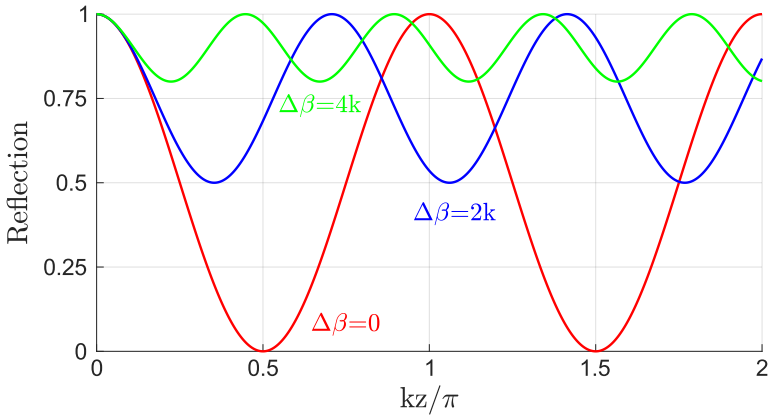

Figure 7.2: Simulations of the coupler reflection as a function of the propagation distance z inside the coupling region (in units of π/κ). Three situations are showed: $\Delta\beta = 0,\ 2\kappa,\ 4\kappa$.

7.1.1 3 dB Directional Coupler

A particular case of directional coupler is when $R(L_c) = T(L_c)$, i.e. the input power has been splitted uniformly at the two waveguide outputs. L_c is the required coupling region length in order to achieve such 50:50 condition. It is also called 3 dB coupler since the power in each of the output arms has been decreased by 3 dB from the input one.

A synchronous 3 dB coupler can be obtained setting

$$L_c = \frac{\Lambda^s}{4} + m\frac{\Lambda^s}{2}, \qquad m = 0, 1, ... \tag{7.2}$$

However, the working point is always on a maximum slope point of the curve. Therefore, even a small error in the device fabrication, will produce large differences in the performances.

A possible solution to this problem is to adopt the asynchronous 3 dB coupler. This time, two conditions have to be satisfied. The reflection amplitude should be 0.5, i.e. $\Delta\beta = 2\kappa$. Moreover, it is also required that

$$L_c = \frac{\Lambda^a}{2} + m\Lambda^a, \qquad m = 0, 1, ... \tag{7.3}$$

In this case, the working point is on a minimum of the curve: the device is more stable to fabrication uncertainties. The 3 dB coupler is the configuration where the difference in stability between the synchronous and asynchronous cases is more pronounced.

7.2 Wavelength Sensitivity

In the remainder of this chapter, the focus will be on the study of the directional coupler wavelength behavior. In order to do so, the reflection dependence from the wavelength has to be addressed.

Looking at Eq. 7.1, the two parameters depending on the wavelength are δ and κ. Concerning the former, it is known that

$$\delta = \frac{\Delta\beta}{2} = \frac{\pi}{\lambda}\Delta n_{1,2} \tag{7.4}$$

so that $\delta \propto \lambda^{-1}$, assuming $\Delta n_{1,2}$ constant (if $\Delta\lambda \ll \lambda$). This last hypothesis is physically reasonable since the wavelength dependence of $\Delta n_{1,2}$ is weaker than λ^{-1}. The induced refractive index contrast Δn_i for a single FLM-waveguide is theoretically wavelength-dependent due to the dispersion relation of glass. However, since the guiding properties of those waveguides are the same in a bandwidth of about 100 nm, the dependence can be considered very weak and similar for both Δn_1 and Δn_2. Therefore, the wavelength dependence of their difference (i.e. $\Delta n_{1,2}$) is negligible in a narrow bandwidth.

On the other hand, the coupling coefficient has a more complex wavelength dependence

$$\kappa_{n,m} = \frac{k_0^2}{2\beta_n} \frac{\iint \psi_m \Delta n_m^2 \psi_n^* \mathrm{d}x\mathrm{d}y}{\iint \psi_m \psi_n^* \mathrm{d}x\mathrm{d}y} \tag{7.5}$$

It is not straightforward to study it analytically because of the overlap integral, where the mode profiles ψ_n have to be known.

A simpler approach is to analyze this dependence experimentally, studying some real directional couplers. Notice that in a real device, the mode coupling is not strictly limited to the coupling region. Indeed, the modes may partially overlap also in the bent regions, i.e. outside the L_c region. This effect can be treated analytically with an additional phase term φ to Eq. 7.1 [79]. The phase of the sine/cosine functions is now $\sigma z + \varphi$.

7.2.1 Coupling Coefficient Wavelength Dependence

In order to study the wavelength dependence of the coupling coefficient, many synchronous directional couplers have been fabricated. Indeed, its governing equation has less parameters with respect to the asynchronous case: κ can be extrapolated with a higher-fidelity fit. The substrate used is Corning Eagle XG borosilicate glass.

Each device has a coupling distance $d = 9$ µm and a curvature radius $r = 60$ mm. The coupling length is varied from 0 to 1.8 mm. For all the devices, the fabrication parameters used are the same used in the straight waveguides optimization (see § 6.1.1). The depth inside the sample is 400 µm (corresponding to a middle way between the DBC positions, see § 5.1).

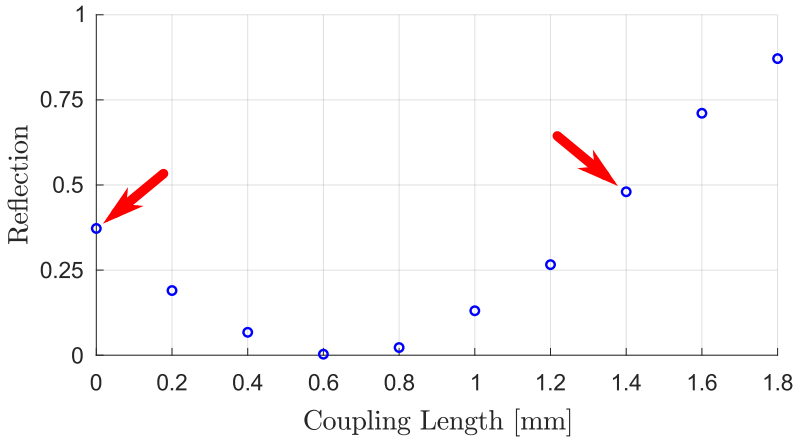

Figure 7.3: Measured reflection for a synchronous directional coupler with writing speed 40 mm/s as a function of the coupling length. The wavelength is fixed at 1550 nm. The couplers used for the subsequent discussion are highlighted by red arrows.

The first step is to fix the wavelength and study the output reflection. Since the devices have different coupling lengths, the reflection curve can be sampled experimentally (see Fig. 7.2). A laser beam at $\lambda = 1550$ nm has been used for this study.

The results are shown in Fig. 7.3, where a periodic oscillation similar to the red curve in Fig. 7.2 can be observed. Notice that with $L_c = 0$ mm, the reflection is different from one. This offset is due to the fact that the modes slightly overlap also before the coupling region.

The wavelength behavior has been carried out on two directional couplers from this set. The first one, with $L_c = 1.4$ mm, has been chosen since it has an almost 50:50 output distribution. The second coupler is the one with $L_c = 0$ mm, chosen in order to retrieve the wavelength dependence of the phase. Indeed, the additional phase term φ added in the previous section is wavelength dependent, but with an unknown functional dependence. This can be explained as follows.

Consider the wavelength-dependent reflection for a synchronous directional coupler

$$R(\lambda) = \cos^2\left[\kappa(\lambda)L_c + \varphi(\lambda)\right] \tag{7.6}$$

In the case $L_c = 0$ mm, the value of φ at a given wavelength $\bar{\lambda}$ can be retrieved by measuring the device response at that same $\bar{\lambda}$

$$R_0(\bar{\lambda}) = \cos^2\left[\varphi(\bar{\lambda})\right] \quad \Longrightarrow \quad \varphi(\bar{\lambda}) = \arccos\left[\sqrt{R_0(\bar{\lambda})}\right] \tag{7.7}$$

The chosen devices have been analyzed at different wavelengths, from 1480 nm

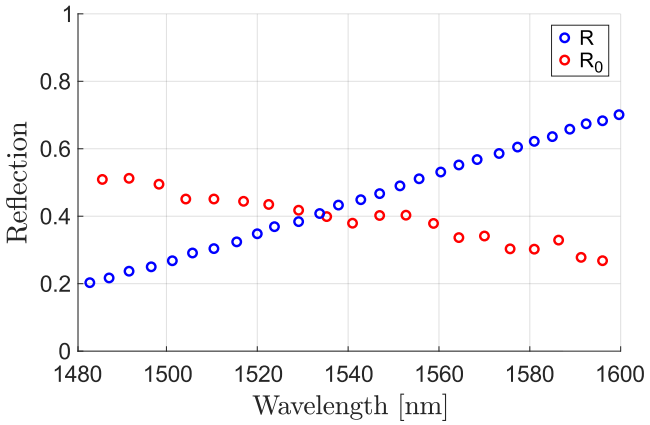

Figure 7.4: Measured reflection of two synchronous directional couplers as a function of wavelength. $L_c = 1.4$ mm for the blue data; $L_c = 0$ mm for the red ones.

to 1600 nm, employing a Santec ECL-200 tunable laser. The reflection has been computed and the data are represented in Fig. 7.4.

From the red curve ($L_c = 0$ mm) a point-to-point wavelength dependence of $\varphi(\lambda)$ can be obtained. These data are then used in Eq. 7.6 to retrieve the coupling coefficient. The latter has been fitted, resulting in a linear relation between κ and λ

$$\kappa(\lambda) = (-4.77 \cdot 10^{-2}\ \text{cm}^{-1}\text{nm}^{-1})\,\lambda + 84.42\ \text{cm}^{-1} \tag{7.8}$$

where λ is measured in nm and κ in cm^{-1}. A comparison between the data and the fit is shown in Fig. 7.5.

It may seem strange that the relation has a negative slope, eventually reaching negative values of κ. However, it must be kept in mind that Eq. 7.8 is valid only within the wavelength range in which it has been obtained. Outside, deviations from this relation are expected. Moreover, notice that from this negative-slope linear relation it follows that the overlap integral (see Eq. 7.5) has a very weak wavelength dependence, within the considered range. Therefore, the assumption that Δn_1 and Δn_2 are approximately constant, is valid.

Example 7. *Consider $\lambda = 1550$ nm. The fitted coupling coefficient is, employing Eq. 7.8, $\kappa \simeq 10.47$ cm^{-1}. This is in good agreement with the fitted κ obtained from Fig. 7.3, which is $\kappa \simeq 10.28$ cm^{-1} (less than 2% difference).*

7.2.2 Theoretical Simulations

The result of the previous section can be used to perform simulations on the expected behavior of different directional couplers. To do this, the Eq. 7.8 has been inserted

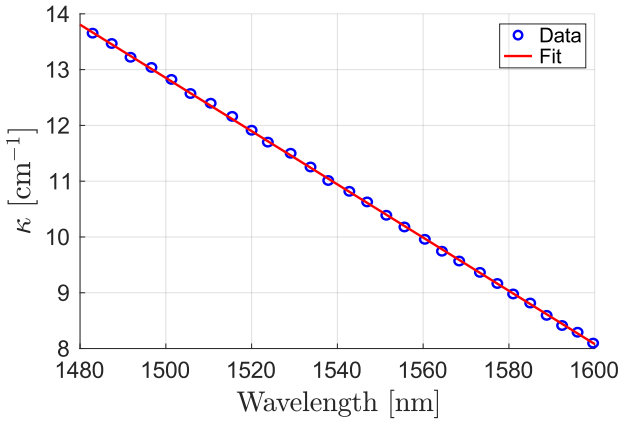

Figure 7.5: Experimental data (extrapolated from the measurements in Fig. 7.4) of the coupling coefficient as a function of wavelength. The corresponding linear fit is also shown (red curve).

into Eq. 7.1. Once again, this has physical meaning only if bounded within the wavelength range in which the coupling coefficient has been studied.

Once a coupling length is fixed, a point of the reflection curve (see Fig. 7.2) is sampled. For this device, the theoretical wavelength is studied. In the current analysis, two characteristic points have been studied, namely a 50:50 and a 100:0 (i.e. $R = 1$) coupler. The behavior is compared between the synchronous and asynchronous cases.

Consider initially the 3 dB synchronous coupler. Since the mean working wavelength of the device is $\lambda_0 = 1550$ nm, it is required that

$$R(L_c, \lambda_0) = T(L_c, \lambda_0) = 0.5 \tag{7.9}$$

where L_c is the coupling length ensuring the 50:50 behavior (at λ_0). L_c can be found employing Eq. 7.2:

$$L_c = \frac{\Lambda^s}{4} = \frac{\pi}{4\kappa(\lambda_0)} \tag{7.10}$$

The wavelength dependence of such device is shown in Fig. 7.6a, blue line. The bandwidth is also highlighted, defined as the wavelength range within which the reflection keeps below a bilateral 0.05 threshold. This is a convention used to compare the wavelength response for different couplers. In this case the bandwidth is 14 nm (from 1543 nm to 1557 nm).

The 3 dB asynchronous case is more complex since also the detuning $\Delta\beta$ has to be decided, together with L_c (which ultimately depends also on $\Delta\beta$). It is not possible to proceed as in §7.1.1 since it has been found that the minimum of reflection with respect to the coupling length does not correspond to the minimum relative to the wavelength.

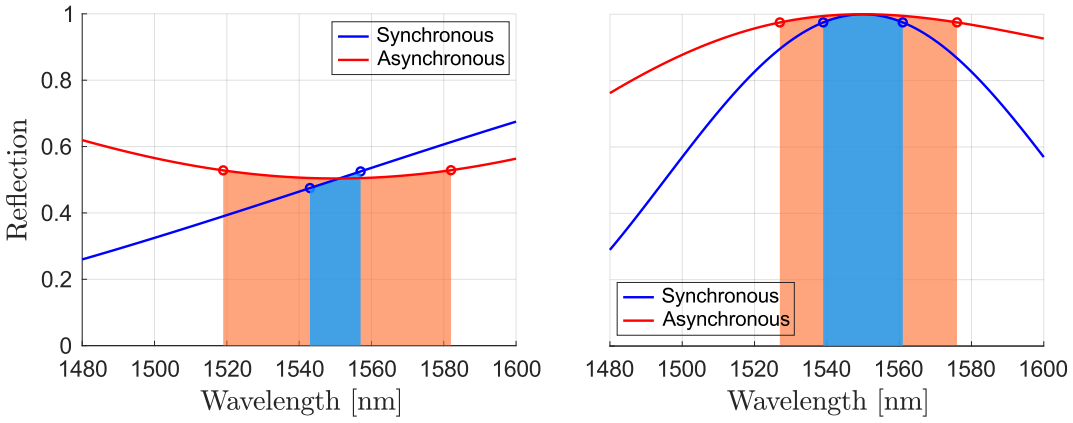

(a) 50:50 directional couplers at $\lambda_0 = 1550$ nm.

(b) 100:0 directional couplers at $\lambda_0 = 1550$ nm.

Figure 7.6: Comparison between the simulations of synchronous and asynchronous directional couplers. Two characteristic situations are shown. In all the cases, the bandwidth is also highlighted.

A trial-and-error process has been carried out in order to find the optimal $\Delta\beta$ and L_c allowing for

$$R(L_c, \Delta\beta, \lambda_0) = T(L_c, \Delta\beta, \lambda_0) = 0.5 \tag{7.11}$$

This condition is satisfied for $\Delta\beta = 18.89$ cm^{-1} and $L_c = 1.34$ mm. The wavelength dependence of such device is shown in Fig. 7.6a, red curve. The bandwidth is 63 nm (from 1519 nm to 1582 nm).

A similar procedure has been followed for the second characteristic point, i.e. the 100:0 coupler. For the synchronous case, the requirement is

$$R(L_c, \lambda_0) = 1 \tag{7.12}$$

where $\lambda_0 = 1550$ nm. This condition is satisfied for

$$L_c = \Lambda^s = \frac{\pi}{\kappa(\lambda_0)} \tag{7.13}$$

It should be noticed that the coupling length obtained in the simulation is quite different from the length required to build a real device. Indeed, the theoretical description does not take into account the mode coupling outside the coupling region. In other words, when dealing with the coupler fabrication, the length has to be re-optimized.

The wavelength dependence of this coupler is shown in Fig. 7.6b, blue curve. The bandwidth is 22 nm (from 1539 nm to 1561 nm).

For the 100:0 asynchronous coupler, the detuning $\Delta\beta$ is already known, since it has been optimized in the previous discussion. Then L_c is not necessarily the double of the coupling length used above, since the two minima (relative to the wavelength or the length) do not coincide. Therefore, for the simulation it has been used

$$L_c = \Lambda^a = \frac{\pi}{\sqrt{k(\lambda_0)^2 + \Delta\beta^2}} \tag{7.14}$$

For this device, the wavelength behavior is shown in Fig. 7.6b, red curve. The bandwidth is 49 nm (from 1527 nm to 1576 nm). Notice that in both cases (50:50 and 100:0) the asynchronous response is more flat than the synchronous one. Therefore, an asynchronous coupler ensures not only a higher stability to coupling length variations, but also to input wavelength variations.

This results have now to be confirmed by experiments. This will be done in the following section.

7.3 Experimental Procedure

In order to experimentally observe the bandwidth difference between synchronous and asynchronous couplers, a deeper study on the κ and $\Delta\beta$ values is required.

Concerning the former, three sets of synchronous directional coupler have been fabricated. The fabrication parameters used and the coupler geometry are the same as in § 7.2.1. Only the writing speed is changed: 35, 40 and 47.5 mm/s have been used in the three sets, respectively.

The acquired data have been analyzed and the coupling coefficient extracted. In the first set $\kappa = 10.71$ cm^{-1}; in the second $\kappa = 10.28$ cm^{-1} (represented in Fig. 7.3) and in the third one $\kappa = 10.78$ cm^{-1}. The latter is represented in Fig. 7.7.

7.3.1 Detuning Analysis

The detuning parameter $\Delta\beta$ has not been addressed yet: it is necessary to study to which extent it can be controlled during the fabrication process. In order to induce a non-zero detuning, the two coupler waveguides should have different propagation constant, i.e. $\beta_1 \neq \beta_2$. This can be achieved by fabricating two waveguides with different refractive index contrast Δn_i with respect to the substrate.

In order to produce two Δn_i, the waveguides can be written with different fabrication parameters. The simplest way is to change the writing speed [79]. Indeed, it is the most reproducible parameter since it is controlled by the software. Moreover, the writing speed does not affect the waveguide quality as much as the other parameters; notice indeed that the three synchronous coupler studied above have very similar values of κ despite the big change in the writing speed.

A series of directional couplers have been fabricated, keeping fixed the writing speed of the first arm at $v_1 = 37.5$ mm/s. The speed of the second arm has been

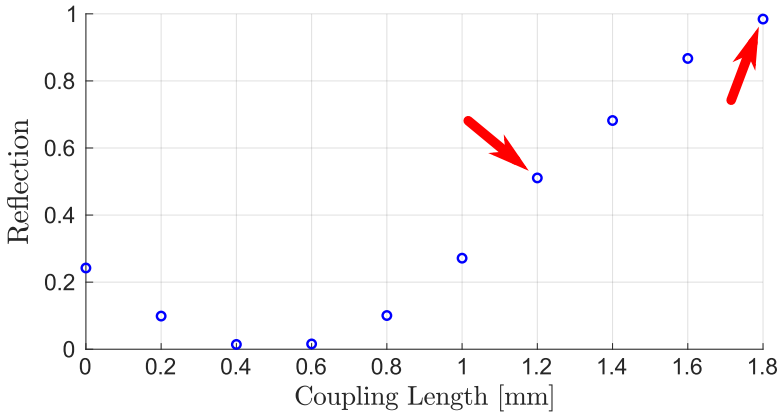

Figure 7.7: Measured reflection for a synchronous directional coupler with writing speed 47.5 mm/s as a function of the coupling length. The wavelength is fixed at 1550 nm. The couplers used for the subsequent discussion are highlighted by red arrows.

changed from 40 mm/s to 50 mm/s. For each set, the coupling length has been changed from $L_c = 0$ mm to $L_c = 1.35$ mm.

The reflection has been measured. Two examples are shown in Fig. 7.8 for Δv = 7.5 mm/s, 12.5 mm/s. By fitting these data, the resulting detuning $\Delta\beta$ are 16.04 cm^{-1} and 31.05 cm^{-1}, respectively.

Notice that the initial phase of the oscillation is unknown. Therefore, a three-parameters (i.e. phase, κ and $\Delta\beta$) fit has to be performed. The more are the degree of freedom and the less precise is the fit: for this reason it has been chosen to fix the κ value for all the fit, in order to decrease to only two the number of parameters. This is reasonable since the coupling coefficient depends weakly on the writing speed. In particular, the value $\kappa = 10.28$ cm $^{-1}$ has been used, corresponding to the synchronous coupler at 40 mm/s.

In Fig. 7.9, the fitted $\Delta\beta$ obtained for all the directional coupler sets have been plotted as a function of the corresponding Δv. Within the writing speed range used, the relation is linear with the following functional form

$$\Delta\beta = (2.83\ \text{s}\,\text{mm}^{-1}\text{cm}^{-1})\,\Delta v - 4.66\ \text{cm}^{-1} \tag{7.15}$$

where Δv is measured in mm/s and $\Delta\beta$ in cm^{-1}. With this experimental relation, a desired $\Delta\beta$ can be induced employing the corresponding Δv.

Notice that Eq. 7.15 is no more reliable near $\Delta\beta \simeq 0$ cm^{-1}. Indeed, when the speed contrast Δv is too low, the fit for the asynchronous couplers does not produce anymore precise values.

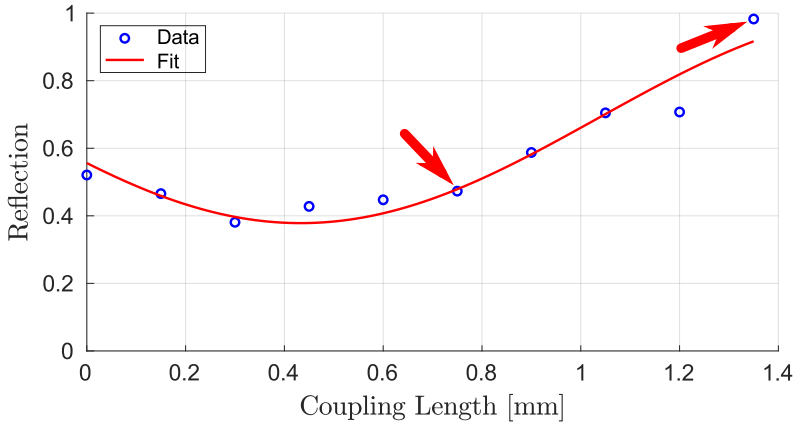

(a) $\Delta v = 7.5$ mm/s; $\Delta\beta = 16.04$ cm^{-1}.

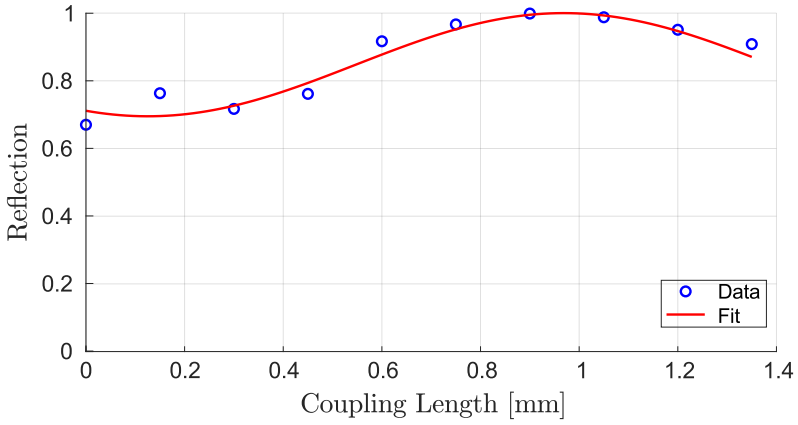

(b) $\Delta v = 12.5$ mm/s; $\Delta\beta = 31.05$ cm^{-1}.

Figure 7.8: Measured reflection for two asynchronous directional couplers as a function of the coupling length. The fit of the data is also shown (red curve). The couplers used in § 7.3.2 are highlighted by red arrows.

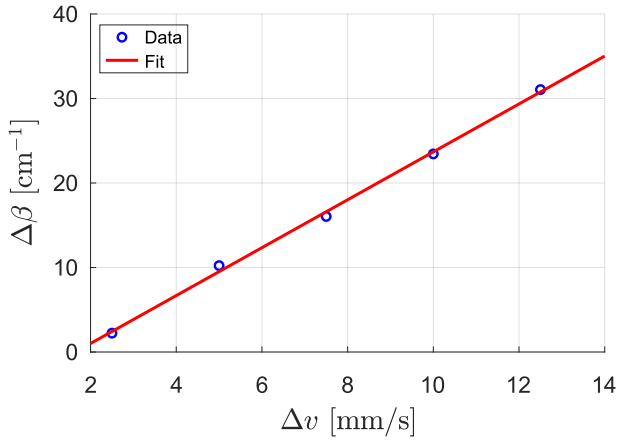

Figure 7.9: Measured data (blue dots) for the detuning $\Delta\beta$ at different speed contrast Δv between the waveguides of a directional coupler. The fit of the data is also shown (red curve).

7.3.2 Experimental Results

Eq. 7.15 can be used to fabricate an asynchronous directional coupler with a desired detuning between the waveguides. It can then be measured at different wavelengths and compared with the corresponding synchronous coupler.

In order to test the validity of the simulations presented in Fig. 7.6, an asynchronous directional coupler with $\Delta\beta \simeq 18.89$ cm^{-1} has to be found. As already explained, the coupling length must be re-optimized experimentally. Once that is done, the corresponding synchronous coupler can be easily fabricated.

Many tests have been carried out, changing the speed contrast and the coupling length in order to reach the desired condition. The device which best resembles the detuning value of 18.89 cm^{-1} is the one represented in Fig. 7.8a. Here, a 50:50 and a 100:0 coupler can be easily found (indicated by red arrows).

The synchronous devices used for the study are represented in Fig. 7.7 by the red arrows. Both arms have been written at a speed of 47.5 mm/s.

All the four directional couplers have been characterized from 1480 nm to 1600 nm and the results are shown in Fig. 7.10. It is clear that in both situations the asynchronous coupler allows for a broader bandwidth. The response is almost flat, which may eventually extend outside the studied wavelength range.

However, notice that the data in Fig. 7.10 resemble the simulations (see Fig. 7.6) only qualitatively. Many are the reasons for this difference. On one side, the simulations have their foundations on a highly-empirical relation, namely Eq. 7.8. On the other hand, the fabrication process possesses some variability, i.e. it is not perfectly reproducible. Future studies should be directed toward a deeper understanding of Eq. 7.15. By improving it, it may be possible to better control the induced $\Delta\beta$ in

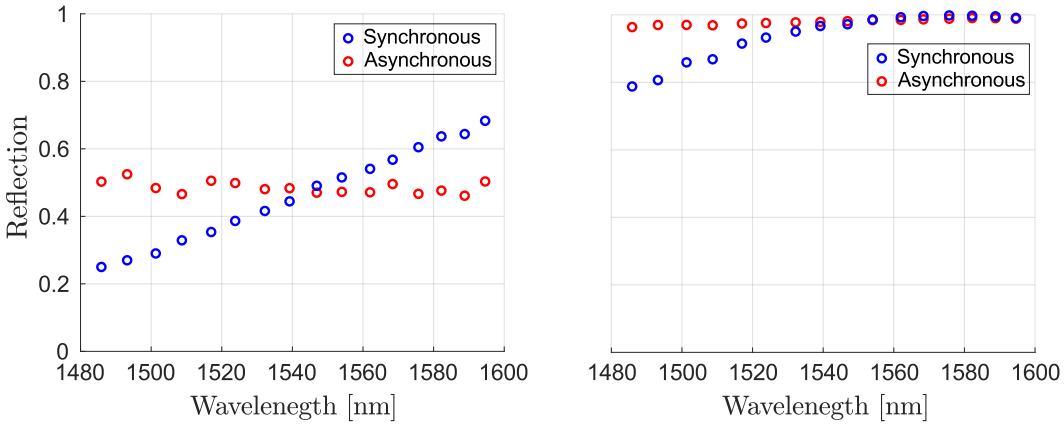

(a) 50:50 directional couplers. **(b)** 100:0 directional couplers.

Figure 7.10: Experimental results for synchronous (blue dots) and asynchronous (red dots) directional couplers with $\kappa = 10.78$ cm^{-1} and $\Delta\beta = 16.04$ cm^{-1}.

order to be able to fabricate the exact device that has been simulated.

Chapter 8

Conclusions and Future Perspectives

In this work, the fabrication and optimization process of an integrated discrete beam combiner has been presented. This device is well suited for astrophotonics, where the interference of the light collected by the telescopes is used to retrieve information about the light intensity distribution of the observed celestial object.

For the fabrication of the interferometer, the femtosecond laser micromachining technique has been employed. In particular, after the inscription process, a thermal annealing step has been performed in order to release the stress accumulated in the glass due to the non-linear interaction with the laser beam. This allowed a reduction of the waveguides birefringence, thus achieving a polarization insensitive behavior of the device. This is a crucial aspect since the celestial light is unpolarized, therefore the device should have the same behavior independently of the input light polarization. Moreover, it has been possible to reduce the waveguides propagation losses below 0.3 dB/cm, thus ensuring a good device operation.

After an optimization of the evanescent coupling, the final device has been fabricated. In particular, a beam combiner able to perform the interference of up to eight points of the same telescope aperture has been inscribed. In order to couple the light coming from the telescope to the interferometer, a pupil remapper has been fabricated, with a maximum depth of more than 850 μm inside the glass.

The device has been firstly characterized with laser light to validate its coupling properties and its polarization insensitive behavior. After that, the circuit has been interferometrically analyzed in order to find its visibility-to-pixel-matrix and the corresponding condition number. A minimum value of 8 in the astronomical H band has been achieved.

Finally, the device has been tested on sky at the William Herschel Telescope in the Roque de los Muchachos Observatory (Spain), where some stars with known intensity distribution have been observed to validate its operation. Though appearing

very promising, the related data are not presented in the present work since they are still under analysis.

Even though the device complies with the requirements, there are still some issues than should be perfectioned. For example, the low resemblance between the outputs of the two DBCs. This can be improved by studying a new fabrication approach leading to a more uniformity of the waveguides on different depth. A possibility could be to employ water-immersion objectives during fabrication, thus limiting the laser beam aberrations. This procedure has not been possible with the setup presented due to physical constraints on the sample dimension.

Another point of improvement could be to increase the similarity between the measured data and the simulations (what has been called ideal distribution previously). This is a fundamental requirement in order to be able to forecast the main device performances.

In the final chapter, the wavelength response of directional couplers has been studied. It has been showed how an asynchronous coupler is able to widen the bandwidth. The following step could be to apply these results to an array of waveguides. The situation is more complex than what presented here, since many couplings between waveguides have to be taken into account. The recipe to induce a desired detuning has been also addressed. Future studies may help improving it, in order to achieve a more reproducible relation.

Appendix A

Coupled Mode Theory

Consider the Maxwell's equations in absence of sources ($\rho = 0$ and $\boldsymbol{J} = 0$)

$$\nabla \cdot \boldsymbol{E} = 0 \qquad \nabla \cdot \boldsymbol{B} = 0 \qquad \nabla \times \boldsymbol{E} = -\frac{\partial \boldsymbol{B}}{\partial t} \qquad \nabla \times \boldsymbol{B} = \frac{\varepsilon_r}{c^2}\frac{\partial \boldsymbol{E}}{\partial t} \tag{A.1}$$

where the magnetic behavior has been neglected ($\mu_r = 1$). $\boldsymbol{E}$ and $\boldsymbol{B}$ are the electric and magnetic field, respectively.

From Eqs. A.1, the electric field propagation equation can be obtained

$$\nabla^2 \boldsymbol{E} - \frac{\varepsilon_r}{c^2}\frac{\partial^2 \boldsymbol{E}}{\partial t^2} = 0 \tag{A.2}$$

The electric field expression can be simplified with the following ansatz

$$\boldsymbol{E}(x, y, z, t) = \psi(x, y, z)e^{-i\omega t}\hat{\boldsymbol{u}} \tag{A.3}$$

where the time dependence has been taken out from the main function – now a scalar.

Using $k_0 = 2\pi/\lambda = \omega/c$ and $\varepsilon_r = n^2$, Eq. A.2 can be reduced to

$$\nabla_t^2 \psi + \psi'' + k_0^2 n^2(x, y)\psi = 0 \tag{A.4}$$

where the following short notations have also been employed:

$$\nabla_t^2 = \frac{\partial^2}{\partial x^2} + \frac{\partial^2}{\partial y^2} \qquad f' = \frac{\partial f}{\partial z}$$

Eq. A.4 describes the scalar electric field propagation inside a given structure, whose geometry is contained into $n(x, y)$. The z dependence has been dropped down since it has been assumed that the structure has a constant shape along the propagation direction.

The simplest structure is composed by a set of two straight waveguides, one near the other. Light is injected into one of them and the output distribution

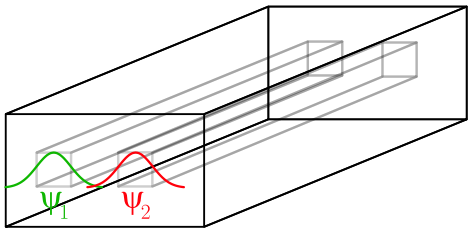

Figure A.1: Graphical representation of two square-cross section waveguides fabricated inside a substrate. The guided modes are highlighted in green (ψ_1) and red (ψ_2). A small overlap of the mode tails is visible, which ensures the coupling.

is collected. The purpose of this chapter is to characterize theoretically the light propagation inside the structure.

In the following, both waveguides are assumed to be single-moded [40]. Each of them guides its own mode, which can be described as

$$\psi_i(x, y, x) = \psi_i(x, y)e^{-i\beta_i z} \tag{A.5}$$

with β_i the propagation constant of the i-th mode. A graphical representation of the system is shown in Fig. A.1.

The mode in a waveguide is not strictly confined to its core. Extending outside the waveguide, there is an evanescent electric field. If two guides are placed sufficiently close to each other, these evanescent fields can overlap spatially. This causes an energy exchange between them.

If the mode overlap is big, the situation is very difficult to treat analytically. However, if the waveguides are not too close to each other (but still close enough to ensure some overlap), it is possible to describe the coupling treating each mode separately. This is called *coupled mode approximation* [40].

Under this assumption, the solution of Eq. A.4 can be written as a linear combination of the two single modes (see Eq. A.5):

$$\psi(x, y, z) = A_1(z)\psi_1(x, y)e^{-i\beta_1 z} + A_2(z)\psi_2(x, y)e^{-i\beta_2 z} \tag{A.6}$$

where $A_i(z)$ are the local amplitudes of the two modes. They vary with the propagation distance z due to the energy exchange between the modes. The transverse field $\psi_i(x, y)$ is assumed constant with the propagation distance.

By substituting Eq. A.6 into Eq. A.4, it is possible to get

$$\begin{aligned}\nabla_t^2\psi_1 A_1 e^{-i\beta_1 z} + A_1''\psi_1 e^{-i\beta_1 z} - 2i\beta_1 A_1'\psi_1 e^{-i\beta_1 z} - \beta_1^2 A_1\psi_1 e^{-i\beta_1 z} + \\ + k_0^2\left[n_1^2 + \Delta n_1^2\right] A_1\psi_1 e^{-i\beta_1 z} + (same\ for\ 2) = 0\end{aligned}$$

Notice that Δn_1^2 is a perturbation to the first waveguide introduced by the second one. The opposite holds for Δn_2^2.

The first, fourth and fifth terms (for both ψ_1 and ψ_2) represent the wave equation for a single waveguide, that is when $n(x,y) = n_1$ and $A_1(z) = const$:

$$\nabla_t^2 \psi_1 A_1 e^{-i\beta_1 z} - \beta_1^2 A_1 \psi_1 e^{-i\beta_1 z} + k_0^2 n_1^2 A_1 \psi_1 e^{-i\beta_1 z} = 0$$

Moreover, in the weakly coupling approximation, the second derivative A'' can be neglected with respect to the first one A'. Therefore:

$$-2i\beta_1 A_1' \psi_1 - 2i\beta_2 A_2' \psi_2 e^{i\Delta\beta z} + k_0^2 \Delta n_1^2 A_1 \psi_1 + k_0^2 \Delta n_2^2 A_2 \psi_2 e^{i\Delta\beta z} = 0 \tag{A.7}$$

where $\Delta\beta = \beta_1 - \beta_2$ is the mismatch between the modes propagation constants.

Multiplying Eq. A.7 by ψ_1^* and integrating over the transverse plane, it can be modified as

$$\begin{aligned} -2i\beta_1 A_1' \iint_{-\infty}^{\infty} \psi_1 \psi_1^* \mathrm{d}x\mathrm{d}y - 2i\beta_2 A_2' e^{i\Delta\beta z} \iint_{-\infty}^{\infty} \psi_2 \psi_1^* \mathrm{d}x\mathrm{d}y + \\ + k_0^2 A_1 \iint_{-\infty}^{\infty} \psi_1 \Delta n_1^2 \psi_1^* \mathrm{d}x\mathrm{d}y + k_0^2 A_2 e^{i\Delta\beta z} \iint_{-\infty}^{\infty} \psi_2 \Delta n_1^2 \psi_1^* \mathrm{d}x\mathrm{d}y = 0 \end{aligned}$$

The second term can be neglected, since the overlap between ψ_1 and ψ_2 is negligible in the weak coupling approximation. This is because the waveguides are not too close to each other.

Defining the *coupling coefficients* $\kappa_{n,m}$ as

$$\kappa_{n,m} = \frac{k_0^2}{2\beta_n} \frac{\iint \psi_m \Delta n_m^2 \psi_n^* \mathrm{d}x\mathrm{d}y}{\iint \psi_m \psi_n^* \mathrm{d}x\mathrm{d}y} \tag{A.8}$$

and repeating the multiplication of Eq. A.7 by ψ_2^*, it is possible to obtain the following system of equations, called *coupled mode equations*:

$$\begin{cases} iA_1' = \kappa_{1,1} A_1 + \kappa_{1,2} A_2 e^{i\Delta\beta z} \\ iA_2' = \kappa_{2,1} A_1 e^{-i\Delta\beta z} + \kappa_{2,2} A_2 \end{cases} \tag{A.9}$$

However, as can be seen from Eq. A.8, $\kappa_{1,1}$ and $\kappa_{2,2}$ can be neglected. Indeed, Δn_1^2 is non-zero only on the second waveguide, where ψ_1 is small. These equations can then be rewritten as

$$\begin{cases} iA_1' = \kappa_{1,2} A_2 e^{i\Delta\beta z} \\ iA_2' = \kappa_{2,1} A_1 e^{-i\Delta\beta z} \end{cases} \tag{A.10}$$

These equations imply that variations in the amplitude of the first mode are linked to the amplitude of the second one, through $\kappa_{1,2}$, and vice-versa. The modes are coupled together, exchanging energy through the coupling coefficients.

It can be assumed, due to the symmetry of the device that $\kappa_{1,2} \simeq \kappa_{2,1} = \kappa$ [40]. It is now possible to analytically solve the system A.10.

It is common use to describe the mode coupling in terms of power, instead of amplitude. Being both values normalized, the connection between them is simply $P_i(z) = |A_i(z)|^2$.

Assuming light is injected only in the first waveguide: $P_1(0) = 1$ and $P_2(0) = 0$. It can be showed that the normalized power propagation in the two waveguides, as a function of z, can be described as [40]:

$$\begin{cases} P_1(z) = \cos^2(\sigma z) + \dfrac{\delta^2}{\delta^2 + \kappa^2} \sin^2(\sigma z) \\ P_2(z) = \dfrac{\kappa^2}{\delta^2 + \kappa^2} \sin^2(\sigma z) \end{cases} \tag{A.11}$$

where $\sigma = \sqrt{\delta^2 + \kappa^2}$ and $\delta = \Delta\beta/2$.

Since the mode amplitudes are normalized: $0 < P_i(z) < 1$ and $P_1(z)+P_2(z) = 1$.

Appendix B

Gaussian Beam Propagation

In many applications, the laser beam intensity profile is assumed to follow a gaussian distribution. It is a mathematical description to simply the problem, which well resembles the reality in many situations.

The intensity profile decreases as the radial distance from the beam center increases, on the plane perpendicular to the beam propagation direction. This distribution is described as

$$I(r) = I_0 e^{-\frac{2r^2}{w(z)^2}} \tag{B.1}$$

where I_0 is the peak intensity, r the radial distance from the beam center and z the propagation direction. $w(z)$ is the beam radius where $I(r) = (1/e^2)I_0$, as can be seen from Fig. B.1.

The intensity profile changes with propagation. The beam converges towards (and diverges afterwards) $w_z = w(z_R)$, called *beam waist*. This is the region where the beam radius is at its minimum.

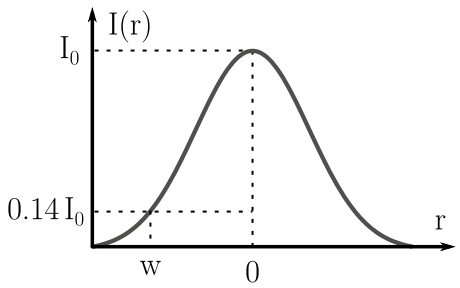

Figure B.1: Gaussian beam intensity as a function of the radial distance from the beam center. w is the beam radius where $I(r) = 0.14I_0$, I_0 being the peak intensity.

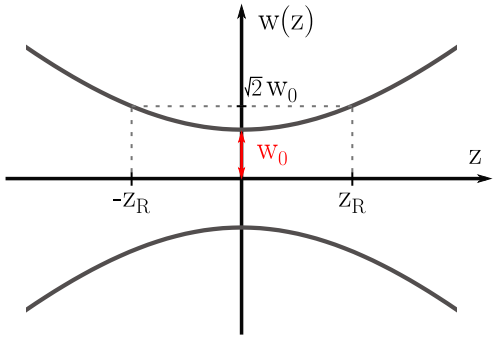

Figure B.2: Gaussian beam width $w(z)$ as a function of propagation distance. The beam waist w_0 is highlighted. Notice that $w(z_R) = \sqrt{2}w_0$.

The propagation of $w(z)$ through space can be described with [80]:

$$w(z) = w_0\sqrt{1 + \left(\frac{z}{z_R}\right)^2} \tag{B.2}$$

where $z_R = \dfrac{\pi w_0^2}{\lambda}$ is called *Rayleigh range* of the gaussian beam. Notice that z_R is the z coordinate where the cross-sectional area of the beam is doubled with respect to the one at the beam waist. In other words, $w(z_R) = \sqrt{2}w_0$ as in Fig. B.2

A real laser beam has some deviations from the ideal gaussian profile. The quality of a laser beam is defined as the amount of similarity with an ideal gaussian beam. It mathematically described by the M^2 *factor*, defined as [81]:

$$M^2 = \frac{\pi w_0 \theta}{\lambda} \tag{B.3}$$

where θ is the beam divergence. Notice that for a gaussian beam $\theta = \lambda/\pi w_0$, so that $M^2 = 1$. A real laser beam has $M^2 > 1$.

It can be showed that, for a real laser beam focused into a material with refractive index n, the beam waist w_0 can be computed as [46]:

$$w_0 = \frac{M^2\lambda}{\pi NA} \tag{B.4}$$

in the paraxial approximation. On the other hand, the Rayleigh range is

$$z_R = \frac{M^2\lambda n}{\pi NA^2} \tag{B.5}$$

Notice that the ratio between the Rayleigh range and the beam waist is

$$\frac{z_R}{w_0} = \frac{n}{NA} \tag{B.6}$$

Bibliography

[1] F. Malbet, P. Kern, I. Schanen-Duport, J. Berger, and K. Perraut, "Integrated optics for astronomical interferometry. I. Concept and astronomical applications," *Astron. Astrophys. Supplement Series*, vol. 138, 07 1999.

[2] P. R. Lawson, *Principles of Long Baseline Stellar Interferometry*. JPL, 1999.

[3] R. N. Bracewell, "Detecting nonsolar planets by spinning infrared interferometer," pp. 780 – 781, Aug 1978. [Online]. Available: https://doi.org/10.1038/274780a0

[4] B. Mennesson, M. Ollivier, and C. Ruilier, "Use of single-mode waveguides to correct the optical defects of a nulling interferometer," *J. Opt. Soc. Am. A*, vol. 19, no. 3, pp. 596–602, Mar 2002. [Online]. Available: http://josaa.osa.org/abstract.cfm?URI=josaa-19-3-596

[5] T. Lagadec, B. Norris, S. Gross, A. Arriola, T. Gretzinger, N. Cvetojevic, J. Lawrence, M. Withford, and P. Tuthill, "GLINT South: a photonic nulling interferometer pathfinder at the Anglo-Australian Telescope for high contrast imaging of substellar companions," in *Optical and Infrared Interferometry and Imaging VI*, M. J. Creech-Eakman, P. G. Tuthill, and A. Mérand, Eds., vol. 10701, International Society for Optics and Photonics. SPIE, 2018, pp. 238 – 245. [Online]. Available: https://doi.org/10.1117/12.2313171

[6] J. Bland-Hawthorn, S. Ellis, S. Leon-Saval, R. Haynes, M. Roth, H.-G. Löhmannsröben, A. Horton, T. Cuby, J.-G. Birks, J. Lawrence, P. Gillingham, S. Ryder, and C. Trinh, "A complex multi-notch astronomical filter to suppress the bright infrared sky," *Nat. Commun.*, vol. 581, no. 2, Dec 2011. [Online]. Available: https://doi.org/10.1038/ncomms1584

[7] B. Norris and J. Bland-Hawthorn, "Astrophotonics: The Rise of Integrated Photonics in Astronomy," *Optics and Photonics News*, vol. 30, no. 5, pp. 26 – 33, May 2019. [Online]. Available: http://dx.doi.org/10.1364/OPN.30.5.000026

[8] T. Mizunami, T. V. Djambova, T. Niiho, and S. Gupta, "Bragg gratings in multimode and few-mode optical fibers," *J. Light. Technol.*, vol. 18, no. 2, pp. 230–235, Feb 2000.

[9] L.-S. S. G., A. Alexander, and B.-H. Joss, "Photonic lanterns," *Nanoph.*, vol. 2, pp. 429 – 440, 2013. [Online]. Available: https://www.degruyter.com/view/j/nanoph.2013.2.issue-5-6/nanoph-2013-0035/nanoph-2013-0035.xml

[10] S. G. Leon-Saval, T. A. Birks, J. Bland-Hawthorn, and M. Englund, "Multimode fiber devices with single-mode performance," *Opt. Lett.*, vol. 30, no. 19, pp. 2545–2547, Oct 2005. [Online]. Available: http://ol.osa.org/abstract.cfm?URI=ol-30-19-2545

[11] C. Trinh, S. Ellis, J. Bland-Hawthorn, J. Lawrence, A. Horton, S. Leon-Saval, K. Shortridge, J. Bryant, S. Case, M. Colless, W. Couch, K. Freeman, H.-G. Loehmannsroeben, L. Gers, K. Glazebrook, R. Haynes, S. Lee, J. O'Byrne, S. Miziarski, and J. Zheng, "Gnosis: the first instrument to use fibre bragg gratings for oh suppression," *Astron. J.*, vol. 145, p. 51, 02 2013.

[12] R. R. Thomson, T. A. Birks, S. G. Leon-Saval, A. K. Kar, and J. Bland-Hawthorn, "Ultrafast laser inscription of an integrated photonic lantern," *Opt. Express*, vol. 19, no. 6, pp. 5698–5705, Mar 2011. [Online]. Available: http://www.opticsexpress.org/abstract.cfm?URI=oe-19-6-5698

[13] J. Bland-Hawthorn, J. Lawrence, G. Robertson, S. Campbell, B. Pope, C. Betters, S. Leon-Saval, T. Birks, R. Haynes, N. Cvetojevic, and N. Jovanovic, "PIMMS: Photonic integrated multimode microspectrograph," *Proc SPIE*, vol. 7735, 07 2010.

[14] C. Betters, S. Leon-Saval, J. Robertson, and J. Bland-Hawthorn, "Beating the classical limit: A diffraction-limited spectrograph for an arbitrary input beam," *Opt. express*, vol. 21, pp. 26 103–12, 11 2013.

[15] N. Cvetojevic, N. Jovanovic, C. Betters, J. S. Lawrence, S. C. Ellis, G. Robertson, and J. Bland-Hawthorn, "First starlight spectrum captured using an integrated photonic micro-spectrograph," *Astron. Astrophys.*, vol. 544, p. L1, Jul 2012. [Online]. Available: http://dx.doi.org/10.1051/0004-6361/201219116

[16] J. Bland-Hawthorn and S. G. Leon-Saval, "Astrophotonics: molding the flow of light in astronomical instruments," *Opt. Express*, vol. 25, no. 13, pp. 15 549–15 557, Jun 2017. [Online]. Available: http://www.opticsexpress.org/abstract.cfm?URI=oe-25-13-15549

[17] J.-T. Gomes, L. Delage, R. Baudoin, L. Grossard, L. Bouyeron, D. Ceus, F. Reynaud, H. Herrmann, and W. Sohler, "Laboratory demonstration of spatial-coherence analysis of a blackbody through an up-conversion interferometer," *Phys. Rev. Lett*, vol. 112, p. 143904, 04 2014.

[18] L. Szemendera, P. Darré, R. Baudoin, L. Grossard, L. Delage, H. Herrmann, C. Silberhorn, and F. Reynaud, "In-lab ALOHA mid-infrared up-conversion interferometer with high fringe contrast @$\lambda = 3.39$ µm," *Mon. Notices Royal Astron. Soc*, vol. 457, pp. 3115–3118, 04 2016.

[19] P. Darré, R. Baudoin, J.-T. Gomes, N. Scott, L. Delage, L. Grossard, J. Sturmann, C. Farrington, F. Reynaud, and T. Brummelaar, "First on-sky fringes with an up-conversion interferometer tested on a telescope array," *Phys. Rev. Lett*, vol. 117, 11 2016.

[20] The Event Horizon Collaboration, "First M87 Event Horizon Telescope Results. I. The Shadow of the Supermassive Black Hole," *Astrophys. J*, vol. 875, pp. L1 – L17, Apr 2019. [Online]. Available: https://iopscience.iop.org/article/10.3847/2041-8213/ab0ec7

[21] S. Minardi, S. Lacour, J.-P. Berger, L. Labadie, R. Thomson, C. Haniff, and M. Ireland, "Beam combination schemes and technologies for the planet formation imager," 08 2016, p. 99071N.

[22] R. Diener, S. Minardi, J. Tepper, S. Nolte, and L. Labadie, "All-in-one 4-telescope beam combination with a zig-zag array of waveguides," vol. 9907, 2016. [Online]. Available: https://doi.org/10.1117/12.2232290

[23] N. Jovanovic, P. G. Tuthill, B. Norris, S. Gross, P. Stewart, N. Charles, S. Lacour, M. Ams, J. S. Lawrence, A. Lehmann, C. Niel, J. G. Robertson, G. D. Marshall, M. Ireland, A. Fuerbach, and M. J. Withford, "Starlight demonstration of the Dragonfly instrument: an integrated photonic pupil-remapping interferometer for high-contrast imaging," *Mon. Notices Royal Astron. Soc.*, vol. 427, no. 1, pp. 806–815, 11 2012. [Online]. Available: https://doi.org/10.1111/j.1365-2966.2012.21997.x

[24] M. Benisty, J. Berger, L. Jocou, P. Labeye, F. Malbet, K. Perraut, and P. Kern, "An integrated optics beam combiner for the second generation vlti instruments," *Astron. Astrophys.*, vol. 498, 03 2009.

[25] A. Glindemann, *Principles of Stellar Interferometry*, ser. Astronomy and Astrophysics Library. Springer, 2011.

[26] M. Shao and D. H. Staelin, "Long- baseline optical interferometer for astrometry," *J. Opt. Soc. Am.*, vol. 67, no. 1, pp. 81–86, Jan 1977. [Online]. Available: http://www.osapublishing.org/abstract.cfm?URI=josa-67-1-81

[27] GRAVITY Collaboration, "First light for GRAVITY: Phase referencing optical interferometry for the Very Large Telescope Interferometer," *Astron. Astrophys.*, vol. 602, p. A94, 2017. [Online]. Available: https://doi.org/10.1051/0004-6361/201730838

[28] S. Minardi, "Photonic lattices for astronomical interferometry," *Mon. Notices Royal Astron. Soc.*, vol. 422, no. 3, pp. 2656–2660, May 2011. [Online]. Available: https://doi.org/10.1111/j.1365-2966.2012.20832.x

[29] R. Diener, J. Tepper, L. Labadie, T. Pertsch, S. Nolte, and S. Minardi, "Towards 3D-photonic, multi-telescope beam combiners for mid-infrared astrointerferometry," *Opt. Express*, vol. 25, no. 16, pp. 19 262–19 274, Aug 2017. [Online]. Available: http://www.opticsexpress.org/abstract.cfm?URI=oe-25-16-19262

[30] M. Born and E. Wolf, "Interference and diffraction with partrially coherent light," in *Principles of Optics (Sixth Edition)*. Pergamon, 1980, ch. 10, pp. 491–555.

[31] J. W. Goodman, *Introduction to Fourier Optics*. McGraw-Hill, 1996.

[32] D. Segransan, "Observability and uv coverage," *EAS Publications Series*, vol. 6, pp. 69 – 69, 01 2003.

[33] L. A. Thompson, "Adaptive optics in astronomy," *Physics Today*, vol. 47, no. 12, Dec 1994.

[34] C. A. Primmerman, D. V. Murphy, D. A. Page, B. G. Zollars, and H. T. Barclay, "Compensation of atmospheric optical distortion using a synthetic beacon," pp. 141 – 143, Sep 1991. [Online]. Available: https://doi.org/10.1038/353141a0

[35] R. Foy and A. Labeyrie, "Feasibility of adaptive telescope with laser probe," pp. L29 – L31, Nov 1985.

[36] J. E. Baldwin, C. A. Haniff, C. D. Mackay, and P. J. Warner, "Closure phase in high-resolution optical imaging," *Nature*, vol. 320, pp. 595 – 597, Apr 1986. [Online]. Available: https://doi.org/10.1038/320595a0

[37] A. C. S. Readhead, T. S. Nakajima, T. J. Pearson, G. Neugebauer, J. B. Oke, and W. L. W. Sargent, "Diffraction-Limited Imaging with Ground-Based Optical Telescopes," *Astron. J*, vol. 52, no. 4, pp. 1278 – 1296, Apr 1988. [Online]. Available: https://ui.adsabs.harvard.edu/abs/1988AJ.....95.1278R/abstract

[38] J. D. Monnier, "Optical interferometry in astronomy," *Rep. Prog. Phys*, vol. 66, no. 5, pp. 789–857, Apr 2003. [Online]. Available: https://doi.org/10.1088%2F0034-4885%2F66%2F5%2F203

[39] S. Minardi, F. Dreisow, M. Gräfe, S. Nolte, and T. Pertsch, "Three-dimensional photonic component for multichannel coherence measurements,"

Opt. Lett., vol. 37, no. 15, pp. 3030–3032, Aug 2012. [Online]. Available: http://ol.osa.org/abstract.cfm?URI=ol-37-15-3030

[40] R. R. A. Syms and J. R. Cozens, "Coupled Mode Devices," in *Optical Guided Waves and Devices*. McGraw-Hill, 1992, ch. 10, pp. 1–31.

[41] S. Minardi, "Nonlocality of coupling and the retrieval of field correlations with arrays of waveguides," *Phys. Rev. A*, vol. 92, p. 013804, Jul 2015. [Online]. Available: https://link.aps.org/doi/10.1103/PhysRevA.92.013804

[42] S. Minardi and T. Pertsch, "Interferometric beam combination with discrete optics," *Opt. Lett.*, vol. 35, no. 18, pp. 3009–3011, Sep 2010. [Online]. Available: http://ol.osa.org/abstract.cfm?URI=ol-35-18-3009

[43] E. W. Weisstein, *Moore-Penrose Matrix Inverse*. From *MathWorld*–A Wolfram Web Resource. [Online]. Available: http://mathworld.wolfram.com/Moore-PenroseMatrixInverse.html

[44] D. A. Belsley, E. Kuh, and R. E. Welsch, *Regression Diagnostics*. Wiley, 1980.

[45] R. Errmann and S. Minardi, "6- and 8-telescope discrete beam combiners," in *Optical and Infrared Interferometry and Imaging V*, F. Malbet, M. J. Creech-Eakman, and P. G. Tuthill, Eds., vol. 9907, International Society for Optics and Photonics. SPIE, 2016, pp. 730 – 737. [Online]. Available: https://doi.org/10.1117/12.2232329

[46] S. M. Eaton, G. Cerullo, and R. Osellame, "Fundamentals of Femtosecond Laser Modification of Bulk Dielectrics," in *Femtosecond Laser Micromachining*, R. Osellame, G. Cerullo, and R. Ramponi, Eds. Springer, 2012, ch. 1, pp. 3–18.

[47] K. M. Davis, K. Miura, N. Sugimoto, and K. Hirao, "Writing Waveguides in Glass with a Femtosecond Laser," *Opt. Lett.*, vol. 21, no. 21, pp. 1729–1731, Nov 1996. [Online]. Available: http://ol.osa.org/abstract.cfm?URI=ol-21-21-1729

[48] A. Marcinkevičius, S. Juodkazis, M. Watanabe, M. Miwa, S. Matsuo, H. Misawa, and J. Nishii, "Femtosecond laser-assisted three-dimensional microfabrication in silica," *Opt. Lett.*, vol. 26, no. 5, pp. 277–279, Mar 2001. [Online]. Available: http://ol.osa.org/abstract.cfm?URI=ol-26-5-277

[49] C. B. Schaffer, A. Brodeur, and E. Mazur, "Laser-induced breakdown and damage in bulk transparent materials induced by tightly focused femtosecond laser pulses," *Meas. Sci. Technol.*, vol. 12, no. 11, pp. 1784–1794, Oct 2001. [Online]. Available: https://iopscience.iop.org/article/10.1088/0957-0233/12/11/305

[50] L. V. Keldysh, "Ionization in the Field of a Strong Electromagnetic Wave," *Sov. Phys. JETP*, vol. 20, no. 5, pp. 1945–1957, May 1965.

[51] A. M. Streltsov and N. F. Borrelli, "Study of femtosecond-laser-written waveguides in glasses," *J. Opt. Soc. Am. B*, vol. 19, no. 10, pp. 2496–2504, Oct 2002. [Online]. Available: http://josab.osa.org/abstract.cfm?URI=josab-19-10-2496

[52] A. Kaiser, B. Rethfeld, M. Vicanek, and G. Simon, "Microscopic processes in dielectrics under irradiation by subpicosecond laser pulses," *Phys. Rev. B*, vol. 61, pp. 11 437–11 450, May 2000. [Online]. Available: https://link.aps.org/doi/10.1103/PhysRevB.61.11437

[53] R. R. Gattass and E. Mazur, "Femtosecond laser micromachining in transparent materials," *Nat. Photonics*, vol. 2, pp. 219–225, Apr 2008. [Online]. Available: https://doi.org/10.1038/nphoton.2008.47

[54] R. Osellame, G. Della Valle, N. Chiodo, S. Taccheo, P. Laporta, O. Svelto, and G. Cerullo, "Lasing in femtosecond laser written optical waveguides," *Appl. Phys. A*, vol. 93, pp. 17–26, 10 2008.

[55] B. C. Stuart, M. D. Feit, S. Herman, A. M. Rubenchik, B. W. Shore, and M. D. Perry, "Nanosecond-to-femtosecond laser-induced breakdown in dielectrics," *Phys. Rev. B*, vol. 53, pp. 1749–1761, Jan 1996. [Online]. Available: https://link.aps.org/doi/10.1103/PhysRevB.53.1749

[56] M. H. Niemz, "Threshold dependence of laser-induced optical breakdown on pulse duration," *Appl. Phys. Lett.*, vol. 66, pp. 1181–1183, Mar. 1995.

[57] M. Lenzner, J. Krüger, S. Sartania, Z. Cheng, C. Spielmann, G. Mourou, W. Kautek, and F. Krausz, "Femtosecond Optical Breakdown in Dielectrics," *Phys. Rev. Lett.*, vol. 80, pp. 4076–4079, May 1998. [Online]. Available: https://link.aps.org/doi/10.1103/PhysRevLett.80.4076

[58] J. W. Chan, T. Huser, S. Risbud, and D. M. Krol, "Structural changes in fused silica after exposure to focused femtosecond laser pulses," *Opt. Lett.*, vol. 26, no. 21, pp. 1726–1728, Nov 2001. [Online]. Available: http://ol.osa.org/abstract.cfm?URI=ol-26-21-1726

[59] S. M. Eaton, H. Zhang, M. L. Ng, S. Ho, and P. R. Herman, "Optimization of repetition rate, pulse duration, and polarization for femtosecond-laser-writing of waveguides in borosilicate and fused silica glasses," *CLEO/Europe and IQEC 2007 Conference Digest*, 2007.

[60] D. Homoelle, S. Wielandy, A. L. Gaeta, N. F. Borrelli, and C. Smith, "Infrared photosensitivity in silica glasses exposed to femtosecond laser pulses," *Opt. Lett.*, vol. 24, no. 18, pp. 1311–1313, Sep 1999. [Online]. Available: http://ol.osa.org/abstract.cfm?URI=ol-24-18-1311

[61] K. Itoh, W. Watanabe, S. Nolte, and C. B. Schaffer, "Ultrafast Processes for Bulk Modification of Transparent Materials," *MRS Bulletin*, vol. 31, no. 8, p. 620–625, 2006.

[62] R. R. Thomson, N. D. Psaila, H. T. Bookey, D. T. Reid, and A. K. Kar, "Controlling the Cross-section of Ultrafast Laser Inscribed Optical Waveguides," in *Femtosecond Laser Micromachining*, R. Osellame, G. Cerullo, and R. Ramponi, Eds. Springer, 2012, ch. 5, pp. 93–125.

[63] G. Cerullo, R. Osellame, S. Taccheo, M. Marangoni, D. Polli, R. Ramponi, P. Laporta, and S. D. Silvestri, "Femtosecond micromachining of symmetric waveguides at 1.5 um by astigmatic beam focusing," *Opt. Lett.*, vol. 27, no. 21, pp. 1938–1940, Nov 2002. [Online]. Available: http://ol.osa.org/abstract.cfm?URI=ol-27-21-1938

[64] M. Shimizu, M. Sakakura, M. Ohnishi, Y. Shimotsuma, T. Nakaya, K. Miura, and K. Hirao, "Mechanism of heat-modification inside a glass after irradiation with high-repetition rate femtosecond laser pulses," *J. Appl. Phys.*, vol. 108, no. 7, p. 073533, 2010. [Online]. Available: https://doi.org/10.1063/1.3483238

[65] S. M. Eaton and P. R. Herman, "Passive Photonic Devices in Glass," in *Femtosecond Laser Micromachining*, R. Osellame, G. Cerullo, and R. Ramponi, Eds. Springer, 2012, ch. 7, pp. 155–195.

[66] S. M. Eaton, H. Zhang, P. R. Herman, F. Yoshino, L. Shah, J. Bovatsek, and A. Y. Arai, "Heat accumulation effects in femtosecond laser-written waveguides with variable repetition rate," *Opt. Express*, vol. 13, no. 12, pp. 4708–4716, Jun 2005. [Online]. Available: http://www.opticsexpress.org/abstract.cfm?URI=oe-13-12-4708

[67] M. S. Eaton, "Contrasts in Thermal Diffusion and Heat Accumulation Effects in the Fabrication of Waveguides in Glasses Using Variable Repetition Rate Femtosecond Laser," Ph.D. dissertation, University of Toronto, 2008.

[68] W. Vogel, *Glass Chemistry*. Springer, 1994.

[69] A. Marcinkevičius, V. Mizeikis, and S. Juodkazis, "Effect of refractive index-mismatch on laser microfabrication in silica glass," *Appl. Phys. A*, no. 76, pp. 257–260, 2003. [Online]. Available: https://rd.springer.com/article/10.1007/s00339-002-1447-z

[70] S. M. Eaton, H. Zhang, M. L. Ng, J. Li, W.-J. Chen, S. Ho, and P. R. Herman, "Transition from thermal diffusion to heat accumulation in high repetition rate femtosecond laser writing of buried optical waveguides," *Opt. Express*, vol. 16, no. 13, pp. 9443–9458, Jun 2008. [Online]. Available: http://www.opticsexpress.org/abstract.cfm?URI=oe-16-13-9443

[71] A. Arriola, S. Gross, N. Jovanovic, N. Charles, P. G. Tuthill, S. M. Olaizola, A. Fuerbach, and M. J. Withford, "Low bend loss waveguides enable compact, efficient 3D photonic chips," *Opt. Express*, vol. 21, no. 3, pp. 2978–2986, Feb 2013. [Online]. Available: http://www.opticsexpress.org/abstract.cfm?URI=oe-21-3-2978

[72] N. Charles, N. Jovanovic, S. Gross, P. Stewart, B. Norris, J. O'Byrne, J. S. Lawrence, M. J. Withford, and P. G. Tuthill, "Design of optically path-length-matched, three-dimensional photonic circuits comprising uniquely routed waveguides," *Appl. Opt.*, vol. 51, no. 27, pp. 6489–6497, Sep 2012. [Online]. Available: http://ao.osa.org/abstract.cfm?URI=ao-51-27-6489

[73] G. Corrielli, S. Atzeni, S. Piacentini, I. Pitsios, A. Crespi, and R. Osellame, "Symmetric polarization-insensitive directional couplers fabricated by femtosecond laser writing," *Opt. Express*, vol. 26, no. 12, pp. 15 101–15 109, Jun 2018. [Online]. Available: http://www.opticsexpress.org/abstract.cfm?URI=oe-26-12-15101

[74] R. Osellame, N. Chiodo, G. D. Valle, S. Taccheo, R. Ramponi, G. Cerullo, A. Killi, U. Morgner, M. Lederer, and D. Kopf, "Optical waveguide writing with a diode-pumped femtosecond oscillator," *Opt. Lett.*, vol. 29, no. 16, pp. 1900–1902, Aug 2004. [Online]. Available: http://ol.osa.org/abstract.cfm?URI=ol-29-16-1900

[75] R. Hunsperger, *Integrated Optics*, 6th ed. Springer, 2009.

[76] E. Pedretti, S. Piacentini, G. Corrielli, R. Osellame, and S. Minardi, "A six-apertures discrete beam combiners for J-band interferometry," Sep 2018. [Online]. Available: https://arxiv.org/abs/1809.01260

[77] A. Saviauk, S. Minardi, F. Dreisow, S. Nolte, and T. Pertsch, "3d-integrated optics component for astronomical spectro-interferometry," *Appl. Opt.*, vol. 52, no. 19, pp. 4556–4565, Jul 2013. [Online]. Available: http://ao.osa.org/abstract.cfm?URI=ao-52-19-4556

[78] E. W. Weisstein, *Cubic Spline*. From *MathWorld*–A Wolfram Web Resource. [Online]. Available: http://mathworld.wolfram.com/CubicSpline.html

[79] W.-J. Chen, S. M. Eaton, H. Zhang, and P. R. Herman, "Broadband directional couplers fabricated in bulk glass with high repetition rate femtosecond laser pulses," *Opt. Express*, vol. 16, no. 15, pp. 11 470–11 480, Jul 2008. [Online]. Available: http://www.opticsexpress.org/abstract.cfm?URI=oe-16-15-11470

[80] O. Svelto, *Principles of Lasers*, 5th ed. Springer, 2010.

[81] *Lasers and laser-related equipment – Test methods for laser beam widths, divergence angles and beam propagation ratios.* ISO 11146, 2005.